GEOCHEMICAL AND MINERALOGICAL CHARACTERISATION OF THE INCA URANIUM MINERALISATION IN THE CENTRAL ZONE OF THE DAMARA BELT, NAMIBIA

A MINI THESIS SUBMITTED IN PARTIAL FULFILMENT

OF THE REQUIREMENTS FOR THE DEGREE OF

MASTER OF SCIENCE IN APPLIED GEOLOGY

OF

THE UNIVERSITY OF NAMIBIA

BY

APHARY MUYONGO

9978402

SEPTEMBER 2020

SUPERVISOR: PROFESSOR A. F. KAMONA (GEOLOGY DEPARTMENT, UNIVERSITY OF NAMIBIA)

Abstract

The Inca uranium deposit is situated about 40 km east of the town Swakopmund in the central Namib Desert within the Erongo region, in western Namibia. It is located within the uranium-endowed Central Zone of the Pan African Damara orogenic belt. The deposit is hosted in amphibolite facies grade metasedimentary rocks of the Lower Swakop Group of the Damara Supergoup. Characterisation of mineralogical and geochemical features of the Inca uranium mineralisation has been conducted to enhance the understanding of formation processes of the deposit. The objectives of the study were to characterise the occurrence of uranium mineralisation and to establish a genetic model of the deposit. This quantitative study has been conducted through whole-rock major and trace element geochemical analytical methods comprising ICP-OES and ICP-MS; and XRD method for mineral identification; as well as scanning electron microscopy and optical petrographic examination of selected drill core samples from three selected boreholes. Major element abundances of most samples are characterised by anomalous silica and iron oxides related to metamorphic and magmatic-hydrothermal alterations. Trace element abundances of some samples such as S, Pb, and Zn depict positive correlation with uranium mineralisation and is postulated to simultaneous and successive distinct processes. REE and uranium enrichment correlation particularly associated with magnetite skarn rocks suggests mobility of REE during hydrothermal uranium mineralisation. Uranium mineralisation is essentially made up of interstitially disseminated euhedral to subeuhedral primary uraninite and secondary, hydrothermal, massive to semi-massive and botryoidal coffinite occurring as fracture infills, veinlets and coatings around grain boundaries of gangue mineral assemblages of host metasedimentary and leucogranite rocks. Uraninite is intimately related to prograde metamorphic assemblages and magnetite skarn rock. Coffinite is derived from partial dissolution of uraninite under hydrothermal conditions and

is associated with sulphide and REE mineralisation as fracture infills and along grain boundaries of host mineral assemblages of the iron skarn and calc-silicate rocks as well as leucogranites. Pervasive fracturing associated with secondary mineralisation suggests that fractures facilitated the remobilization of metals and served both as conduit for fluid transport and as deposition sites. The magnetite skarn rock served as a redox boundary for metal rich circulating hydrothermal fluids and triggered precipitation of uranium mineralisation and associated ore minerals such as galena, and xenotime. Botryoidal coffinite mineralisation together with opal and aragonite appear to be associated with late meteoric fluids under hydrothermal conditions. Partial oxidation of magnetite to hematite is suggested to be related to this later event. Further research work in mineral geochemistry, U-Pb geochronology and stable isotope is recommended to advance the understanding of the evolution and quantification of the ore forming processes involved in the formation of the Inca U deposit.

Acknowledgements

Firstly, I thank the almighty God for giving me strength to persevere and complete my research. If it was not for his blessings, I was not going to be able to learn and understand my study amidst competing needs. Secondly, I would like to thank my supervisor Prof. A. F. Kamona for his unwavering support through advice and guidance during my research. Thirdly, my sincere appreciation to the Department of Geology, University of Nancy, France for their support on SEM analysis. I would like to acknowledge and thank Prof. Judith Kinnaird for her support and discussion on uranium mineralisation in the uranium province of Namibia. Furthermore, I am deeply indebted to the Geological Survey of Namibia and its staff for their support during my research. I would like to thank Reptile Uranium Namibia (Pty) Ltd (now Reptile Mineral Resources and Exploration (Pty) Ltd) for according me an opportunity and support to study the Inca U deposit. Finally yet importantly, I would like to thank my family for their patience and support during my research.

Dedication

This mini-thesis is dedicated to my children Kachana, Aphary Jr, Mooka, Chris and Lapi who have been my source of motivation, and to my wife for her unfaltering support and patience.

Declarations

I, Aphary Muyongo, hereby declare that this study is a true reflection of my own research, and that this work, or part thereof has not been submitted for a degree in any other institution of higher education.

……. [Signature] Date……..

Table of Contents

Abstract i

Acknowledgements iii

Dedication iv

Declarations v

Table of Contents vi

List of Tables viii

List of Figures viii

List of abbreviations and/or acronyms xi

Chapter 1 1

1. Introduction 1

1.1 Background of the study 1

1.2 Statement of the problem 3

1.3 Objectives of the study 3

1.4 Hypothesis of the study 3

1.5 Significance of the study 3

1.6 Limitation of the study 4

1.7 Delimitation of the study 4

Chapter 2 5

2. Literature review and theoretical framework 5

2.1 Evolution of uranium deposits 5

2.2 Diversity of uranium deposits 6

2.3 Uranium behaviour in magmatic-hydrothermal processes 12

2.4 Overview of uranium mineralisation in the Central Zone of the Damara belt 14

2.4.1 Uranium metallogenesis in the Central Zone (CZ) 14

2.4.2 Uranium mineralisation in the Central Zone (CZ) 14

2.5 Geological setting and mineralisation of Inca uranium deposit 14

Chapter 3 19

3. Research methods 19

3.1 Research design 19

3.2 Sample and laboratory Sample Preparation 19

3.3 Geochemistry 20
3.4 Mineral Petrography 22
3.5 Data analysis 23
3.6 Research ethics 23
Chapter 4 24
4. Results 24
4.1 Mineral Petrography of Samples 24
4.1.1 Mineral Petrography of Metasedimentary rocks 29
4.1.2 Mineral Petrography of Granites 38
4.1.3 Mineral Petrography of the Iron skarn rock 39
4.2 Scanning Electron Microscopy of selected U ore 41
4.2.1 Mineral phases of samples 42
4.2.2 Textural characteristics of U ore 52
4.3 Geochemistry 60
4.3.1 Geochemistry of borehole INCRD 155 65
4.3.2 Geochemistry of borehole INCRD 277 73
4.3.3 Geochemistry of borehole INCRD 332 79
Chapter 5 86
5. Discussion 86
5.1 Primary genesis of uranium mineralisation 86
5.2 Secondary hydrothermal uranium mineralisation 87
5.3 Magnetite skarn 88
5.4 Mineral paragenesis 90
5.5 Geochemical processes, anomalies and trends 92
5.6 Mineralisation Model 97
Chapter 6 99
6. Conclusions and Recommendations 99
6.1 Conclusion 99
6.2 Recommendations 100
7. References 101

List of Tables

Table 4.1. Lithology and XRD identified minerals in selected whole-rock samples from boreholes INCRD 277, INCRD 332 and INCRD 155. 24
Table 4.2. Major element oxides content (wt.%) of samples from boreholes INCRD 332, INCRD 155 and INCRD 277. 62
Table 4.3. Lithophile trace element concentrations of samples from borehole INCRD 155. 66
Table 4.4. Siderophile trace element and uranium concentrations of samples from borehole INCRD 155. 68
Table 4.5. Chalcophile trace elements and U concentrations of samples from borehole INCRD 155 70
Table 4.6. Concentration of selected lithophile trace elements of samples from borehole INCRD 277.... 74
Table 4.7. Concentrations of chalcophile trace elements and U of samples from borehole INCRD 227. .. 77
Table 4.8. Concentrations of selected lithophile trace elements of samples from borehole INCRD 332. . 80
Table 4.9. Concentrations of selected chalcophile trace elements and U of samples from borehole INCRD 332. 82
Table 5.1. A summary of observed mineral paragenetic sequence in the studied samples from borehole INCRD 155, INCRD 277 and INCRD 332. 91

List of Figures

Figure 1.1 Distribution of uranium deposits and projects (purple dots) in Namibia. Note the high concentration of the dots in central Namib Desert, the uranium province of Namibia (Geological Survey of Namibia, 2018)..... 2
Figure 2.1. Schematic diagram showing position of uranium deposits relative to main fractionation processes during the rock cycle (Bruneton and Cuney, 2016). 7
Figure 2.2. Geological setting of the Inca uranium deposit in the Central Zone of the Damara Orogenic Belt (After Geological Survey of Namibia - 1:250 000 Walvis Bay 2214 Geological map sheet, 2019). 15
Figure 2.3 Schematic map showing location of Inca deposit in relation to other U deposits and Reptile Uranium (Pty) Limited projects in the Central Zone of the Damara belt (Deep Yellow (Pty) Ltd)..... 17
Figure 2.4. Cross-section along 488700m easting looking towards west indicates sectional lithologies (Marble – blue, Garnetite – brown; Calc-silicate - pale green; Iron skarn – grey; Biotite gneiss - olive green; Breccia - shaded grey; Hybrid granite – orange, Granite – pink) at Inca deposit. The insert map depict the synclinal footwall marble (Reptile Uranium (Pty) Ltd.). 18
Figure 4.1. Granoblastic interbolate texture of calc-silicate rock under cross-polarised transmitted light microscope. Plg –plagioclase, Cc – calcite, Amp – hornblende, Qtz – quartz. 10x magnification, field of view 10mm..... 30
Figure 4.2. Ganoblastic interbolate texture of calc-silicate rock under plane-polarised transmitted light microscopy. Plg –plagioclase, Cc – calcite, Amp – hornblende, Qtz – quartz. 10x magnification, field of view 10mm..... 31

Figure 4.3. Photomicrograph showing magnetite replacement texture in the calc-silicate rock. Fracture (vein) filled by silicate mineral assemblages. UO – rare cob-web uraninite; S-qtz is smoky quartz; Mt-magnetite; Qtz 2 - hydrothermal quartz, Hb-hornblende, Bt- biotite, under transmitted polarised light microscope, 4x magnification, field of view 10mm. 32
Figure 4.4. Reflected photomicrograph depicting magnetite (Mt) and hematite (Hm) replacement texture as well as rare micro cob-web uraninite (UO) grain associated with quartz in bottom left corner under plane-polarised reflected light microscope, 10x magnification, field of view10 mm. 33
Figure 4.5. Replacement textures of quartz (Qtz-2, pale-grey) and magnetite (Mt, black) along cleavage planes in hornblende (Amp) and pyroxene (Px) rich calc-silicate rock, 4x magnification, field of view 10mm 34
Figure 4.6. Replacement texture under transmitted cross polarised light microscope: biotite (Bt) replacing hornblende (Hb), quartz (Qtz-2) replacing hornblende and Mt replacing bitotite, quartz and hornblende in a calc-silicate protolith. 4x magnification, field of view 10mm 35
Figure 4.7. Replacement texture under reflected polarised light microscope: biotite (Bt) replacing hornblende (Hb), quartz (Qtz-2) replacing hornblende and Mt replacing bitotite, quartz and hornblende in a calc-silicate protolith. Magnetite is replaced by hematite along grain boundaries and fractures. 4x magnification, field of view 10mm 36
Figure 4.8. Granoblastic polygonal texture calcite (Cc) is replaced by magnetite (Mt- black). Under cross-polarised transmitted light, 10x magnification, field of view 10mm 37
Figure 4.9. Quartz (Qtz-2) –sericite (Sc) - magnetite (Mt) replacement textures of plagioclase (Plg), quartz (Qtz) and botite (Bt) in a granite. Under cross-polarised transmitted light, 10x magnification, field of view 10mm 39
Figure 4.10. Photomicrograph of an iron skarn rock (black) with remnant calcite (Cc) aggregate of possibly a calc-silicate rock under cross-polarised transmitted light microscope, 10x magnification, field of view 10mm 40
Figure 4.11. Photomicrograph of an iron skarn rock (black) with remnant calcite (Cc) aggregate of possibly a calc-silicate rock under cross-polarised transmitted light microscope, 10x magnification, field of view 10mm. Localised minor partial replacement of magnetite by hematite (Hm). 41
Figure 4.12. Granoblastic fractured magnetite pale grey colour (Mt) and hematite alteration in dark grey (Hm). 42
Figure 4.13. SEM photomicrograph showing somewhat-hexagonal, coarse-grained uraninite (UO) interlocked with magnetite (Mt, pale-grey). Dark grey shade in the top right corner is marker pen print on the slide 43
Figure 4.14. SEM photomicrograph of fractured uraninite (UO) exhibiting enclosing replacement texture hosted in fractured massive magnetite. 44
Figure 4.15. SEM photomicrograph of fractured coffinite (Spectre 1, USi) associated with Yttrium (xenotime) with silicification colloform texture around it. UO is uraninite 45
Figure 4.16. SEM spectral graph of fractured coffinite (Spectre 1, Fig. 23) associated with Yttrium (xenotime) with silicification colloform texture around it. 45
Figure 4.17. SEM photomicrograph of apatite (spectre 2, Ap) with fractures partly filled with hydrothermal uraninite (UO) mineralisation, and partly replaced by uraninite and quartz (Qtz-2). 46
Figure 4.18. SEM photomicrograph of apatite (spectre 2 in Fig. 25). 47

Figure 4.19. SEM photomicrograph showing uraninite (UO), Apatite (Ap), coffinite (USi) and diopside (Spectre 3) resident to hydrothermal mineralisation. 47
Figure 4.20. SEM spectral graph showing diopside (Spectre 3 in Fig. 4. 27). 48
Figure 4.21. SEM photomicrograph of calcite (Spectre 4), apatite (Ap) and uraninite in host calc-silicate rock. 48
Figure 4.22. SEM spectral graph of calcite in host calc-silicate rock (Fig. 29). 49
Figure 4.23. SEM photomicrograph of galena (spectre 5). 50
Figure 4.24. SEM spectral graph of galena (spectre 5, Fig. 4.23). 50
Figure 4.25. SEM photomicrograph of hydrothermal quartz (Spectre 7) replacing apatite. 51
Figure 4.26. SEM spectral graph of hydrothermal quartz (Spectre 7, Fig. 4.25). 51
Figure 4.27. SEM photomicrograph showing massive botryoidal or colloform coffinite (white colour) with undistinguished needle-like mineral within calc-silicate rock. Red arrow depicts an inferred overprinted linear structure. 52
Figure 4.28. SEM photomicrograph of coarse-grained (200 - 400µm in size) uraninite, and micro-fractures as well as grain boundaries filled with hydrothermal mineralisation in iron skarn rock. 53
Figure 4.29. SEM photomicrograph showing partial dissolution and leaching of uraninite (UO) into fractures and as partial aureole around its grain (pale grey and grey). 54
Figure 4.30. SEM Photomicrograph of a hydrothermal vein associated with hydrothermal uranium, REE (pale grey) and sulphide mineralisation. Bright white cubic galena (PbS) on the middle right margin of the plate. 55
Figure 4.31. Metamictization of uraninite (UO) indicated by alpha-decay halo around its grain boundary. Botryoidal quartz and coffinite (USi) in the top middle right and fracture infilling of coffinite in the bottom right of the photomicrograph. 56
Figure 4.32. SEM photomicrograph of in-situ alteration (centre, pale grey and grey) of uraninite (white) and metamictization halo on the left of the photomicrograph. 57
Figure 4.33. SEM photomicrograph depicting two compositional zones (corona texture) around uraninite grain and anhendral to subeuhedral apatite enclosed in uraninite. 58
Figure 4.34. SEM photomicrograph showing pervasively fractured uraninite grain with composition zonation and replacement texture around its grain margins within a silicate groundmass. 59
Figure 4.35. SEM photomicrograph of Sulphide, REE and coffinite (USi) mineralisation at the left top and bottom of a quartz grain (subrounded, pale-grey, Qtz), around grain boundaries, and in fractures. Calcite I – calcite of calc-silicate rock; S-Qtz – silicification quartz. 60
Figure 4.36. Major oxide element abundances of samples from borehole INCRD 155. 65
Figure 4.37. Siderophile trace element distribution of samples from borehole INCRD 155. 68
Figure 4.38. REE patterns of samples from borehole INCRD 155. 72
Figure 4.39. Relationship of major oxides in borehole INCRD 277. 74
Figure 4.40. Distribution of selected siderophile trace elements of samples from borehole INCRD 277. 76
Figure 4.41. REE patterns of samples from borehole INCRD 277. 79
Figure 4.42 Major element oxide distributions of samples from borehole INCRD 332. 80
Figure 4.43. Distribution of selected siderophile trace elements of samples from borehole INCRD 332. 84
Figure 4.44. REE patterns of samples from borehole INCRD 332. 85
Figure 5.1. Correlation coefficient (R^2) of U verses Y (Yttrium) concentration in drill hole INCRD 277. 94

Figure 5.2. Correlation coefficient (R^2) of U and Y concentration in drill hole INCRD 155. 95
Figure 5.3. Correlation coefficient (R^2) of U verses Pb concentration in drillhole INCRD 332..... 95
Figure 5.4. Correlation coefficient (R^2) of U verses Pb concentration in drill hole INCRD 277..... 96
Figure 5.5. Correlation coefficient (R^2) of U verses Pb concentration in drill hole INCRD 155..... 96

List of abbreviations and/or acronyms

Al – Aluminium

Al_2O_3 – Aluminium oxide

Ba – Barium

Ca – Calcium

CaO – Calcium oxide

Ce - Cerium

Co – Cobalt

Conc. - Concentration

Cr – Cromium

CZ – Central Zone

Dy – Dysprosium

Eu - Europium

Er – Erbium

Fe - Iron

Fe_2O_3 – Iron (III) oxide

Gd – Gadolinium

Hm - Hematite

Ho – Holbium

K – Potassium

K_2O – Potassium oxide

La - Lanthanum

Lu – Lutetium

Mg – Magnesium

MgO – Magnesium Oxide

Mn - Manganese

MnO – Manganese (II) oxide

Mt - Magnetite

Na – Sodium

Na_2O – Sodium oxide

Nd – Neodynium

Ni - Nikel

P – Phosphorous

Pb - Lead

P_2O_5 - Phosphate

Pm – Promethium

Pr - Praseodynium

Qtz – Quartz (gangue mineral)

Qtz-2 – Hydrothermal quartz

Rb - Rubidium

REE – Rare earth elements

S - Sulphur

Sm - Samarium

Sc – Scandium

Si – Silica

SiO_2 – Silica dioxide

S-Qtz - Silification

U – Uranium

UO_2 – Uranium Oxide

USi – Uranium Silicate

Ta - Tantalum

Tb – Terbium

Ti –Titanium

TiO_2 – Titanium oxide

Th - Thorium

Y - Yttrium

Yb – Ytterbium

Chapter 1

1. Introduction

1.1 Background of the study

The Inca uranium deposit is located within the Central Zone (CZ) of the Pan African NE- trending Damara Orogenic Belt, about 40 km east of the town of Swakopmund in the Namib Desert of western Namibia. The deposit was discovered in 2007 by Reptile Uranium Namibia (Pty) Ltd and appears to represent a unique type of magnetite bearing uranium mineralisation hosted by metasedimentary rocks of the Lower Swakop Group of the Damara Supergroup.

The central Namib Desert is endowed with abundant uranium deposits and is referred to as the Uranium Province of Namibia (Fig. 1.1). Uranium has been known to occur in Namibia since the 1920s when the first uranium-containing mineral, davidite and several uranium bearing titanium and iron oxides were discovered in areas around Rössing mine (Marlow, 1981). In the 1960s, improved uranium market demand and prices coupled with the availability of airborne radiometric data acquired by the Geological Survey of Namibia led to extensive prospecting and exploration activities and the subsequent discovery of the several uranium deposits e.g., Rössing and Ida Dome. In the Central Zone of the Damara belt, uranium mineralisation is manifested through magmatic uranium deposits hosted in leucogranites (e.g., Rössing deposit) and epigenetic uranium deposits hosted mainly in calcrete (e.g., Langer Heinrich deposit). The Inca uranium deposit appears to represent a significant and different style of uranium mineralisation in the Central Zone.

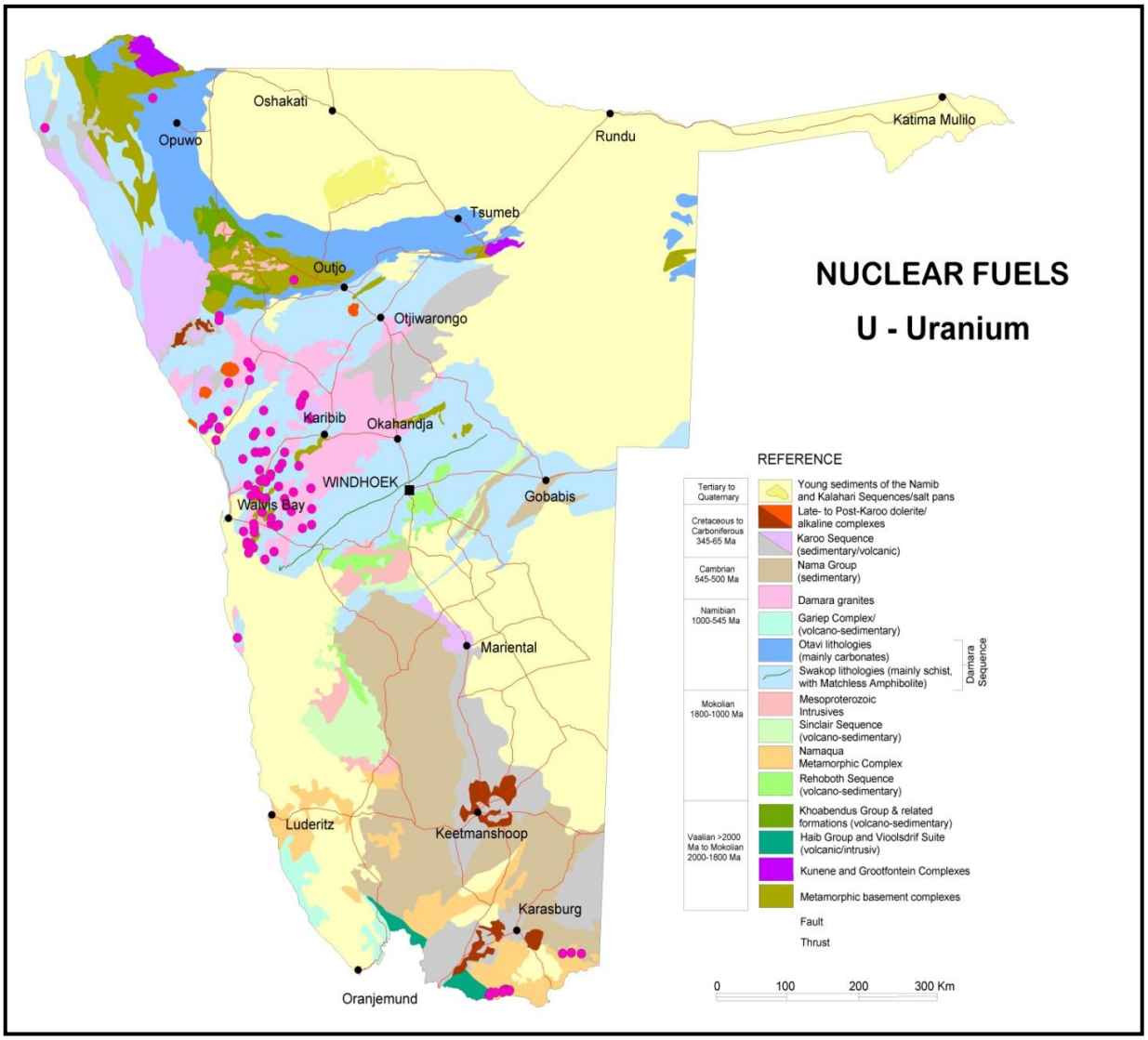

Figure 1.1 Distribution of uranium deposits and projects (purple dots) in Namibia. Note the high concentration of the dots in central Namib Desert, the uranium province of Namibia (Geological Survey of Namibia, 2018).

At present, three uranium mines namely; Rössing, Langer Heinrich, and Husab have been operational and a number of deposits have been qualified as economically exploiTable (e.g., Etango and Omahola projects for Bannermen resources (Pty) Ltd and Reptile Uranium Namibia (Pty) Ltd respectively).

1.2 Statement of the problem

Despite previous studies by Reptile Uranium Namibia (Pty) Ltd, the genetic evolution of the Inca deposit is not yet well established as indicated by the fact that mineralisation has been considered as skarn type, despite the lack of skarn alteration zones and associated mineralogical assemblages, (Pontifex and Associates, 2008; Reyx, 2009). If indeed, the Inca is of skarn-type deposit then there is a need for supporting mineralogical and geochemical evidence, which can confirm it as a skarn type, deposit. This study examines and provides a comprehensive synthesis of the diverse mineralogy and geochemical features that have vital implications for the understanding of uranium mineralisation and genesis of the Inca deposit.

1.3 Objectives of the study

The principal objectives of the study are to:

a) Characterise the occurrence and distribution of the uranium mineralisation at the Inca deposit; and

b) Establish a genetic model of the deposit.

1.4 Hypothesis of the study

Formation of the Inca deposit involved metasomatic processes resulting from interaction of uranium bearing hydrothermal fluids with the host metasedimentary rocks to precipitate uranium due to changes in either pH, redox conditions and temperature.

1.5 Significance of the study

The study will contribute to the understanding of the genesis of the Inca uranium deposit, which will assist in the search and discovery of similar deposits in Namibia.

1.6 Limitation of the study

The scope of the work undertaken was constrained by limited funds and the lack of appropriate analytical equipment for geochemical analyses.

1.7 Delimitation of the study

Due to limited funds, EMP analyses on minerals were not conducted and the geochemical techniques only involved SEM, ICP-OES, and XRD analyses.

Chapter 2

2. Literature review and theoretical framework

2.1 Evolution of uranium deposits

Although no uranium deposits are likely to occur before 3.1 Ga, they have formed from Neoarchaean to Quareternary (Bruneton and Cuney, 2016). Based on the origins and near surface distributions of known uranium and thorium minerals on earth, Hazen et al., (2009) divided their evolution into four periods.

The first period, from Hadean to early Archean (ca. 4.5 to 3.5 Ga), is represented by successive concentrations of uranium and thorium from their original trace uniform distribution chondritic abundance (< 10 and < 30 ppm respectively) into magmatic related fluids from which the first U^{4+} and Th^{4+} minerals, uraninite (UO_2), thoriate (ThO_2), and coffinite ($USiO_4$) formed in the Earth's crust.

The second period from ~3.5 to 2.2 Ga, involved the formation of low-grade concentrations of detrital uraninite with high weight percent thorium such as in the Witwatersrand-type quartz pebble conglomerates, which were deposited in highly anoxic fluviatile environment.

The third period began at ~2.2 Ga, and coincided with the Great Oxidation Event (GOE) in which most known uranium minerals first precipitated from reactions of soluble uranyl $(U^{6+}O_2)^{2+}$ complexes. Because of the GOE, these reactions must have been aided by biological activities. The majority of uraninite deposited during this period was low in Th, and precipitated from saline and oxidizing hydrothermal solutions transporting $(UO_2)^{2+}$-chloride complexes. The unconformity- and vein-type uranium deposit in Australia and Canada respectively, and Oklo natural nuclear reactors in Gabon are examples of deposits formed in third period. The onset of

hydrothermal transport of $(UO_2)^{2+}$ complexes in the upper crust may indicate the availability of calcium sulphate-bearing evaporites after the GOE.

The fourth period began ~400 million years ago and coincide with the rise of land plants which led to terrestrial and shallow marine organic rich sediments that promoted new sandstone-type uranium deposits. These sediment-hosted uranium deposits formed at redox fronts, where organic matter reduced low-temperature, near surface, uranyl-rich waters and led to precipitation of uraninite and coffinite.

Hazen et al. (2009) further postulated that the modes of uranium accumulation and composition of uraninite including the multiple oxidation states of Uranium (4^+, 5^+, 6^+) are a sensitive indicator of global redox conditions. In contrast, thorium does not reflect changing redox conditions because it has a single oxidation state (4^+) that has a very low solubility in the absence of fluorine complexes. Thus, geochemical accumulation of thorium relative to uranium at high temperature is limited to special magmatic environments, where U^{4+} is preferentially removed by chloride or carbonate complexes and at low temperatures by mineral surface reactions.

The near surface mineralogy of uranium and thorium provide a measure of the earth's geotectonic and geobiological history (Hazen et al., 2009). Without extensive magmatic-related fluids reworking the crust and upper mantle, uranium and thorium would not become concentrated sufficiently to form their own deposits. In addition, without surface oxidation majority of known uranium minerals are unlikely to have formed (Hazen et al., 2009).

2.2 Diversity of uranium deposits

The formation processes of uranium deposits spans nearly all stages of the geological cycle, ranging from from high grade metamorphic conditions to plutonic, metasomatic, hydrothermal,

basinal diagenetic, metamorphic, and volcanic to sedimentary and superficial environments with the calcretes (Bruneton and Cuney, 2016). Cuney (2009) described the diversity of uranium deposits and suggested a genetic classification of uranium deposits based on the classification of the geochemical behaviour of uranium in fluids, silicate melts, and on the fractionation mechanisms of uranium in uranium-rich peraluminous, metaluminous, and peralkaline melts. These mineral deposit classes are briefly discussed below according to conditions of formation during the rock cycle, Fig 2.1, (Bruneton and Cuney, 2016).

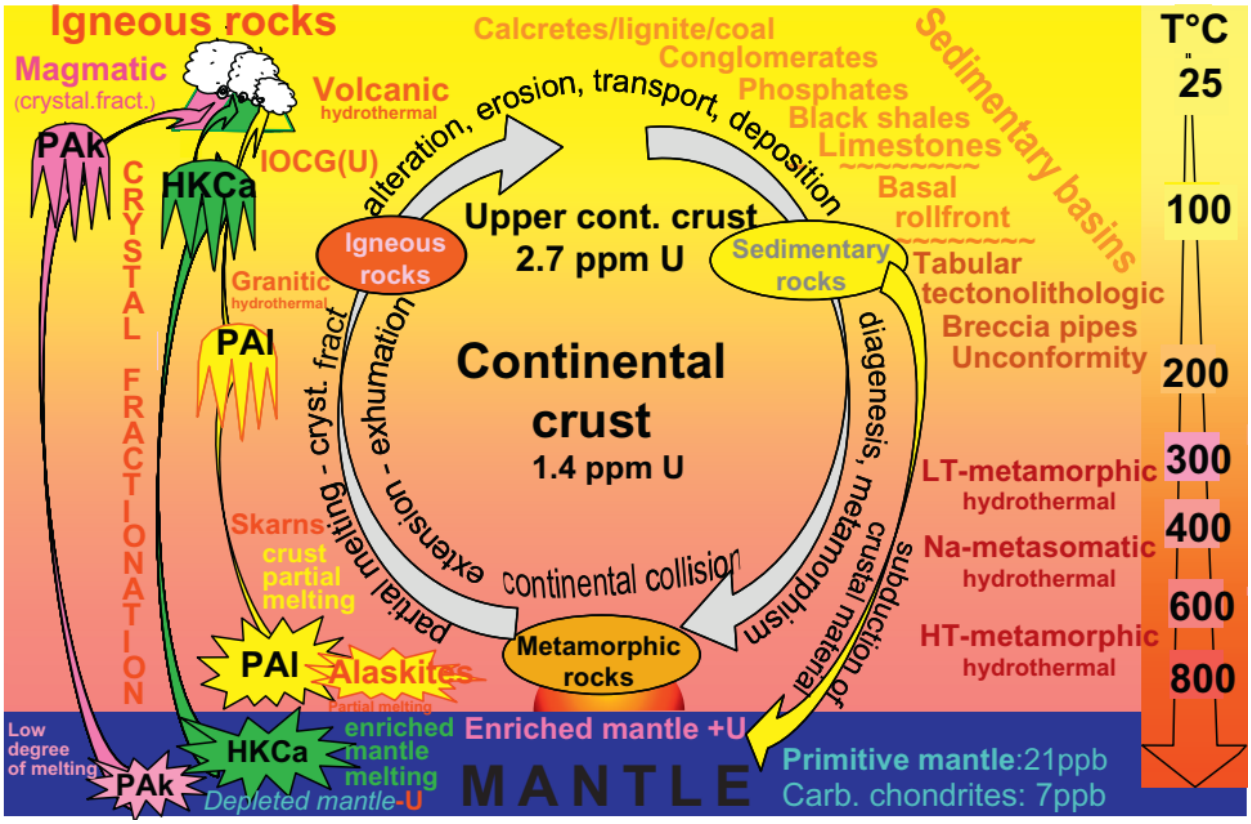

Figure 2.1. Schematic diagram showing position of uranium deposits relative to main fractionation processes during the rock cycle (Bruneton and Cuney, 2016).

The first class, uranium deposits related to surface processes, correspond to syn- to early-epigenetic near surface uranium concentrations formed during intracontinental sedimentation and weathering (Cuney, 2009). Placer deposits were the first uranium deposits to form on earth and are exemplified by the Witwatersrand uranium deposit within the Dominion Group (2.1 Ga) in South Africa. Another example at the opposite geological time scale are the Tertiary to Present uranium deposits of Langer Heinrich deposit in Namibia, and is associated with calcrete which formed in arid to semi climatic conditions by evapotranspiration of a fluviatile to playa system (Cuney, 2009).

Syn-sedimentary uranium deposits are the second class, formed during sedimentation in epicontinental platform environments, exemplified by the uranium-rich black shales and phosphorites (Cuney, 2009). The formation of phosphorites is restricted to shallow continental shelves where limited current circulations are prevalent. The substitution of Ca^{2+} by U^{4+} in the apatite structure and subsequent biologically induced reducing environments can lead to uranium deposition outside of the apatite structure (Cuney, 2009). The largest of this type of deposits occurred during Cretaceous to Eocene at latitudes 8^{o} - 15^{o} N and forms a belt along the southern margins of the Tethys Ocean (Cuney, 2009). This uranium-phosphorite belt extends from Turkey to Morocco and the latter is host to three quarters of world resources of Syn-sedimentary uranium deposits (Cuney, 2009).

The third class are the uranium deposits related to hydrothermal processes, and constitute a wide variety of ore deposit type in uranium geology literature (Cuney, 2009). The deposits are typically of epigenetic nature and formed during fluid circulation through porous and occasionally fractured fluviatile, lacustrine, deltaic to near shore siliciclastic sediments, sometimes in limestones, or through fractured granitic, volcanic, or metamorphic rocks (Cuney, 2009). The uranium transport

is by various fluids of meteoric, diagenetic, and/or metamorphic nature. The subtypes of this hydrothermal uranium deposits include:

Basal type uranium deposits which are at the border between surficial and diagenetic-hydrothermal types (Cuney, 2009). These deposits occur in poorly sorted and consolidated, permeable, fluvial to lacustrine carbonaceous gravels and sands accumulated as thin elongated bodies (10-15km) along palaeovalleys incised in basement rocks and covered by plateau basalts. An example is the Blizzard deposit in Canada (Cuney, 2009).

Tabular uranium deposits which are at the border between syn-sedimentary and diagenetic-hydrothermal deposits (Cuney, 2009). Uranium deposition may begin shortly after sedimentation and burial, but often during diagenesis. Ore bodies form within sandy layers intercalated with non-permeable clay zones commonly marginal to palaeochannels. The major source of uranium is the volcanic ash within the sandstone. The mode of uranium transport is through brines, which are released from underlying evaporitic sediments. Examples are those in the Grants region, Colorado (Cuney, 2009).

Roll-front uranium deposits symbolise the epigenetic deposition of uranium at a redox boundary. Host rocks are generally younger than Ordovician and accumulated in fluvial and lacustrine environments or in settings such as marine marginal plains, lagoons, channels, and beach bars (Cuney, 2009). Uranium sources may be host volcanic rocks, volcanic ash as well as external uranium rich granites. The transport of uranium was by oxidized low temperature meteoric waters that infiltrated permeable rocks after some diagenesis had occurred. The ore bodies are crescent shaped in cross section and sinuous along the roll-front interface e.g. Inkai deposit in Kazakhastan (Cuney, 2009).

Tectonic-lithologic deposits which are hosted by sandstones but fluid infiltration is strongly controlled by faults (Cuney, 2009). The deposition processes are similar to those described in tabular uranium deposits. An example is the deposit from the Arlit area in Niger (Cuney, 2009).

Solution-collapse breccia pipes which are near vertical, cylindrical columns, ca. 30-175m in size, and situated in flat-lying upper Paleozoic to Triassic marine platform sediments. Uranium deposition is associated with low temperature,saline, and oxidizing fluids of diagenetic origin that are derived from deeper basinal regions, e.g. those in the Grand Canyon, USA (Cuney, 2009).

Unconformity related deposits which are typical diagenetic-hydrothermal uranium deposits and correspond to focused uranium deposition at the interface between a thick, Paleo- to Meso-Proterozoic sandstone cover and an Archean to Paleoproterozoic crystalline basement, where graphite-rich faults were reactivated (Cuney, 2009). The source of uranium is a subject of debate with those that propose uranium sourced from the basin (Fayek et al., 2002) and those that support the uranium-rich metamorphic basement as the main source (Hecht and Cuney, 2000).

Syn-metamorphic uranium deposits which originate from circulation of metamorphic hydrothermal fluids in association with deformation of rocks. The favourable metamorphic conditions are the low-grade metamorphism of epicontinental platform sediments in which most fluid extraction occurs. The released oxidized brines from both evaporitic horizons and hydrocarbons (from black shales) are efficient for uranium transport and precipitation respectively (Cuney, 2009). An example is the Kansanshi deposit in Zambia that formed

at 350^{o}C +/- 50^{o}C (Kríbek et al., 2005). Syn-metamorphic uranium deposits are not well constrained at high metamorphic conditions (Cuney, 2009).

Metasomatic uranium deposits which are commonly associated with sodium metasomatism (Cuney, 2009). A variety of processes can lead to metasomatic alteration and range from the interaction of magmatic solutions released from peralkaline granite to lower temperature solutions from basinal brine or magma. The Mary Kathleen uranium-mineralised skarns in Australia is an example of metasomatic uranium deposits.

Vein-type uranium deposits which are related to leucogranites and are hosted either in the granites or in metamorphic rocks (Cuney, 2009). They originate from low salinity and low temperature hydrothermal fluids (Dubessy et al., 1987). Uraninite is leached from the granites by oxidized meteoric water and precipitation occurs when these fluids mix with reducing fluids derived from the overlying basin (Turpin et al., 1990).

Uranium deposits which are related to extrusive rocks occur within the wide calderas filled with alternating mafic and felsic volcanic rocks and sedimentary rocks (Cuney, 2009). Peralkaline magma are the source of uranium but the genesis of significant deposits requires million years of magmatism of shallow magma chambers to provide the heat flux which is necessary to generate long lasting fluid convections (Cuney, 2009). Streltsovkoye caldera in Transbaikalia, Russia is an example of this deposit type (Cuney, 2009).

The fourth class of uranium deposits is that related to partial melting. This class is essentially granitoid hosted low-grade uraninite mineralisation emplaced in epicontinental sediments such as arkose, quartzite marlstone and limestone, which have been metamorphosed to upper amphibolite facies accompanied by partial melting (Cuney, 2009). The deposits in this class originate from

extreme fractionation of a deep-seated granite body or from partial melting of uranium-rich metasedimentary or metavolcanic rocks (Cuney, 2009). Apart from uraninite crystalizing from the magma, some uranium concentrations originate from circulation of magmatic fluids and supergene processes (Cuney, 2009). An example of this deposit class is the Rössing Uranium deposit in Erongo region, Namibia (Cuney, 2009).

Uranium deposits related to crystal fractionation are the fifth class, and are only known to occur in peralkaline complexes. As a result of high solubility of U, Zr, Th, and REE in peralkaline melts, continuous enrichment is effectively achieved during fractionation and the final precipitation of complex minerals that incorporate uranium occurs together with these minerals (Cuney, 2009). Therefore, because of high costs related to extracting uranium from refractory minerals, this type of uranium has rarely been mined (Cuney, 2009). The example of this class is the low-grade uranium resource of Kvanefjeld deposit at Ilimaussaq, Greenland (Cuney, 2009).

2.3 Uranium behaviour in magmatic-hydrothermal processes

The concept of magmatic-hydrothermal processes relates to the ore forming processes whereby the role of fluids derived from the magma body, in particular granitic magmas, are central to the formation of mineral deposits (Robb, 2005). Therefore magmatic-hydrothermal processes involve the interaction of fluids derived from a magma body with other fluids and environments such as the meteoric water and near surface settings (Robb, 2005). Majority of mineral ore deposits around the world are formed either as a result of direct processes of circulating hydrothermal fluids through the earth's crust or indirectly through modification by such hot aqueous solutions (Robb, 2005).

Giant uranium deposits of the world are thought to have formed from large scale circulation of brines at temeratures of about 120 to 200 ^{o}C that have interacted with sedimentary rocks and crystalline basement rocks (Richard et al, 2012). It has been suggested by Richard et al., (2012) that the richest uranium deposits of the world have formed from acidic brines (e.g., pH 2.5 to 4.5) which contained uranium and that their period of formation must be short, in the order of 0.1 to 1 Myr.

Some hydrothermal uranium deposits are spatially related to leucogranites which served as the main source of uranium (Ballouard et al., 2017). The incompatible behavior of uranium in silicate magmas results in its concentration in felsic melts and subsequently as uranium sources in granites and rhyolites (Cuney, 2014). Despite the incompatible behavior of uranium, only a few uranium deposits have formed as a direct result of magmatic processes (Cuney, 2014). Amongst a variety type of granites only a few are uranium fertile because uranium endowment does not only depend on uranium content but also on the ability of the uranium-containing phases they host to be leached by fluids (Cuney, 2014). Four varieties of granites or rhyolites namely, peralkaline, high-K metaluminous calc-alkaline, L-type peraluminous and anatectic granitoids can be sufficiently enriched in uranium and may serve as a substantial source for the genesis of uranium deposits (Cuney, 2014). In the L-type peraluminous plutonic rocks uranium mineralisation mainly occurs as uraninite and signify the greatest source of uranium (Cuney, 2014).

Ballouard et al., (2017) postulate that leaching of uranium from granitic sources may be facilitated by low salininty oxidising fluids derived from the surface and could be promoted by tectonic structures. The leaching is usually of sub-solidus alteration of magmatic uranium oxides hosted in granitic sources and is likely to have been precipitated in the reducing settings associated with host metasedimentary rocks (Ballouard et al., 2017). The unfavorability of other types of igneous rocks

to serve as sources for uranium is due to the refractory character of the uranium-bearing phases which does not permit their extraction under the present economic conditions (Cuney, 2014).

2.4 Overview of uranium mineralisation in the Central Zone of the Damara belt

2.4.1 Uranium metallogenesis in the Central Zone (CZ)

Based on the composition of the uraniferous granite sheets, and their proximity and occurrence at the boundary between the Khan and Rössing Formations, Smith (1965) suggested that uranium-rich granites originate from amphibolite grade metamorphism of uraniferous Damaran sediments. Jacob et al., (1986) postulated that the pre-Damaran basement rocks could constitute the source for leucogranites and related uranium mineralisation with very little hydrothermal influence. However, subsequent fluid inclusion studies at Rössing mine have indicated significant post-magmatic overprint enrichment (Kinnaird and Nex, 2007).

2.4.2 Uranium mineralisation in the Central Zone (CZ)

Based on field relationships, petrology and geochemistry, six types of primary uranium bearing leucogranites ranging in composition from tonalitic to alkali-feldspar granites have been distinguished in the southern CZ (Kinnaird and Nex, 2007). Secondary uranium mineralisation related to climatic, geomorphological controls and weathering of primary uranium deposits occur in the form of carnotite in palaeo-river channels and fluviatile sheet wash along palaeo-river channel banks as observed at the Langer Heinrich, Trekkopje and Tubas deposits (Spivey et al., 2010).

2.5 Geological setting and mineralisation of Inca uranium deposit

The Inca uranium deposit occurs within the Central Zone (CZ) of the Damara Orogenic Belt (Fig. 2.2). The dominant structural grain of Inca deposit area is moderate to steeply dipping towards northwest with adjacent dome structures such as the low-grade uranium enriched Ida dome and

Holand's dome in the far north-eastern direction, Fig. 2.2. Inca deposit is located between aeromagnetic interpreted Welwitchia (east) and Omaruru Lineaments (west), Fig. 2.2.

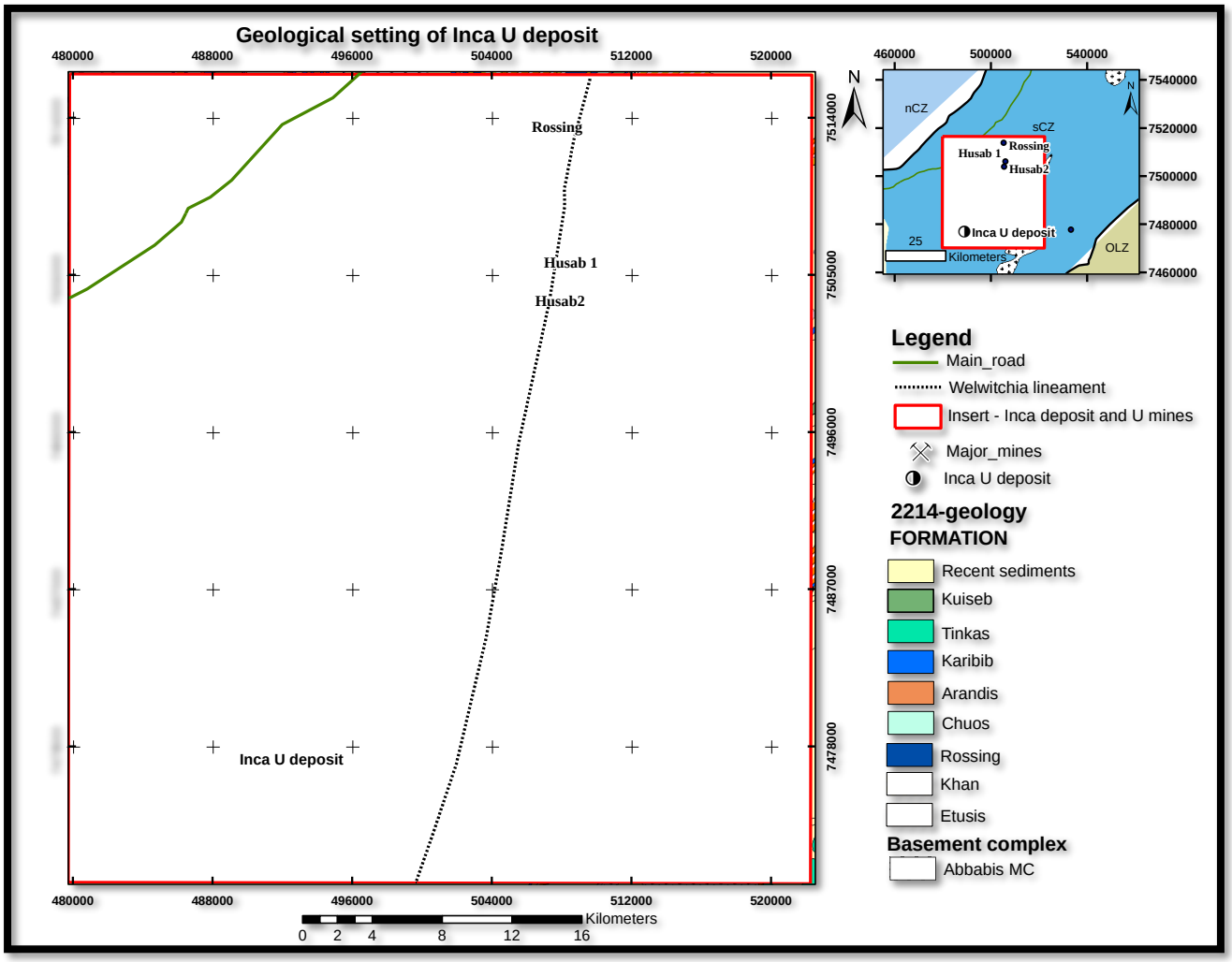

Figure 2.2. Geological setting of the Inca uranium deposit in the Central Zone of the Damara Orogenic Belt (After Geological Survey of Namibia - 1:250 000 Walvis Bay 2214 Geological map sheet, 2019).

The Inca deposit is located south of major known uranium deposits such Rössing and Husab, Fig. 2.2 and Fig. 2.3. The deposit occurs within a hinge zone of a local synclinal structure defined by a

footwall marble interpreted to belong to the Rössing Formation, Fig. 2.4. The partially outcropping synclinal structure has a half wavelength of about 500 m and appears to have been intruded by a generation of undifferentiated granitoids. The unexposed hinge zone and the continuity of the fold structure was confirmed from drilling, and traced from aeromagnetic data obtained by Reptile Uranium Namibia (Pty) Ltd. Brittle deformation is manifested by several moderately dipping (30^{o} to 45^{o}) fault zones and fractures observed from diamond drill core. The fault zones are locally kaolinized and in some places have turned into claystone.

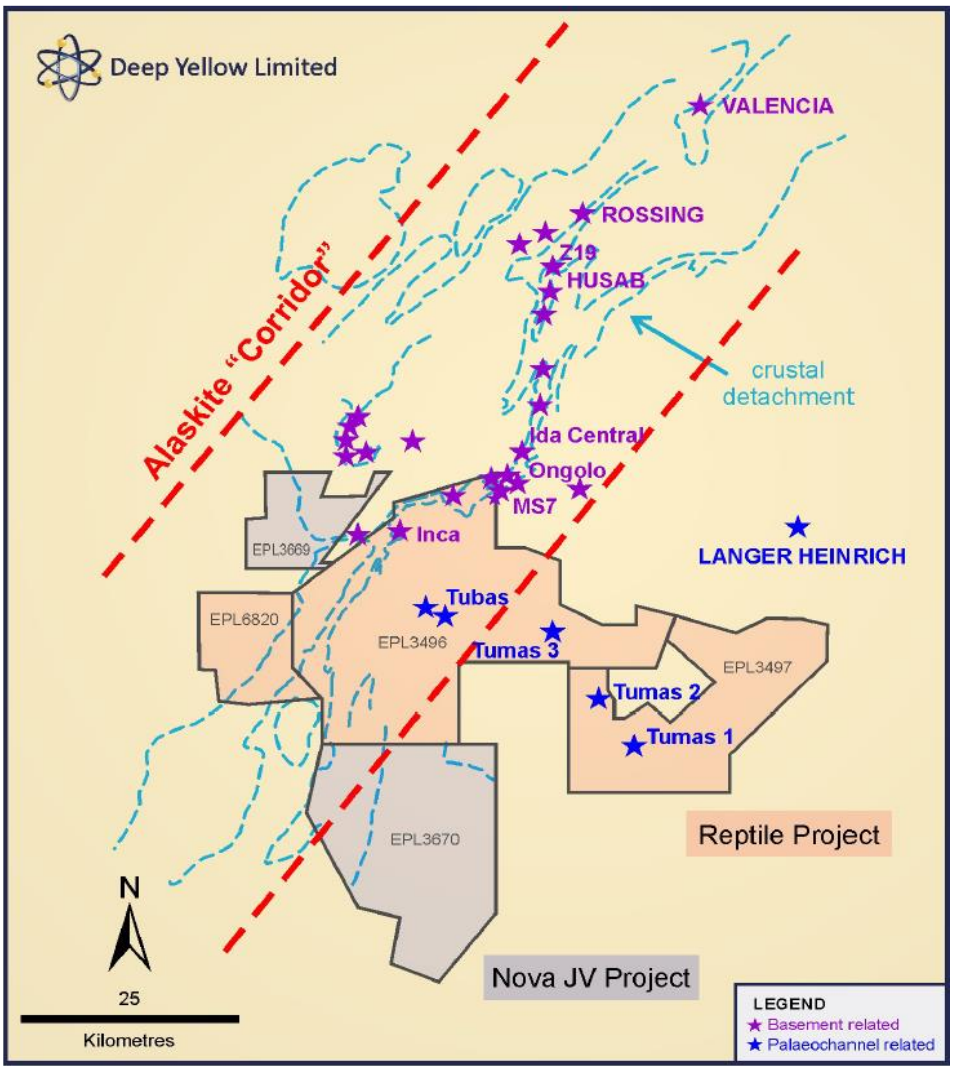

Figure 2.3 Schematic map showing location of Inca deposit in relation to other U deposits and Reptile Uranium (Pty) Limited projects in the Central Zone of the Damara belt (Deep Yellow (Pty) Ltd).

The company reports from Reptile Uranium Namibia (Pty) Ltd. (RUN), e.g., Pontifex and Associates (2008), have suggested that Inca deposit represents a skarn type mineralisation. Uranium mineralisation occurs as uraninite and minor coffinite in calc-silicate and pelitic gneisses of the Lower Swakop Group and to a lesser extent in leucocratic granites. The lithologies at Inca deposit comprise, the footwall marble, garnetite skarn or garnet skarn, magnetite (massive or semi-massive), calc-silicate gneiss (semi-massive or massive), and biotite gneiss which are intruded by late undifferentiated granites, Fig. 2.4. The footwall marble has been mapped by Sawyer (1981) as Karibib Formation on the 1995 Geological Survey of Namibia – 1:250 000 Walvis Bay 2214-map sheet. However, RUN geologists postulated that the marble belongs to Rössing Formation instead.

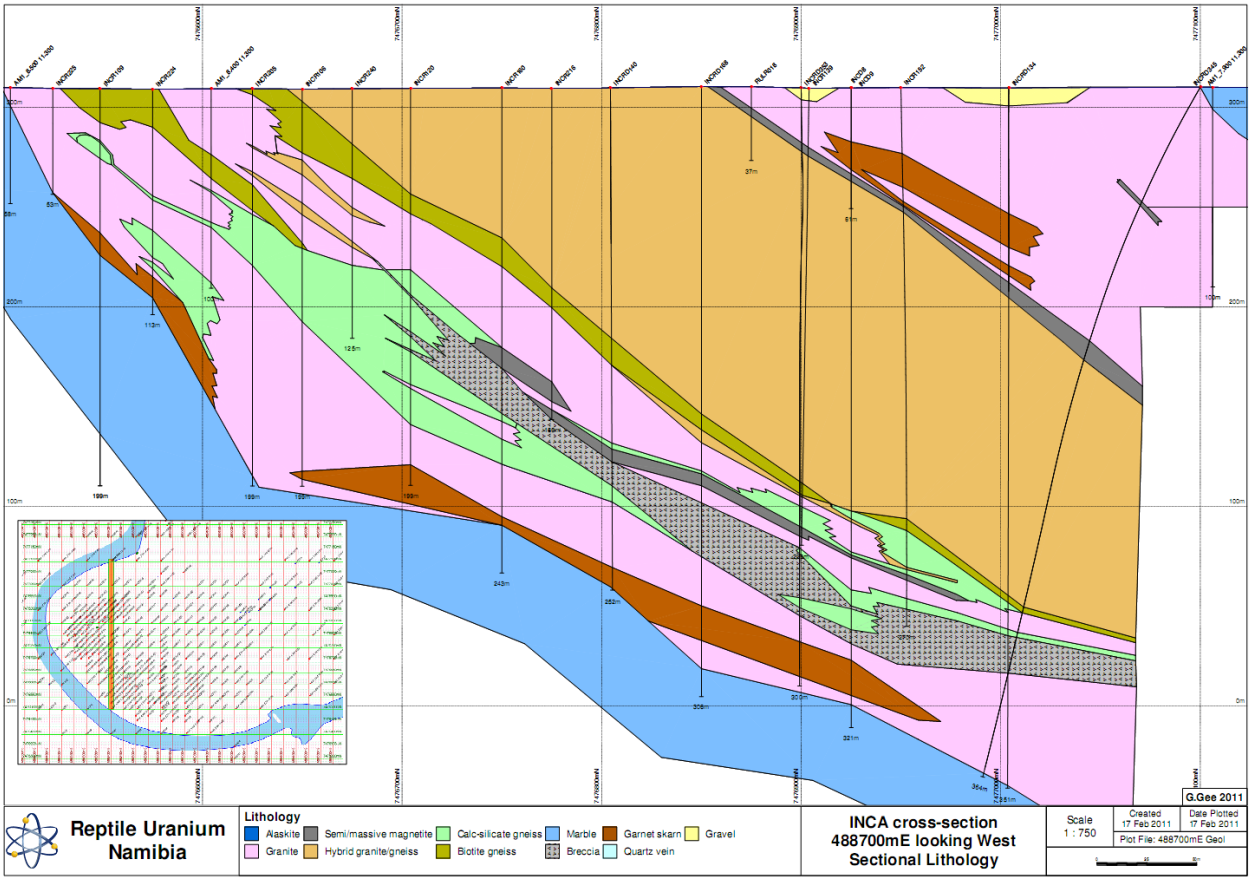

Figure 2.4. Cross-section along 488700m easting looking towards west indicates sectional lithologies (Marble – blue, Garnetite – brown; Calc-silicate - pale green; Iron skarn – grey; Biotite gneiss - olive green; Breccia - shaded grey; Hybrid granite – orange, Granite – pink) at Inca deposit. The insert map depict the synclinal footwall marble (Reptile Uranium (Pty) Ltd.).

The metamorphism of the Inca deposit area is defined by the presence of amphibolite facies assemblages. The calc-silicate and biotite gneisses with alternating metamorphic green amphibole and leucocratic quartz-feldspar bands have been attributed to amphibolite grade metamorphic conditions. The garnetite skarn or garnet skarn along the top contact of the footwall marble that have been intruded by later granites represent remnants of a contact metamorphic event pre-dating the late granitic intrusions that shows no evidence of contact metamorphism.

Chapter 3

3. Research methods

3.1 Research design

This is a quantitative research study based on mineralogical and geochemical data and designed to establish the genetic model of the Inca uranium deposit. Investigations on baseline data were conducted to evaluate exploration data housed at Reptile Uranium Namibia (Pty) Ltd in the town of Swakopmund, Namibia. The purpose of investigations was to select borehole samples that best represent the uranium mineralisation at the Inca deposit. The data assessment study served as a means to collate and create a baseline dataset to form a basis of the study. The investigated data included drill sections, in-house reports, and diamond drill core. The baseline data investigations have been conducted in liaison with Reptile Uranium (Pty) Ltd geologists and included physical examination of exploration data. Based on lithology type and uranium mineralisation, three boreholes INCRD 155, INCRD 277 and INCRD 332 were established as the best representative boreholes upon which the geochemical and mineralogical characterisation of Inca deposit has been conducted. These three boreholes were petrographically studied and sampled for optical and laboratory analyses.

3.2 Sample and laboratory Sample Preparation

With reference to uranium mineralisation and host lithology type, thirty-eight diamond drilled core samples from three boreholes INCRD 155, INCRD 277, and INCRD 332 were collected systematically at approximately 1 m interval. The total number of samples collected from each borehole was directly influenced by the thickness of intersected mineralisation. The quarter-sized core samples range in length between 20 – 30 cm and vary in lithology within and among the boreholes. Ten samples from the chiefly metasedimentary borehole INCRD 332, eleven from the

primarily granite borehole INCRD 277 and seventeen from the predominantly iron skarn borehole INCRD 155 were collected for this study. Samples were collected from lithologies containing anomalous uranium, magnetite and sulphide/sulphate mineralisation within the ore zones, as well as those from footwall and hanging wall have been studied.

Laboratory sample preparations began with sorting and drying of samples, followed by primary preparation that involved crushing each whole sample and then pulverising the crushed sample in a vibrating disc pulveriser under international standard conditions (ISO 17025).

3.3 Geochemistry

Standard analytical procedures practised by geochemical laboratories have been followed, including protocols of systematic sampling, sample contamination, and statistical verification of data to ensure data integrity. The whole-rock geochemical analyses of major and trace element were conducted at the laboratory of Bureau Veritas (Pty) Ltd in Swakopmund, Namibia according to international standards of commercial laboratories. The analyses on thirty-eight samples have been conducted using Inductively Coupled Plasma Mass Spectroscopy (ICP-MS), and Inductively Coupled Optical Emission Spectroscopy (ICP-OES) techniques as described below.

The samples have been digested with a mixture of acids including hydrofluoric, nitric, hydrochloric and perchloric Acids. This digestion approaches a total digest for many elements. However, some refractory oxides such as cassiterite are not efficiently attacked under this digestion method. If Barium occurs as the sulphate mineral, then at high levels of more than 4000

ppm it may re-precipitate after the digest giving seriously low results. Using this digestion, some sulphur losses may occur if the samples contain high levels of sulphide.

The concentration of elements Cu, Co, As, Ag, Cr, Ba, Be, Bi, Cd, Ga, Li, Mo, Pb, Sb, Sn, Sr, W, Hf, Zr, La, Nd, Se, In, Te, Cs, Re, and Tl have been determined by Inductively Coupled Plasma (ICP) Mass Spectrometry. Inductively Coupled Plasma Optical Emission Spectrometry (ICP-OES) has determined the element concentrations of Zn, Ni, Mn, P, Sc, V, Ca, Na, S, SiO_2, Al_2O_3, CaO, and TiO_2. The samples have been fused with Sodium Peroxide and subsequently the melt has been dissolved in dilute hydrochloric acid for analysis. Due to high furnace temperatures, volatile elements are lost. This procedure is particularly efficient for determination of major element composition in the samples or for the determination of refractory mineral species.

The concentration of elements and element oxides B, Si, Fe, Al, Mg, Ti, K, Fe_2O_3, and MgO have been determined by Inductively Coupled Plasma Optical Emission Spectrometry (ICP-OES). The concentrations of elements Ge, Ta, Y, Nb, Ce, Pr, Sm, Eu, Gd, Tb, Dy, Ho, Er, Tm, Yb, Lu, Th, U, Rb have been determined by inductively coupled plasma mass spectrometry (ICP-MS). The samples have been analysed by firing a ~ 40 gm portion of the sample. This is the classical fire assay process and will give total separation of gold, platinum and palladium in the sample. The Inductively Coupled Plasma Optical Emission Spectrometry has determined the concentrations of elements Au, Pt, Pd.

Whole rock major and trace element geochemistry was conducted on all 38 samples, using Inductively coupled plasma optical emission spectrometry (ICP-OES), and inductively coupled

plasma mass spectrometry (ICP-MS) analytical methods. Due to good efficiency and precision, ICP-OES analytical method was used to determine major element geochemistry. The ICP-MS is the accepted technique used in the determination of high precision trace element and isotopic geochemistry of rock samples (Rollinson, 1993). The geochemical data was evaluated, presented and interpreted in order to deduce geochemical characteristics and variation of the deposit.

3.4 Mineral Petrography

The polished and standard thin sections were prepared, under standard laboratory procedures, for optical examinations of mineralogical and textural variation in samples. Optical reflected and transmitted light microscopic studies involved characterisation of gangue and ore minerals.

Scanning Electron Microscope (SEM) studies conducted at the University of Nancy in France enabled identification and characterisation of uranium mineral phases. SEM studies were conducted on selected samples to enable mineral identification and characterisation based on density variation as well as quantitative elemental analysis. These studies were important in determining mineral speciation and textural relationships of the ore minerals abundance and distribution.

Procedures for SEM samples were conducted at the University of Nancy in France. The preparations involved cutting of standard polished thin section sample blocks and impregnation of the blocks with standard laboratory resins before polishing and carbon coating on glass mounted polished thin section. The same procedure has been followed for the preparation of standard thin section, except the carbon coating step. Whole rock X-ray diffraction (XRD) studies conducted on

most samples supplemented the study on mineral identification and verification. The XRD studies were undertaken at the Geological Survey of Namibia in Windhoek, Namibia.

3.5 Data analysis

Microsoft Excel software plots and statistical analyses such as correlation coefficient (R^2) have been applied in the analysis of the geochemical data.

3.6 Research ethics

Permission to sample and conduct research on the deposit was obtained from mineral rights holder of Inca deposit, Reptile Uranium Namibia (Pty) Ltd.

Chapter 4

4. Results

4.1 Mineral Petrography of Samples

This section presents the petrography of ore and gangue minerals from drill core samples collected from ore zones, hanging-wall and footwall zones of three drillholes INCRD 155, INCRD 332 and INCRD 277. The studied samples comprise metasedimentary rocks of calc-silicate gneiss and biotite gneiss, and variable intrusive granitic rocks as well as magnetite rich rock variety referred as iron skarn rock. The samples comprise heterogeneity in rock types related to hydrothermal alteration. The lithologies of the samples are presented in Table 4.1. Deatiled description of rock petrography is presented in the proceeding subsections 4.2.1 to 4.2.3. The mineral assemblages associated with these rock types are characterised in terms of spatial textural features and paragenesis as examined using optical technics of conventional polished thin section microscopy and scanning electron microscopy. The dominant mineral phases in the selected whole rock samples were identified using the x-ray diffraction technique and are presented in Table 4.1.

Table 4.1. Lithology and XRD identified minerals in selected whole-rock samples from boreholes INCRD 277, INCRD 332 and INCRD 155.

Sample No	Major minerals	Major lithology
INCRD 277-1	Quartz, Albite, Microcline	Granite
INCRD 277-2	Quartz, Albite, Microcline, Biotite	Granite
INCRD 277-3	Quartz, Albite, Microcline	Granite

INCRD 277-4	Quartz, Albite-calcian - $(Na,Ca)Al(Si,Al)_3O_8$, Microcline, Anhydrite ($CaSO_4$)	Granite
INCRD 277-5	Graphite, Albite-calcian, Quartz, Phlogopite, Diopside	Biotite schist/gneiss
INCRD 277-6	Quartz, Albite, Microcline	Leucocratic granite
INCRD 277-7	Quartz, Albite-calcian, Anhydrite, Biotite	U mineralised leucocratic granite
INCRD 277-8	Quartz, Albite-calcian, Phlogopite	Biotite schist/gneiss, leucosomes (leucogranite) present, migmatitic
INCRD 277-9	Magnetite, Albite-calcian, Quartz, Riebeckite, Muscovite	Magnetite skarn, feldspar porphyloblast (leucogranite) -pinkish, k-feldspar alteration)
INCRD 277-10	Phlogopite - $KMg_3(Si_3Al)O_{10}(OH)_2$ Calcite – $CaCO_3$	Hydrothermal biotite + calcite alteration, pinkish granite
INCRD 277-11	Quartz, Albite, Microcline	Leucocratic granite
INCRD 332-1	Quartz, Albite-calcian, Microcline	Leucocratic granite
INCRD 332-2	Quartz, Albite, Andesine, Hornblende	Leucocratic granite, scapolite, cavities
INCRD 332-3	Albite-calcian, Quartz, Hornblende, Phlogopite, Anhydrite	Calc-silicate, migmatitic biotite gneiss

INCRD 332-4	Quartz, Albite = Microcline	Leucocraticgranite, weathered, oxidised
INCRD 332-5	Quartz, Albite-calcian, Hastingsite (magmatic amphibole), chlorian potassian - $(K,Na)Ca_2(Fe,Mg)_5(Si,Al)_8O_{22}Cl_2$)	Leucocratic granite, Biotite gneiss
INCRD 332-6	Jacobsite magnesian - $(Mg_{0.735}Mn_{0.284}Zn_{0.017}Fe_{1.908}Al_{0.048}Mn_{0.045})O_4$, Trachyphonolite (?) - $(Mg,Fe,Al,Ti)(Ca,Fe,Na,Mn)(Si,Al)_2O_6$, Augite - $Ca(Fe,Mg)Si_2O_6$, Galenobismutite - $PbBi_2S_4$	Calc-silicate gneiss, magnetite skarn, anhydrite
INCRD 332-7	Trachyphonolite - $(Mg,Fe,Al,Ti)(Ca,Fe,Na,Mn)(Si,Al)_2O_6$, Anhydrite - $Ca(SO_4)$, Meionite sodian (Scapolite) - $Ca_{4.17}Na_{3.31}K_{0.46}Si_{14.99}Al_{8.69}O_{48}Cl_{0.73}(SO_4)_{0.37}(CO_3)_{0.87}$, Quartz, Andesine (30-50% ca plagioclase-feldspar)	Calc-silicate gneiss, magnetite, pyroxene, anhydrite

INCRD 332-8	Magnesioferrite (magnetite series), Pyroxene [Trachyphonolite-$(Mg,Fe,Al,Ti)(Ca,Fe,Na,Mn)(Si,Al)_2O_6$], Calcite, Kalinite - $KAl(SO_4)_2.11H_2O$	Mottled calc-silicate gneiss, magnetite, anhydrite/gypsum
INCRD 332-9	Hornblende, Albite-calcian, Diopside - $CaMgSi_2O_6$	Leuco granite + calc-silicate
INCRD 332-10	Albite-calcian, Quartz, Anhydrite – $Ca(SO_4)$	Leucocratic granite, hydrothermally altered, fault
INCRD 155-1	Quartz, Microcline, Albite	Granite
INCRD 155-2	Magnetite, Hematite, Hornblende (Mg-Hb, Fe^{2+}), Quartz, Russellite	Massive magnetite with mm scale calcite veins, iron skarn, mottled calc-silicate rock
INCRD 155-3	Magnetite, Quartz, Hornblende	Mottled calc-silicate - fracturing/cavities/calcite
INCRD 155-4	Quartz, Calcite, Hematite, Hornblende, Clinoclore $((Mg_{2.8}Fe_{1.7}Al_{1.2})(Si_{2.8}Al_{1.2})O_{10}(OH)_8)$	Mottled calc-silicate, magnetite
INCRD 155-5	Albite (calcian), Hornblende, Quartz, Phlogopite	Biotite gneiss (migmatitic with proxene and biotite + felsic (quartz/feldspar leucomes)),

		hydrothermal veins (-+ calcite and quartz)
INCRD 155-6	Quartz, Albite (calcian), Hornblende, Phlogopite	Biotite gneiss (slightly migmatitic, hydrothermal cavities with calcite
INCRD 155-7	K-feldspar, Albite, Quartz, Phlogopite ($KMg_3(Si_3Al)O_{10}(OH)_2$	Granite, coarse grained - pegmatitic
INCRD 155-10	Quartz, Albite (calcian), Hornblende, Roscoelite - $KAlV_2Si_3O_{10}(OH)_2$	Biotite gneiss, massive
INCRD 155-11	Quartz, Biotite, Albite, Riebeckite - $(Na,Ca)_2(Fe,Mn)_3Fe_2(Si,Al)_8O_{22}(OH,F)_2$; Clinochlore - $(Mg,Al)_6(Si,Al)_4O_{10}(OH)_8$	Mottled biotite gneiss
INCRD 155-12	Quartz, Microcline, Albite, Phlogopite	Granite, coarse grained, biotite
INCRD 155-13	Quartz, Microcline, Albite, Biotite	Granite, coarse grained, biotite
INCRD 155-14	Albite (calcian), Quartz, Phlogopite	Biotite gneiss, massive
INCRD 155-15	Magnetite, Hematite, Phlogopite	Massive magnetite, Reddish brown weathering, some cavities

Granite and biotite gneiss/schist samples from borehole INCRD 277 predominantly comprises of expected mineral assemblages of granitic and metapelitic compositions as well as mineral assemblages of hydrothermal origin such as phlogopite, calcite, and anhydrite, Table 4.1. Mineral assemblages from borehole 332 reflect sample rock type of calc-silicate amphibolite and

hydrothermal related minerals of magnetite, quartz, andesine, scapolite, galenobismutite ($PbBi_2S_4$) and anhydrite, Table 4.1. Magnetite is the dominant mineral assemblage in the samples from borehole INCRD 155. However, quartz, calcite and hornblende is abundant in samples of mottled calc-silicate and biotite gneisses. Other mineral assemblages associated with magnetite are phlogopite, chlinochlore, riebeckite, roscoelite and hematite, Table 4.1.

4.1.1 Mineral Petrography of Metasedimentary rocks

Diverse mineral assemblages such as magnetite, pyroxene, amphibole, calcite, quartz, calcian albite, biotite, phlogopite, anhydrite, kalinite - $KAl(SO_4)_2.11H_2O$, scapolite, clinoclore - $[(Mg_3Fe_2Al)(Si_3Al)O_{10}(OH)_8]$, and russellite dominate the calc-silicate rocks of the samples from the three studied boreholes. These mineral assemblages manifest a granoblastic texture ranging from straight grain boundaries to irregular contact, Fig. 4.1 and 4.2.

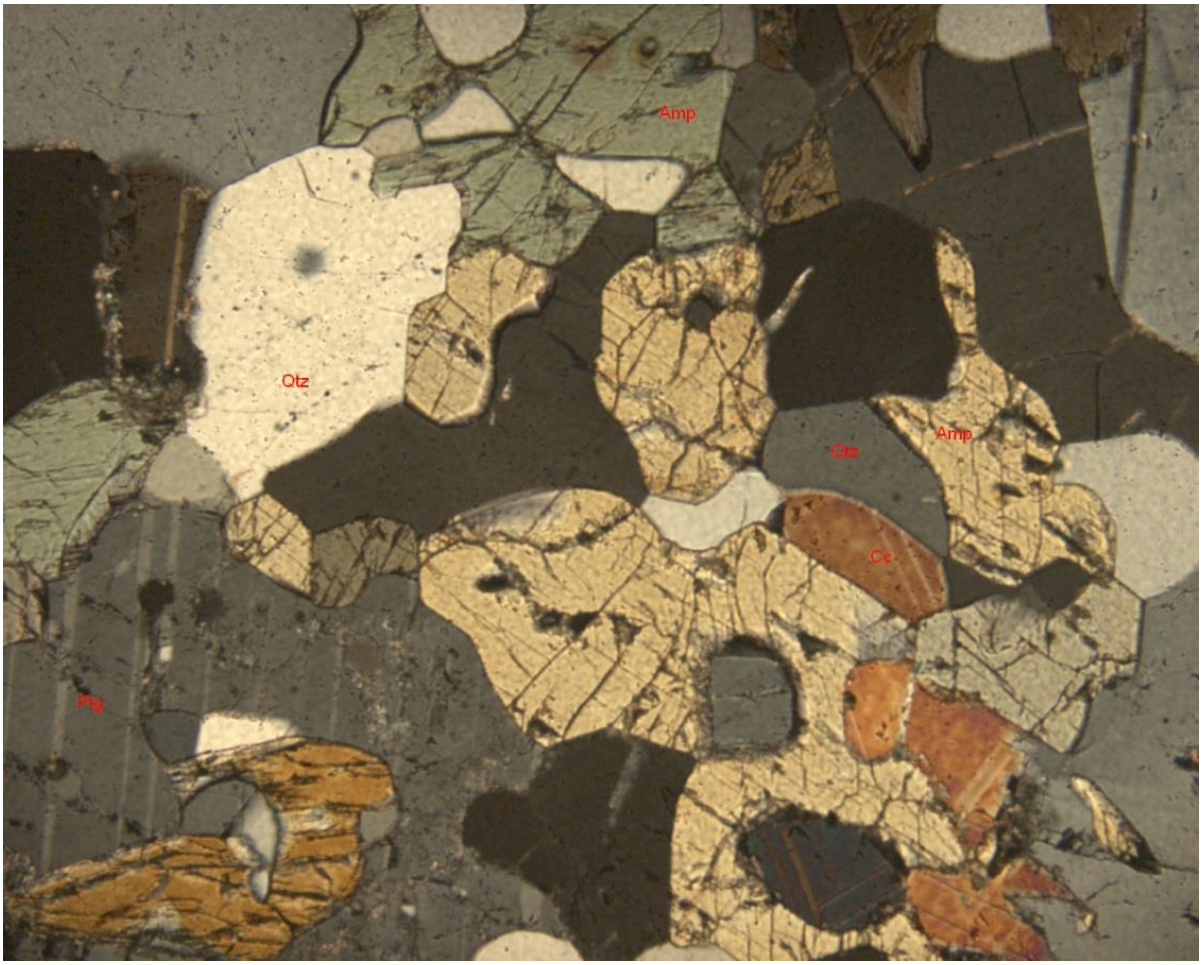

Figure 4.1. Granoblastic interbolate texture of calc-silicate rock under cross-polarised transmitted light microscope. Plg –plagioclase, Cc – calcite, Amp – hornblende, Qtz – quartz. 10x magnification, field of view 10mm.

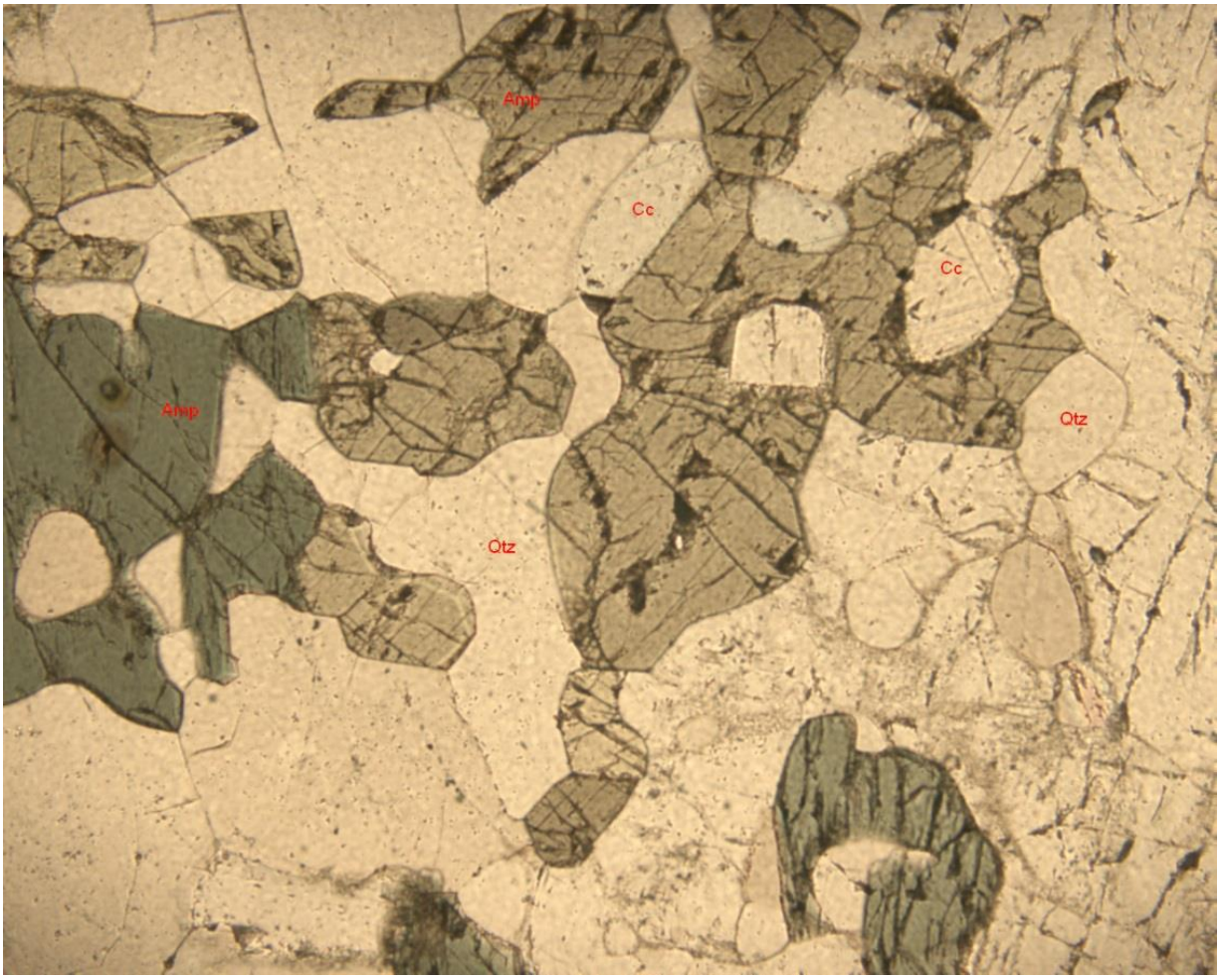

Figure 4.2. Ganoblastic interbolate texture of calc-silicate rock under plane-polarised transmitted light microscopy. Plg –plagioclase, Cc – calcite, Amp – hornblende, Qtz – quartz. 10x magnification, field of view 10mm.

Hydrothermal replacement textures are observed along grain boundaries and along cleavage planes as well as along lamellae of some mineral phases, Fig. 4.3 to 4.7. The original metasedimentary rocks have been pervasively obscured by hydrothermal magnetite and the remnant metasedimentary rocks often observed in thin sections as xenoblastic and skeletal features in a groundmass of granoblastic magnetite, Fig. 4.3 and 4.4.

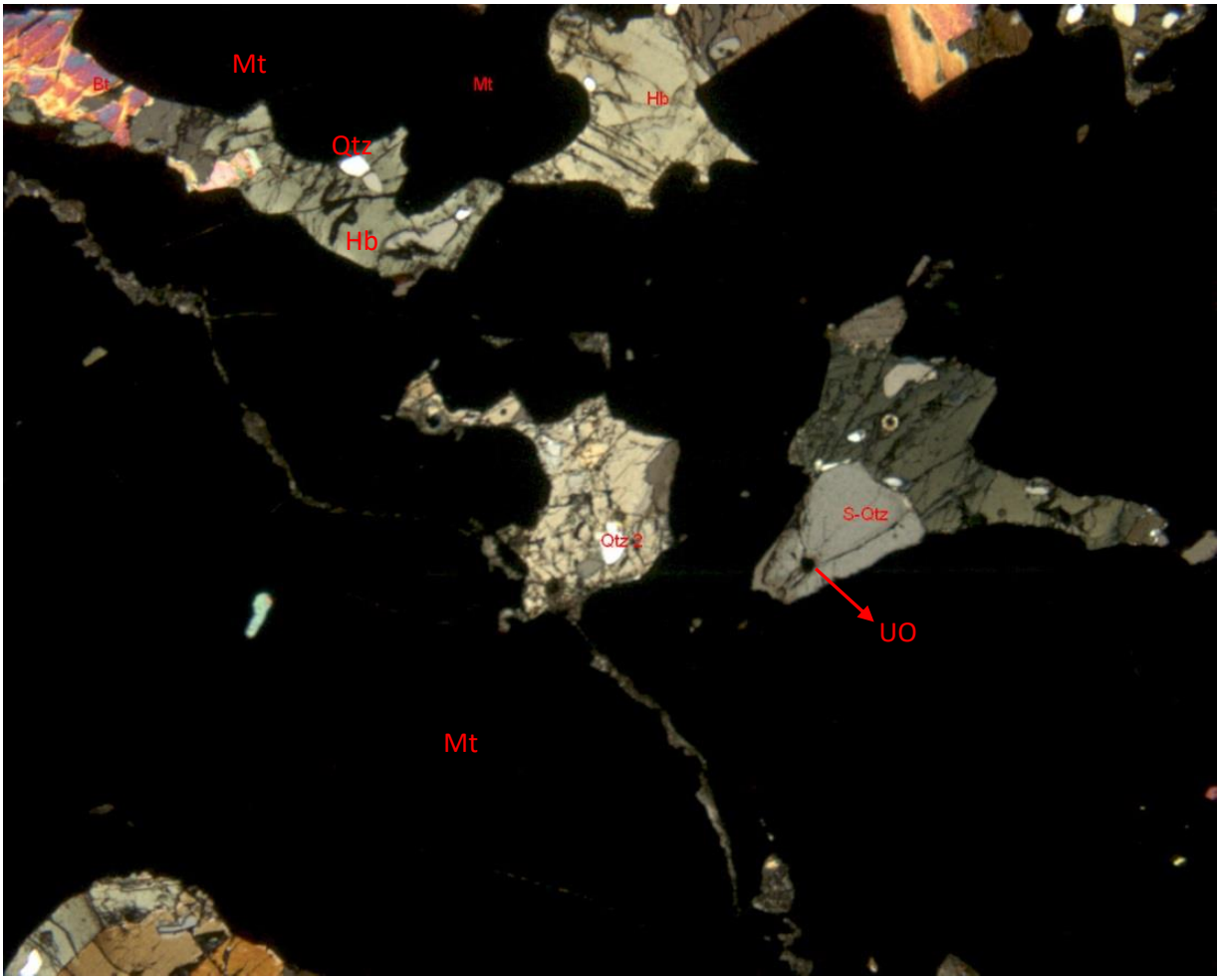

Figure 4.3. Photomicrograph showing magnetite replacement texture in the calc-silicate rock. Fracture (vein) filled by silicate mineral assemblages. UO – rare cob-web uraninite; S-qtz is smoky quartz; Mt-magnetite; Qtz 2 - hydrothermal quartz, Hb-hornblende, Bt- biotite, under transmitted polarised light microscope, 4x magnification, field of view 10mm.

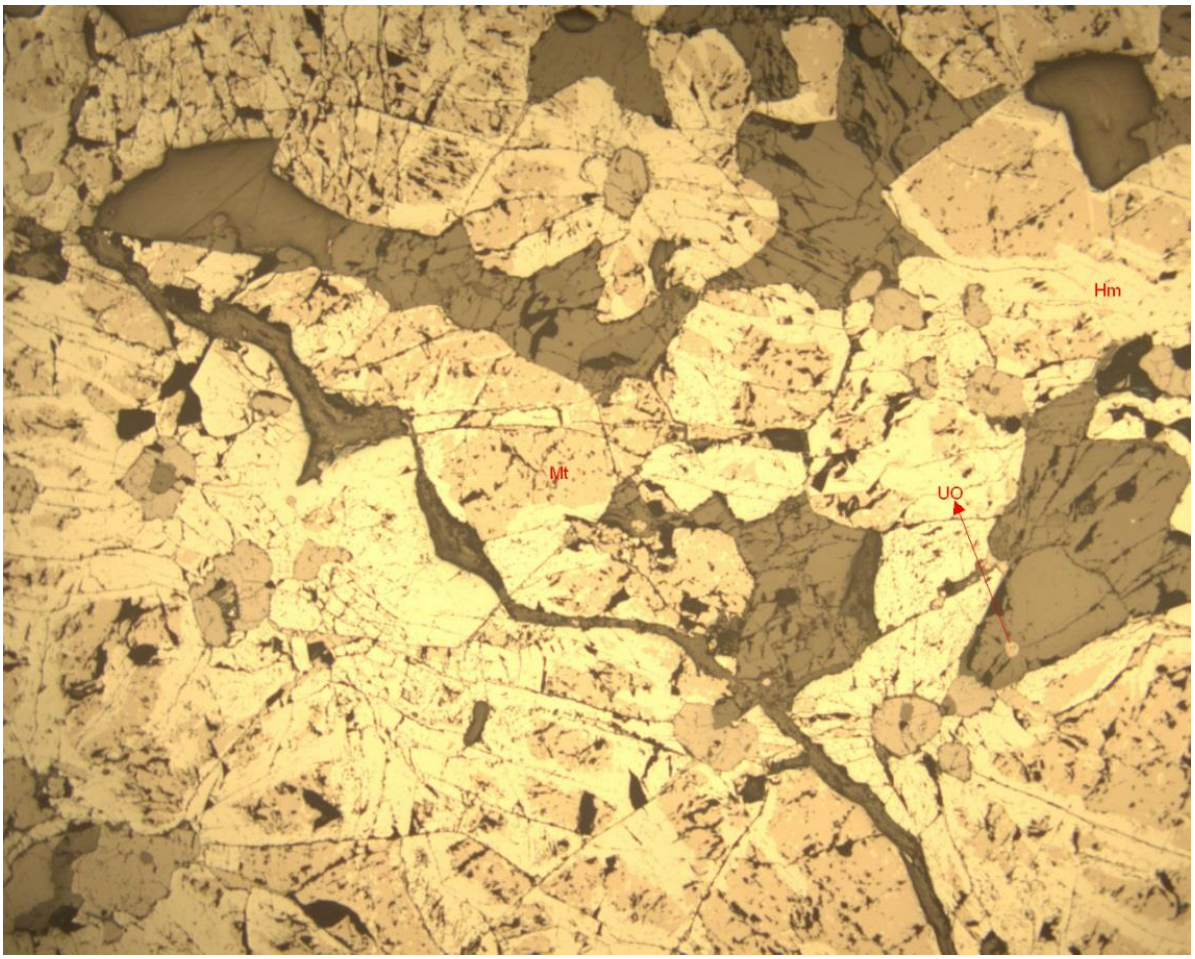

Figure 4.4. Reflected photomicrograph depicting magnetite (Mt) and hematite (Hm) replacement texture as well as rare micro cob-web uraninite (UO) grain associated with quartz in bottom left corner under plane-polarised reflected light microscope, 10x magnification, field of view10 mm.

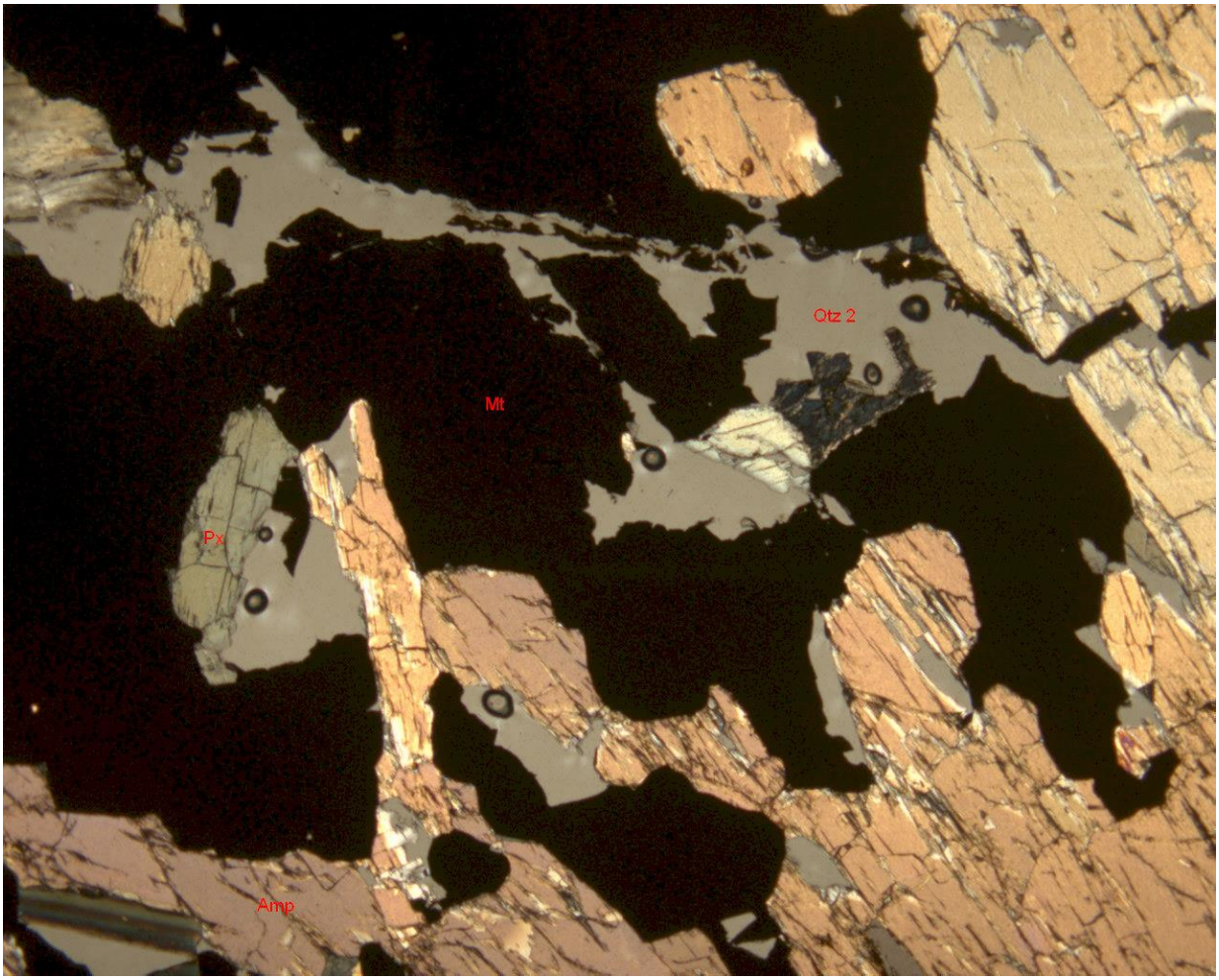

Figure 4.5. Replacement textures of quartz (Qtz-2, pale-grey) and magnetite (Mt, black) along cleavage planes in hornblende (Amp) and pyroxene (Px) rich calc-silicate rock, 4x magnification, field of view 10mm

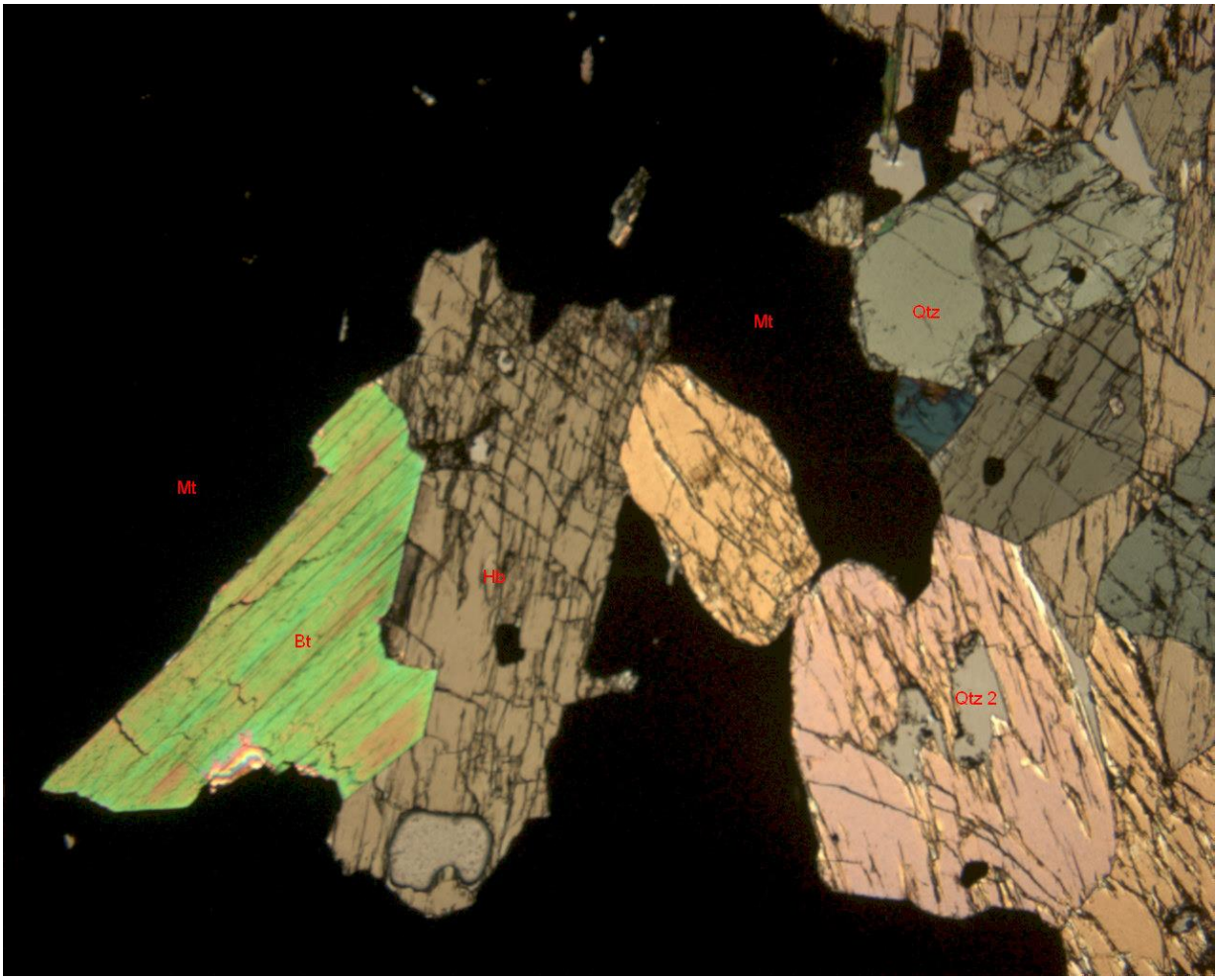

Figure 4.6. Replacement texture under transmitted cross polarised light microscope: biotite (Bt) replacing hornblende (Hb), quartz (Qtz-2) replacing hornblende and Mt replacing bitotite, quartz and hornblende in a calc-silicate protolith. 4x magnification, field of view 10mm

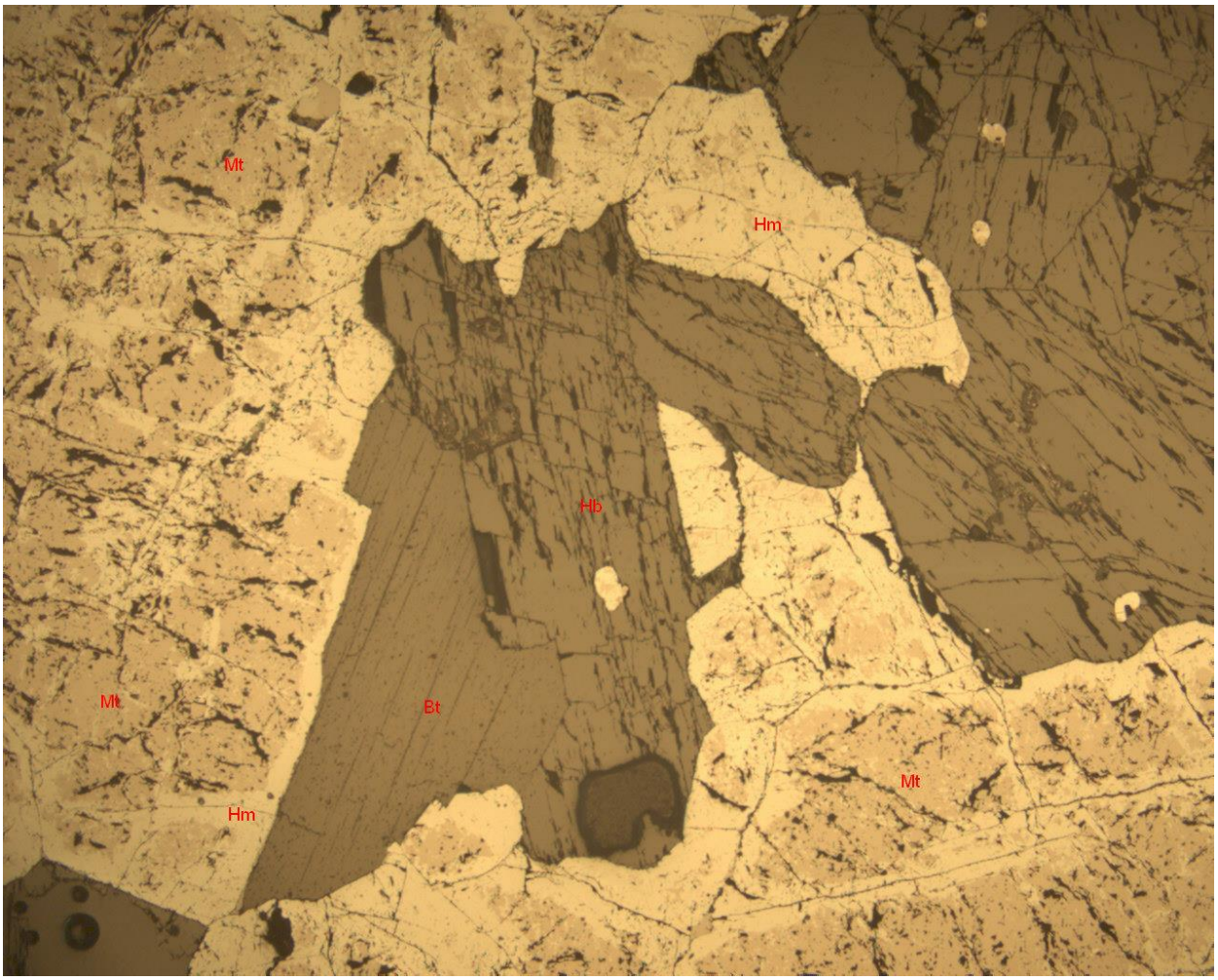

Figure 4.7. Replacement texture under reflected polarised light microscope: biotite (Bt) replacing hornblende (Hb), quartz (Qtz-2) replacing hornblende and Mt replacing bitotite, quartz and hornblende in a calc-silicate protolith. Magnetite is replaced by hematite along grain boundaries and fractures. 4x magnification, field of view 10mm

Amphiboles (hornblende) have been hydrothermally replaced along cleavage planes by biotite, quartz and magetite along cleavage planes, Fig. 4.6 and Fig. 4.7. The replacement of magnetite by hematite along grain boundaries and fractures represents the last reaction texture, Fig 4.7. The

granoblastic polygonal textured calcite is one of the primary minerals and has been replaced along its grain boundary by silicification reactions and randomly replaced by magnetite, Fig. 4.8.

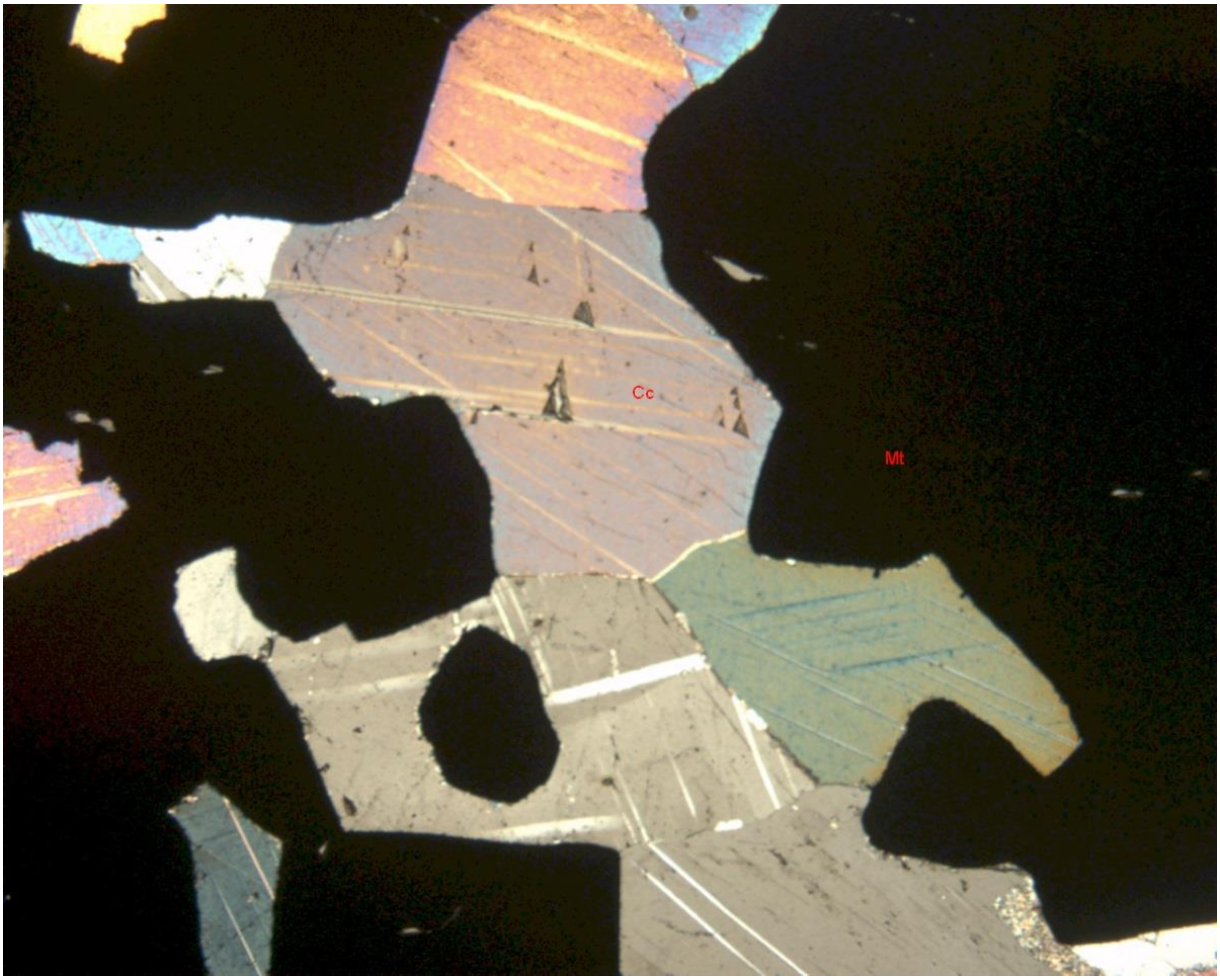

Figure 4.8. Granoblastic polygonal texture calcite (Cc) is replaced by magnetite (Mt- black). Under cross-polarised transmitted light, 10x magnification, field of view 10mm

Magnetite appears to be the last hydrothermal mineral phase, and the predominant replacement mineral in the calc-silicate rock, that replaces all mineral assemblages including earlier replacement textures and hydrothermal reaction products, Fig. 4.5 to 4.8. Magnetite occurs along

grain boundaries, cleavage planes, as fracture fills (veinlets) and cross cutting grains of original mineral assemblages, Fig. 4.5 and Fig. 4.8.

Biotite gneiss rocks of the three boreholes consist of varied mineral assemblages such as quartz, biotite, calcian albite, riebeckite - $(Na, Ca)_2(Fe, Mn)_3Fe_2(Si, Al)_8O_{22}(OH,F)_2$; roscoelite - $KAlV_2Si_3O10(OH)_2$, clinochlore - $(Mg, Al)_6 (Si, Al)_4 O_{10} (OH)_8$, graphite, muscovite, phlogopite - $(KMg_3 (Si_3Al) O_{10} (OH)_2$, and diopside - $CaMgSi_2O_6$. Sericite and chlorite alteration has been locally observed along cleavage planes of feldspar and biotite.

4.1.2 Mineral Petrography of Granites

The medium to coarse-grained granites from the three boreholes exhibit equigranular texture and their mineral grain contacts varies from straight to irregular. The granite rocks range from pale-grey (leucgranite) to pale-pink and pink in colour, and are predominantly comprised of quartz, albite, calcian albite, microcline, biotite, and anhydrite. In most granites, the dominant feldspar is albite and calcian albite and often depict hydrothermal reaction as manifested by sericite and silicification alterations along cleavage planes, Fig. 4.9. Chlorite alteration depicted by replacement of biotite by chlorite has been observed in interstitial sites of granites and appears to predate silicification, Fig. 4.9. Association of anhydrite with calcian albite reflects a spatial association around contact between calc-siicate gneiss and leucogranites. Quartz–sericite-magnetite replacement textures of plagioclase, quratz and biotite and biotite occurs along grain boundaries, cleavage planes, and cut across grains of original mineral assemblages, Fig 4.9.

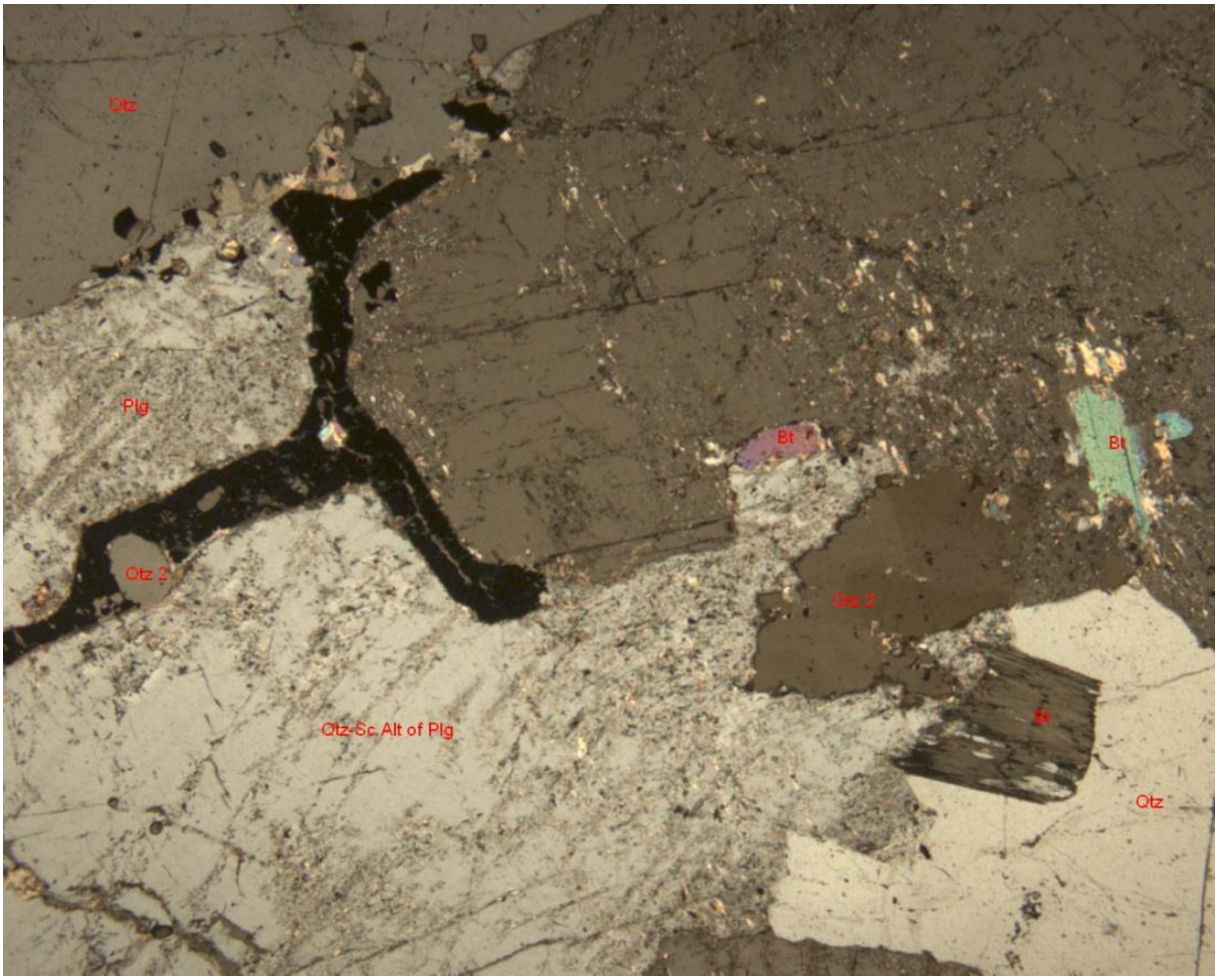

Figure 4.9. Quartz (Qtz-2) –sericite (Sc) - magnetite (Mt) replacement textures of plagioclase (Plg), quartz (Qtz) and botite (Bt) in a granite. Under cross-polarised transmitted light, 10x magnification, field of view 10mm

4.1.3 Mineral Petrography of the Iron skarn rock

The predominantly magnetite containing iron skarn rock is dark grey in colour and exhibit granoblastic and massive texture. The iron skarn rock represents an almost total magnetite replacement texture of a calc-silicate rock protolith as evidenced from relicts of calcite, quartz, pyroxene and hornblende that appears as skeletal features in a massive and granoblastic magnetite

groundmass, Fig. 4.10. Minor replacement textures of magnetite by hematite observed along grain boundaries and fractures across its grains represent the final hydrothermal reaction texture observed in this study, Fig. 11.

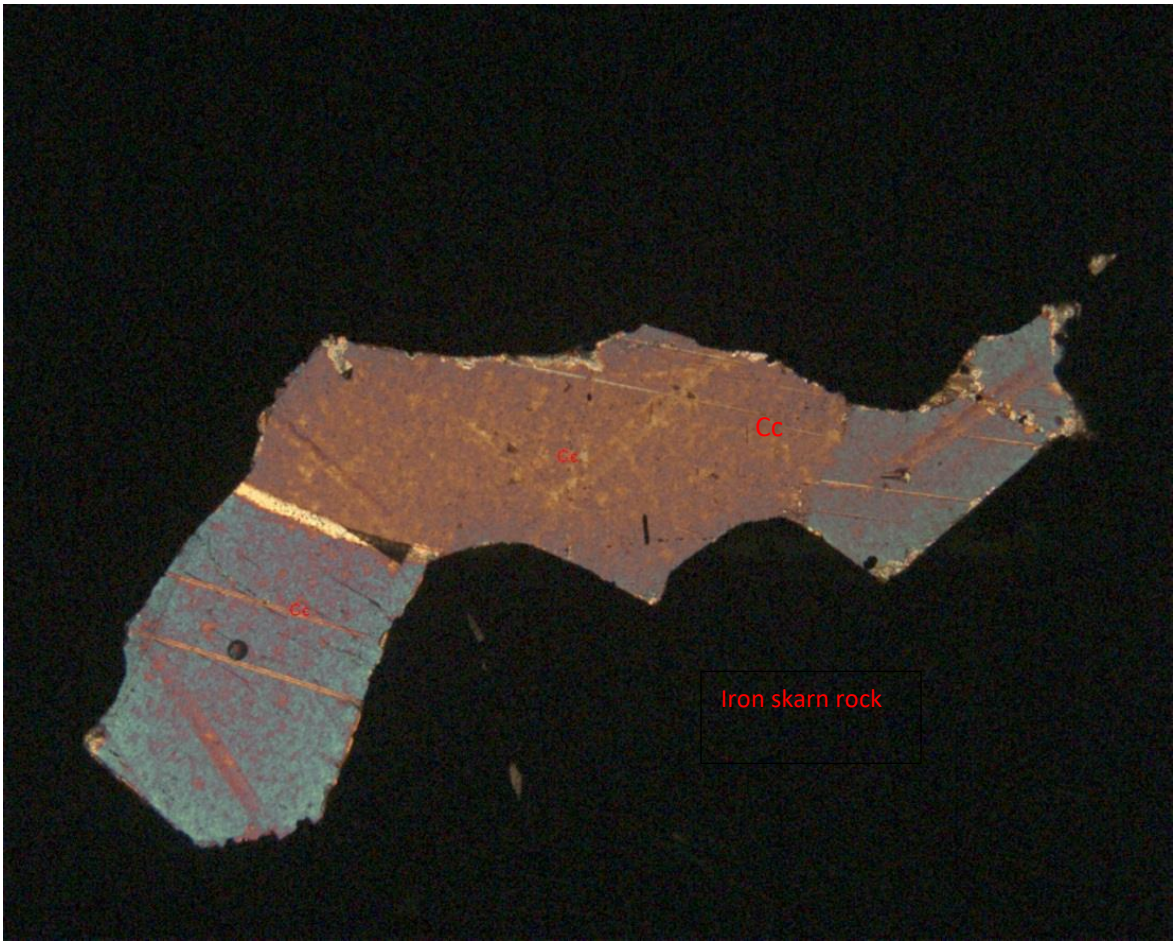

Figure 4.10. Photomicrograph of an iron skarn rock (black) with remnant calcite (Cc) aggregate of possibly a calc-silicate rock under cross-polarised transmitted light microscope, 10x magnification, field of view 10mm

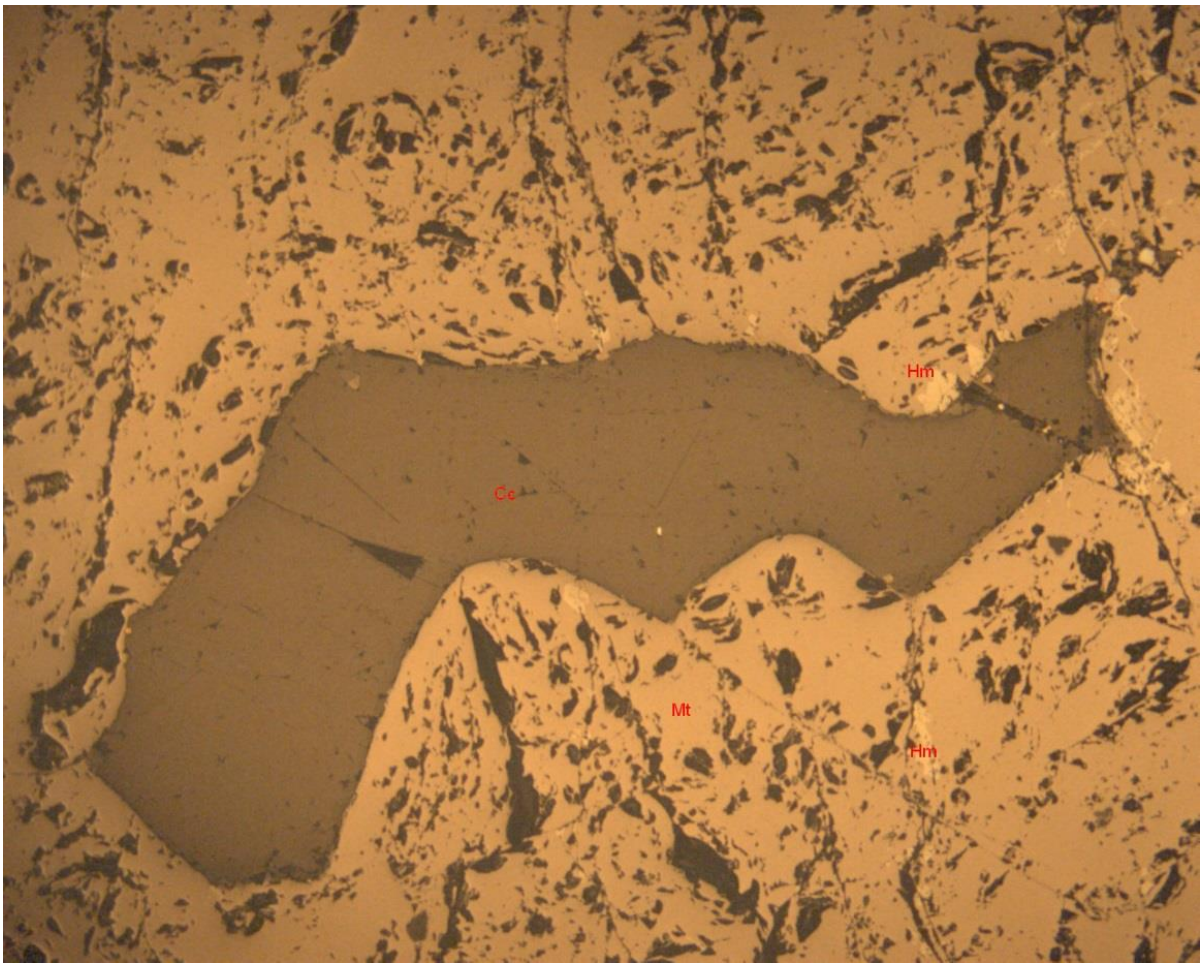

Figure 4.11. Photomicrograph of an iron skarn rock (black) with remnant calcite (Cc) aggregate of possibly a calc-silicate rock under cross-polarised transmitted light microscope, 10x magnification, field of view 10mm. Localised minor partial replacement of magnetite by hematite (Hm).

4.2 Scanning Electron Microscopy of selected U ore

Results of quantitative petrographic analysis of selected ore samples INCRD 155-8, INCRD 277-7 and -10, INCRD 322-2 are presented below as a description of their mineral phases and textural variations sections.

4.2.1 Mineral phases of samples

Magnetite is the most dominant iron oxides and is occasionally in spatial relationship with uranium mineralisation. The granoblastic polygonal to interbolate, subeuhendral magnetite grains has suffered brittle deformation evidenced by pervasive stock-work fractures. Magnetite grains alter to hematite along grain boundaries and fracture margins, Fig. 4.12.

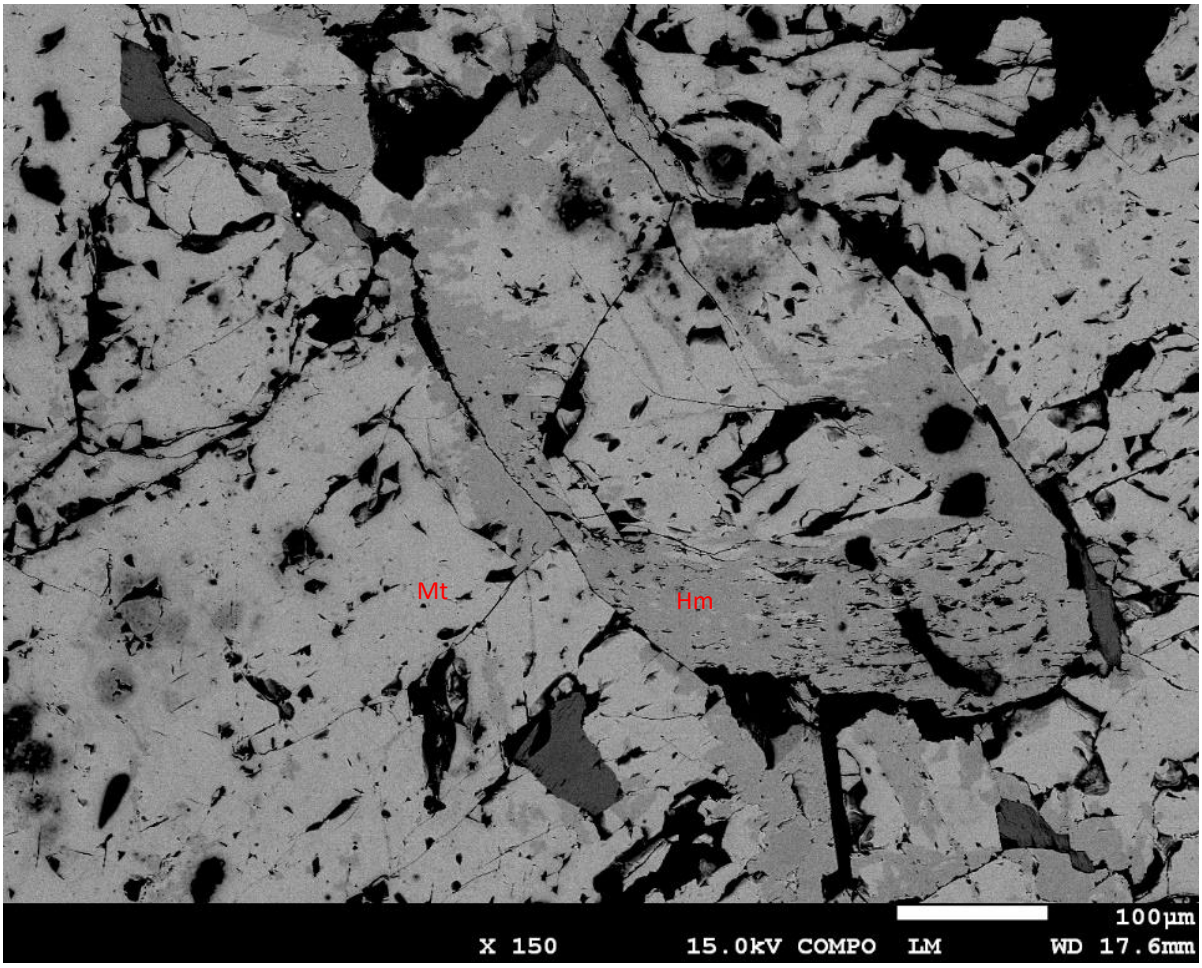

Figure 4.12. Granoblastic fractured magnetite pale grey colour (Mt) and hematite alteration in dark grey (Hm).

The uranium phases present in the ore containing samples are uranium oxide (uraninite -UO_2) and uranium silicate (coffinite- $USiO_4$) and are of relatively distinct temporal relationship. Uraninite occupy interstitial sites (Fig. 4.13) and also encloses magnetite (Fig. 4.14) in the iron skarn rock, occasionally altered to coffinite, as subeuhendral to subrounded grains in interstitial site of host minerals such magnetite and other silicate minerals.

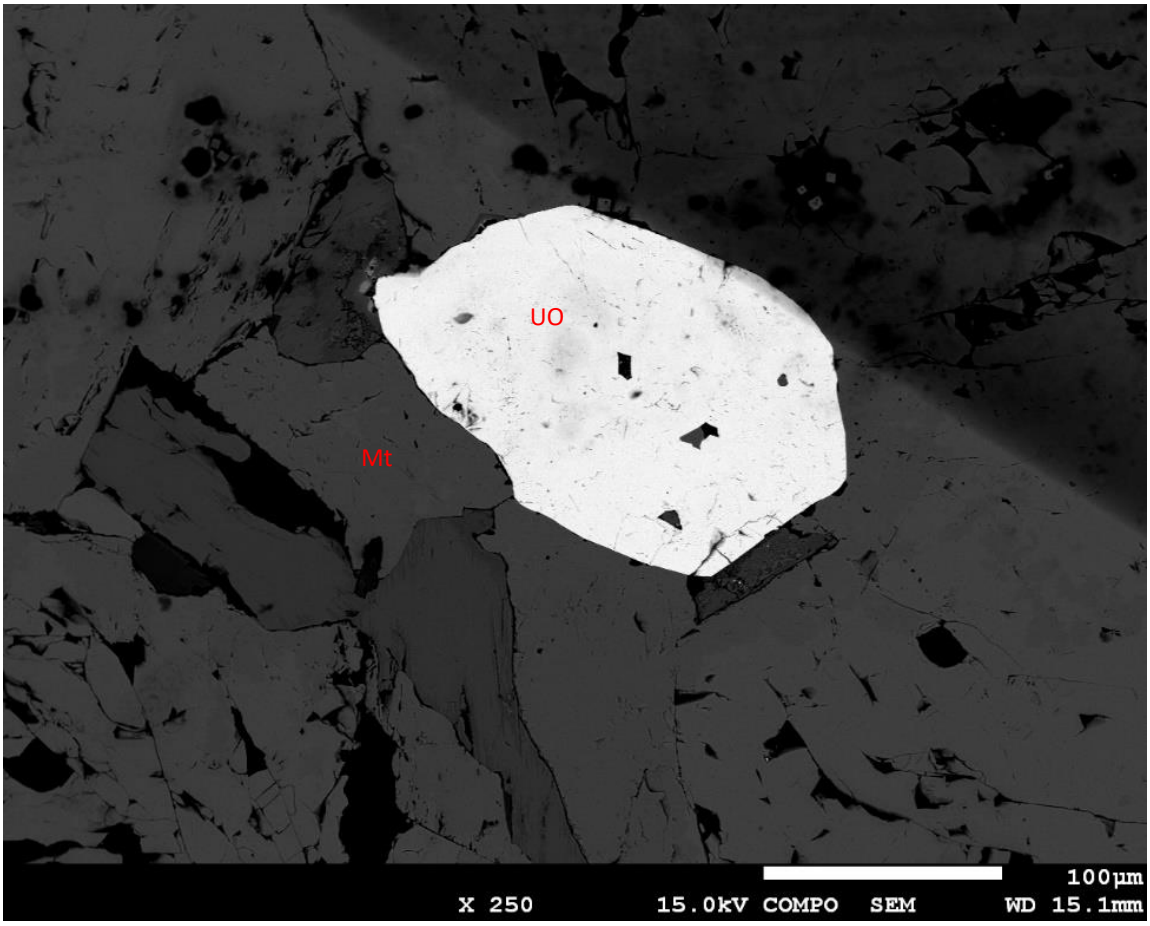

Figure 4.13. SEM photomicrograph showing somewhat-hexagonal, coarse-grained uraninite (UO) interlocked with magnetite (Mt, pale-grey). Dark grey shade in the top right corner is marker pen print on the slide.

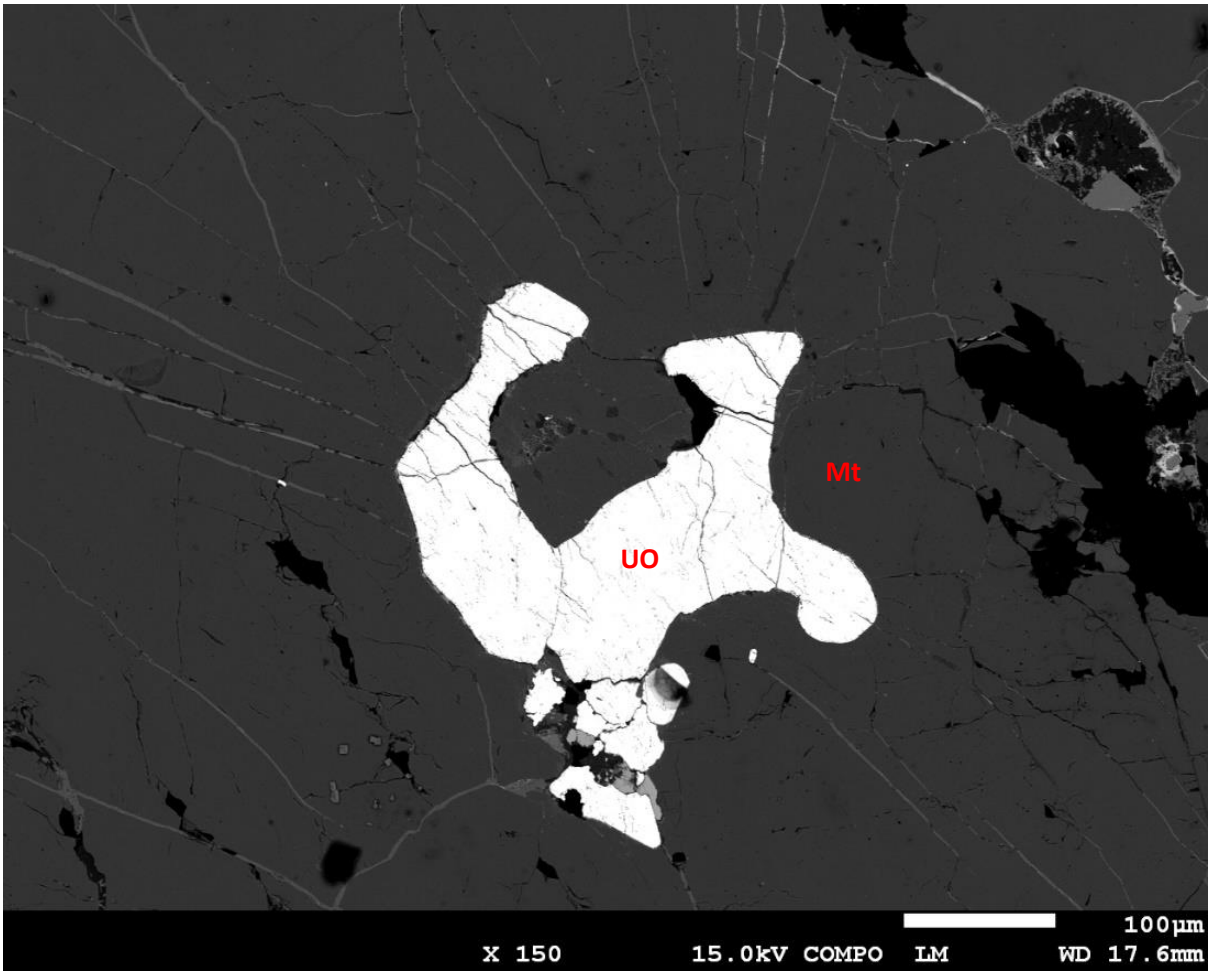

Figure 4.14. SEM photomicrograph of fractured uraninite (UO) exhibiting enclosing replacement texture hosted in fractured massive magnetite.

Coffinite is mainly confined to grain boundaries and fracture sites of uraninite and host minerals. However, in some portions of some rocks (e.g. calc-silicate) where silicification appears to have been intensive, coffinite can occur as massive and botryoidal in association with silicification products, Fig. 4.15. Similar to magnetite, uraninite manifests deformation in form of brittle fractures whereas coffinite generally does not show evidence of deformation. Coffinite occurrence is associated with sulphide and REE mineralisation, Fig. 4.16.

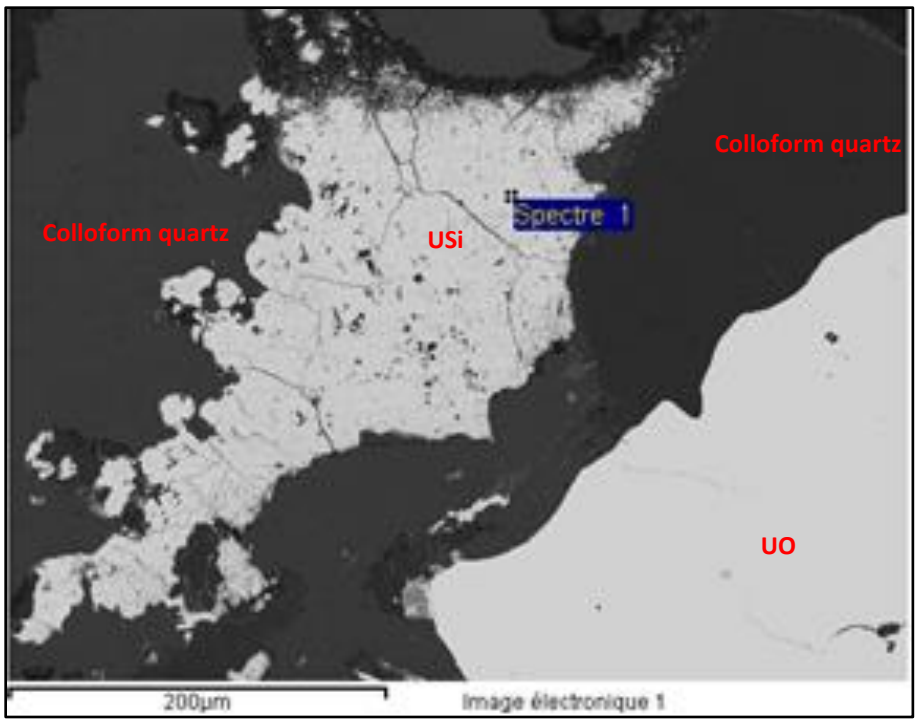

Figure 4.15. SEM photomicrograph of fractured coffinite (Spectre 1, USi) associated with Yttrium (xenotime) with silicification colloform texture around it. UO is uraninite.

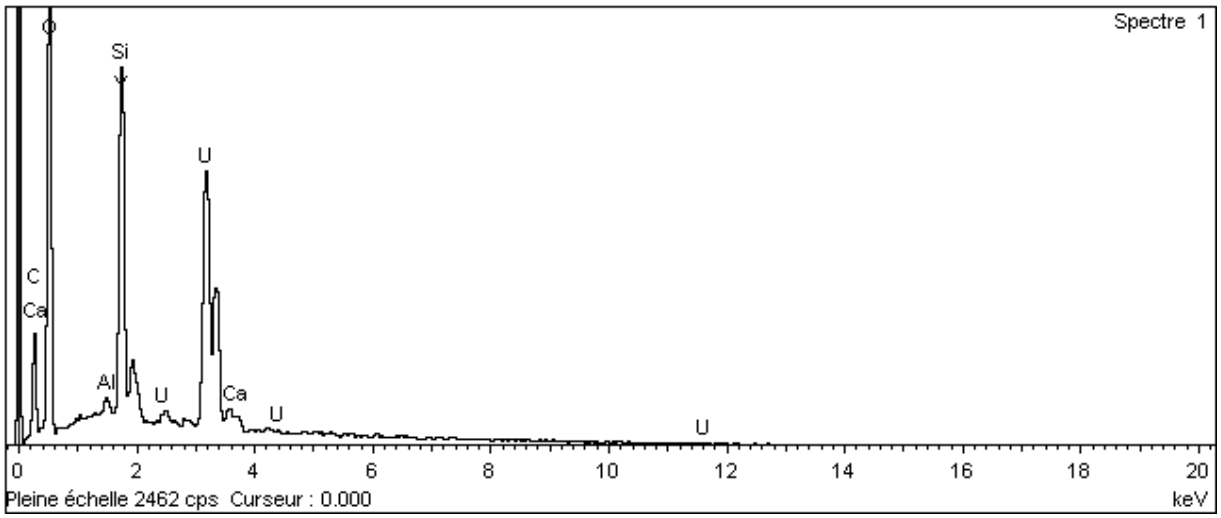

Figure 4.16. SEM spectral graph of fractured coffinite (Spectre 1, Fig. 23) associated with Yttrium (xenotime) with silicification colloform texture around it.

Spatial association of both coffinite and uraninite with other mineral assemblages such as hydrothermal quartz, calcite, diopside and apatite are observed, Fig. 17 to Fig 22.

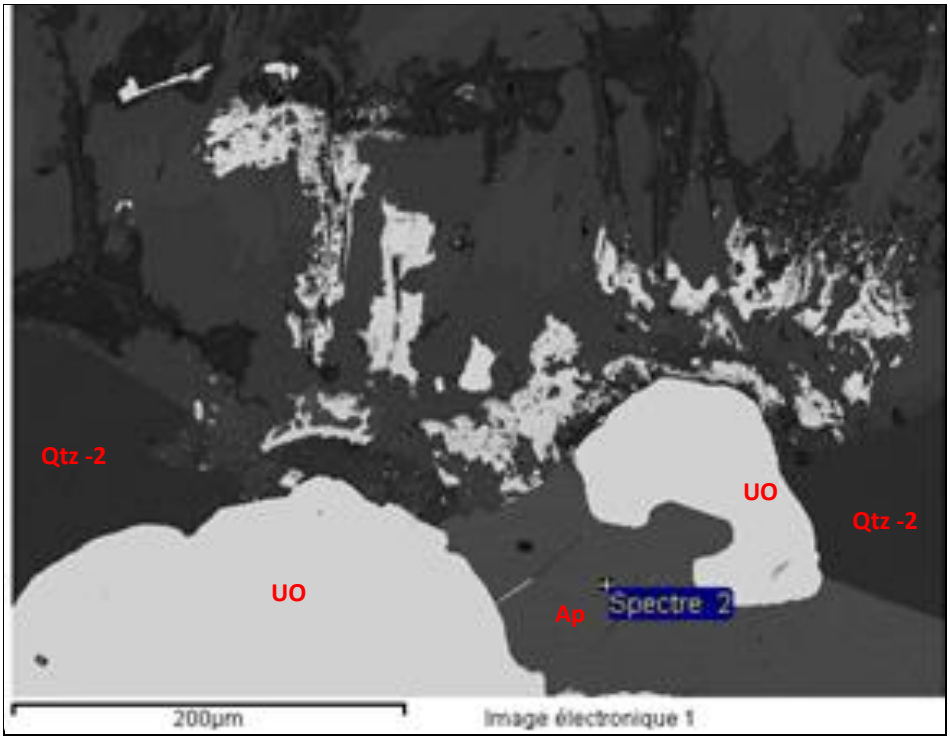

Figure 4.17. SEM photomicrograph of apatite (spectre 2, Ap) with fractures partly filled with hydrothermal uraninite (UO) mineralisation, and partly replaced by uraninite and quartz (Qtz-2).

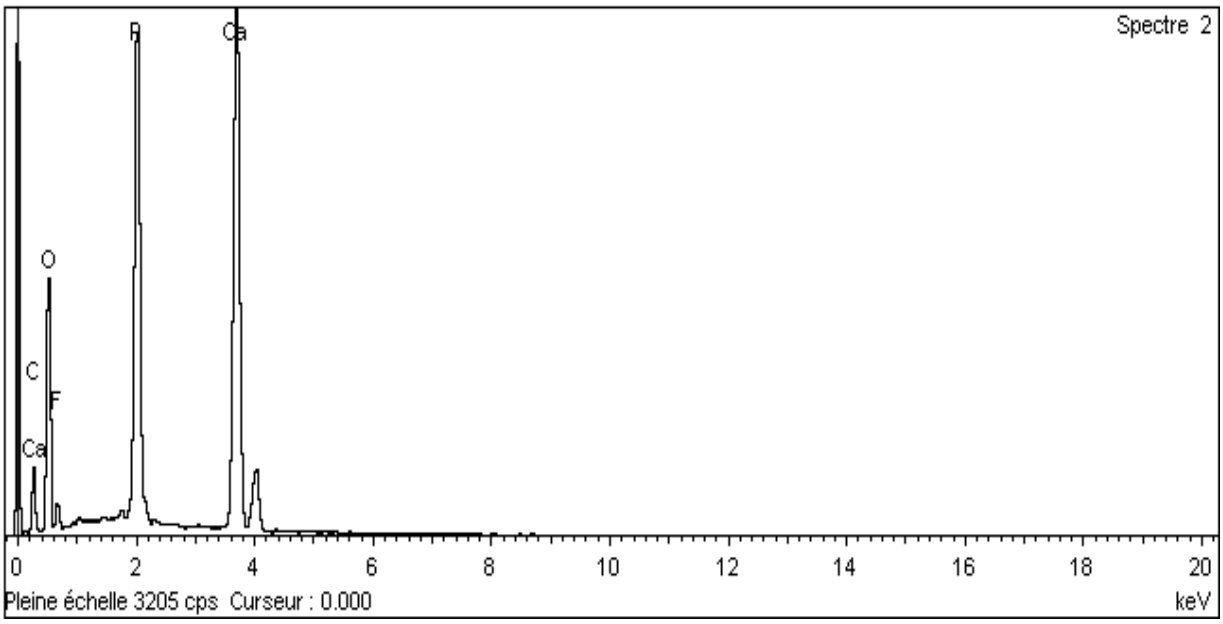

Figure 4.18. SEM photomicrograph of apatite (spectre 2 in Fig. 25).

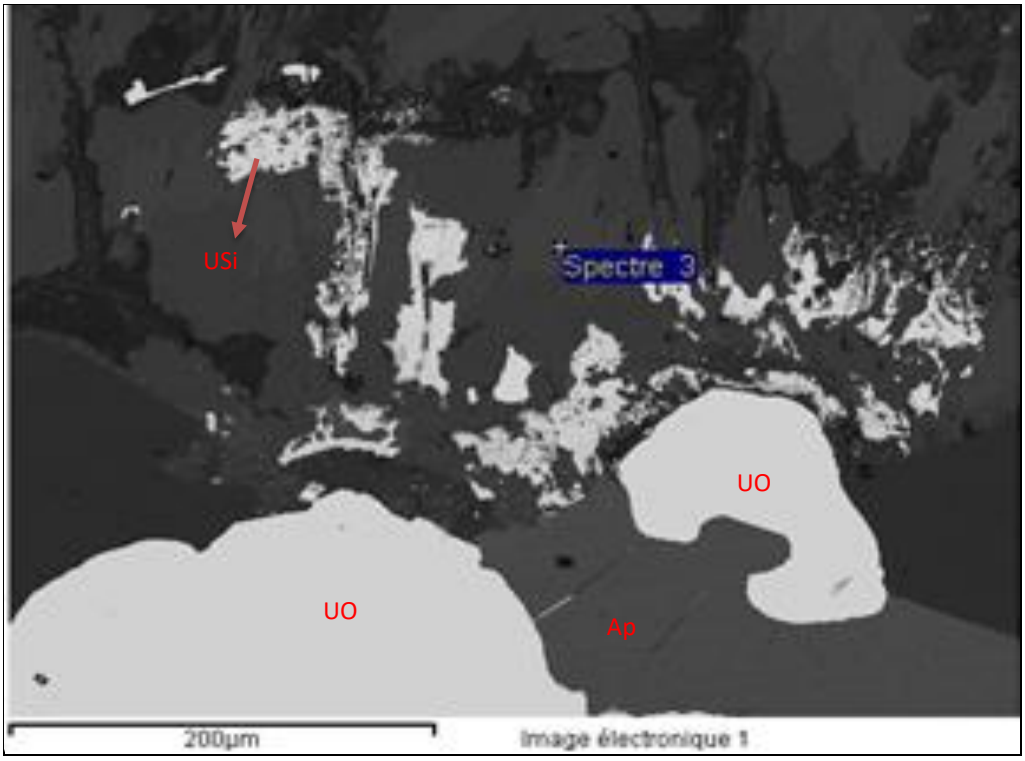

Figure 4.19. SEM photomicrograph showing uraninite (UO), Apatite (Ap), coffinite (USi) and diopside (Spectre 3) resident to hydrothermal mineralisation.

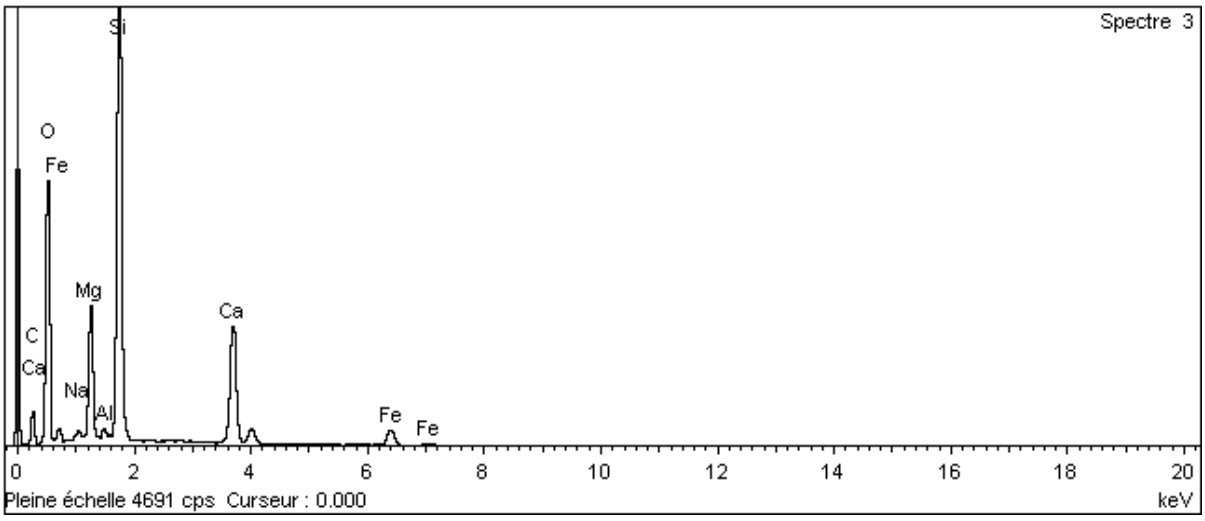

Figure 4.20. SEM spectral graph showing diopside (Spectre 3 in Fig. 4. 27).

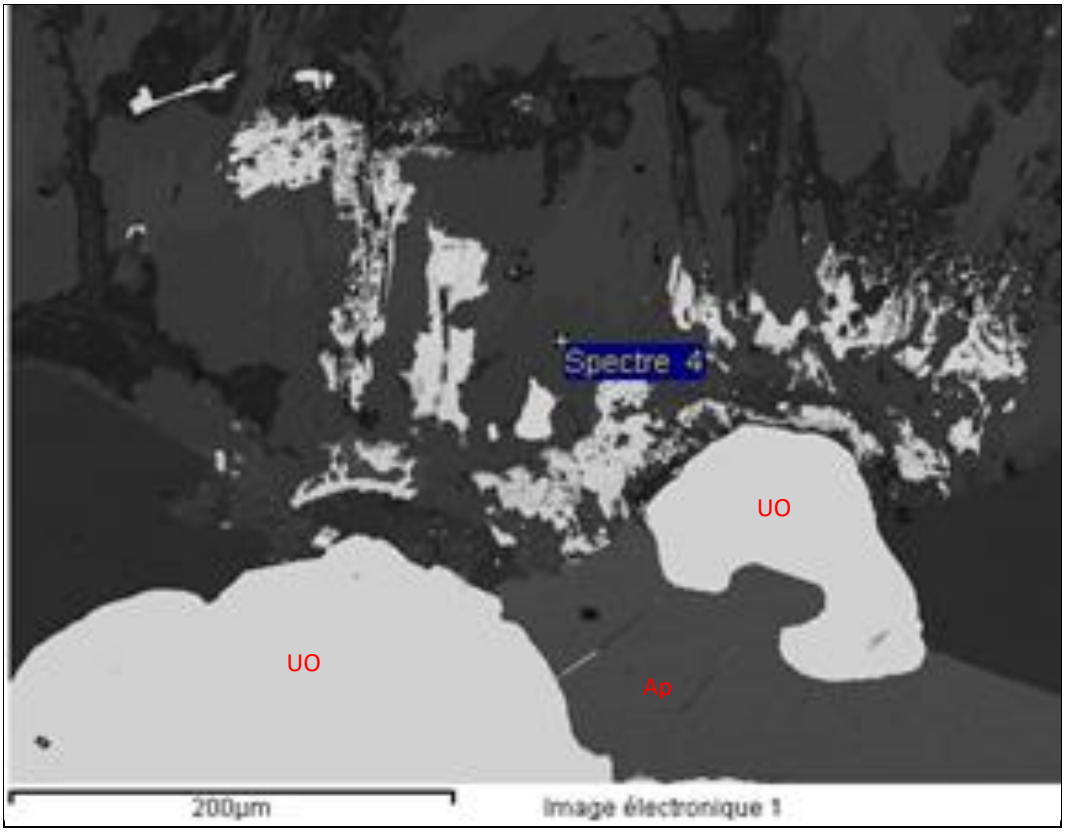

Figure 4.21. SEM photomicrograph of calcite (Spectre 4), apatite (Ap) and uraninite in host calc-silicate rock.

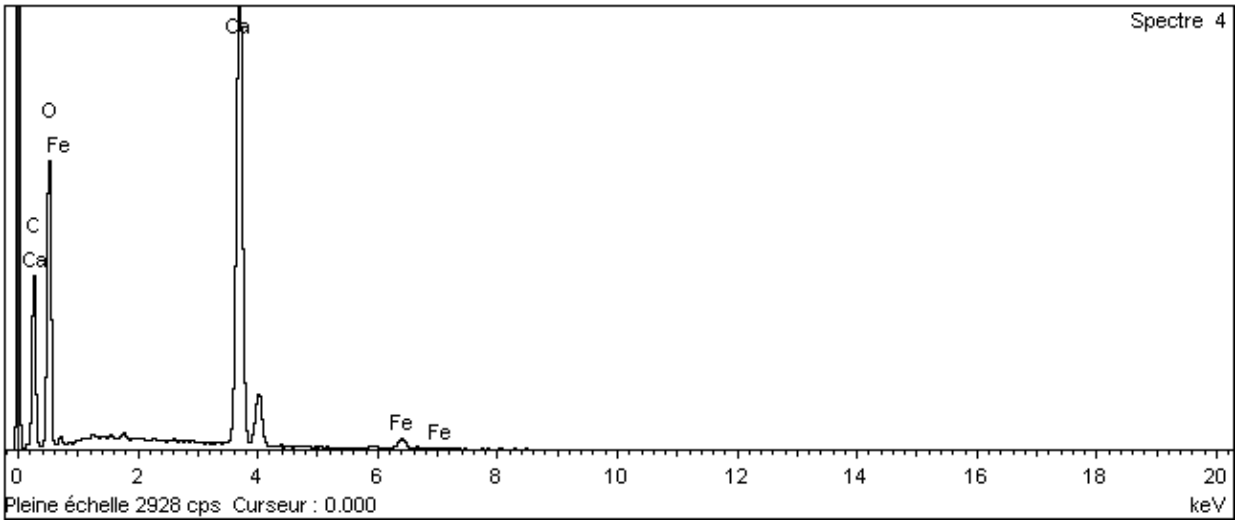

Figure 4.22. SEM spectral graph of calcite in host calc-silicate rock (Fig. 29).

Sulphide mineralisation occurs as galena, pyrite and chalcopyrite in association with coffinite and REE along grain boundaries and fracture zones as veins, e.g., Fig. 4.23 and Fig. 4.24. A spatial association of botryoidal or colloform coffinite and hydrothermal quartz with micro fractures and linear structures is suggestive of struatcural control on mineralisation, Fig. 4.25 to Fig. 4.27.

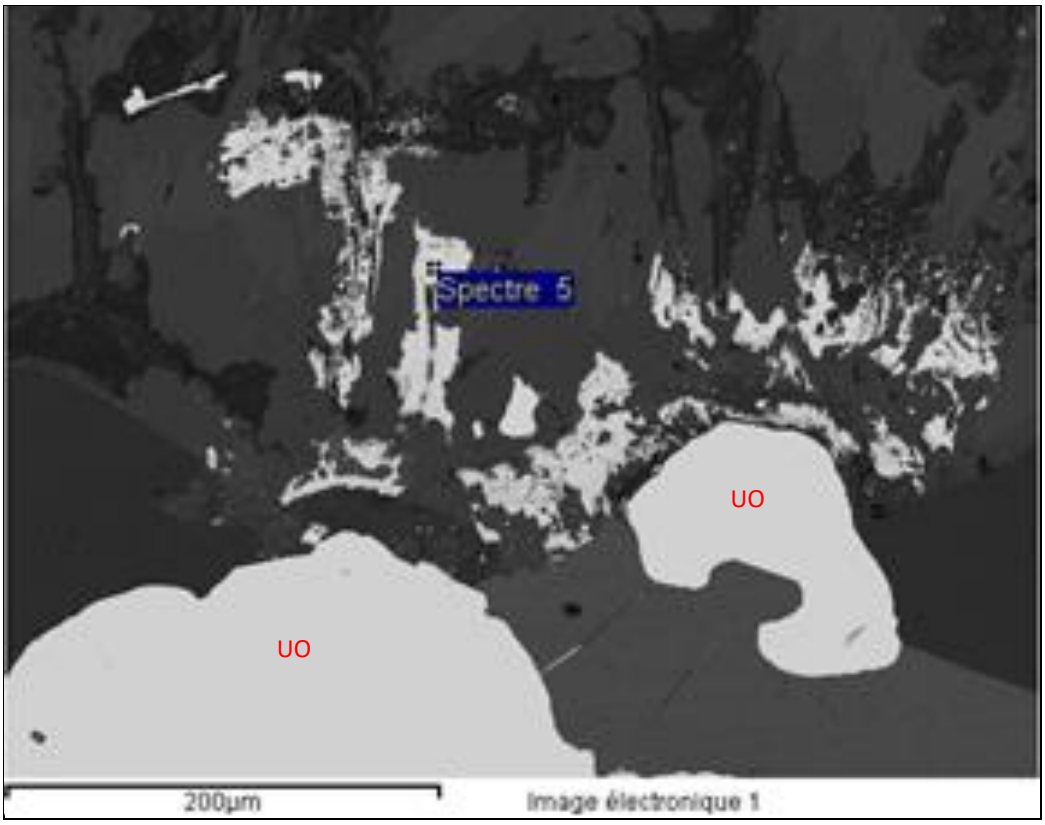

Figure 4.23**.** SEM photomicrograph of galena (spectre 5).

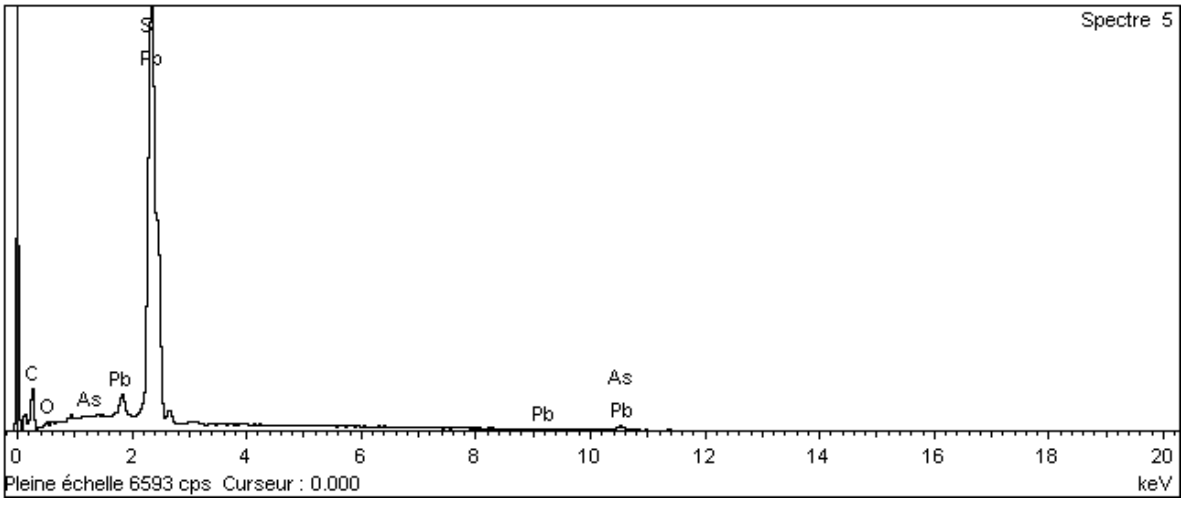

Figure 4.24. SEM spectral graph of galena (spectre 5, Fig. 4.23).

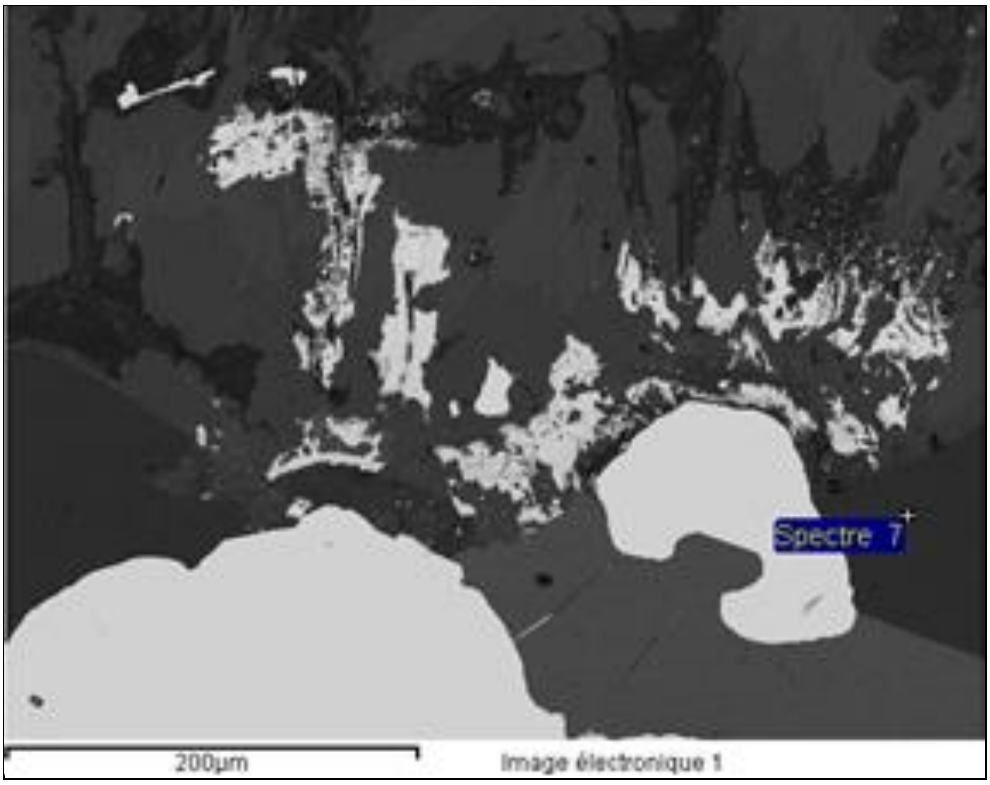

Figure 4.25. SEM photomicrograph of hydrothermal quartz (Spectre 7) replacing apatite.

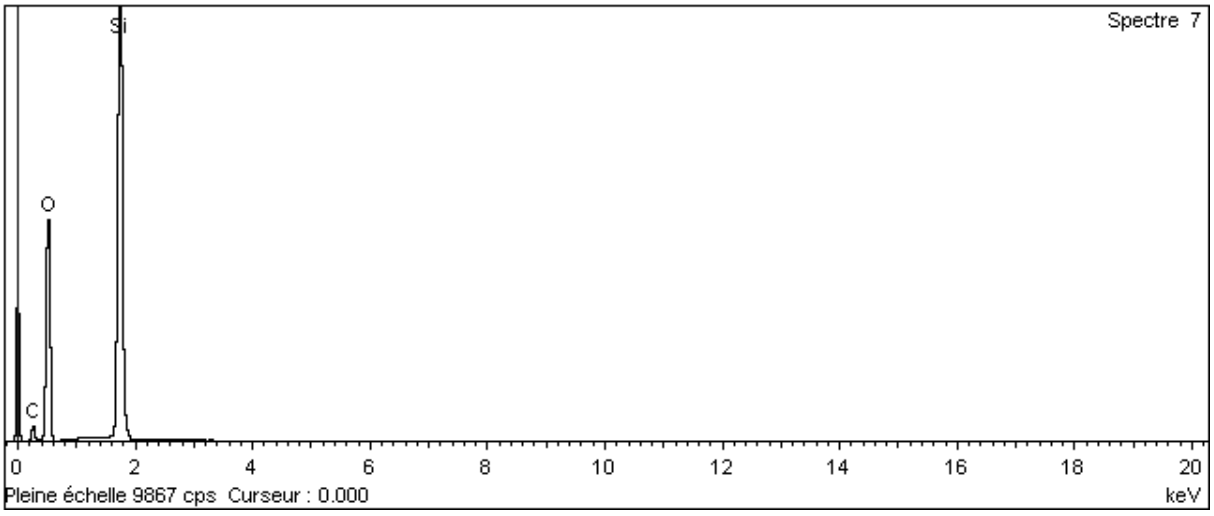

Figure 4.26. SEM spectral graph of hydrothermal quartz (Spectre 7, Fig. 4.25).

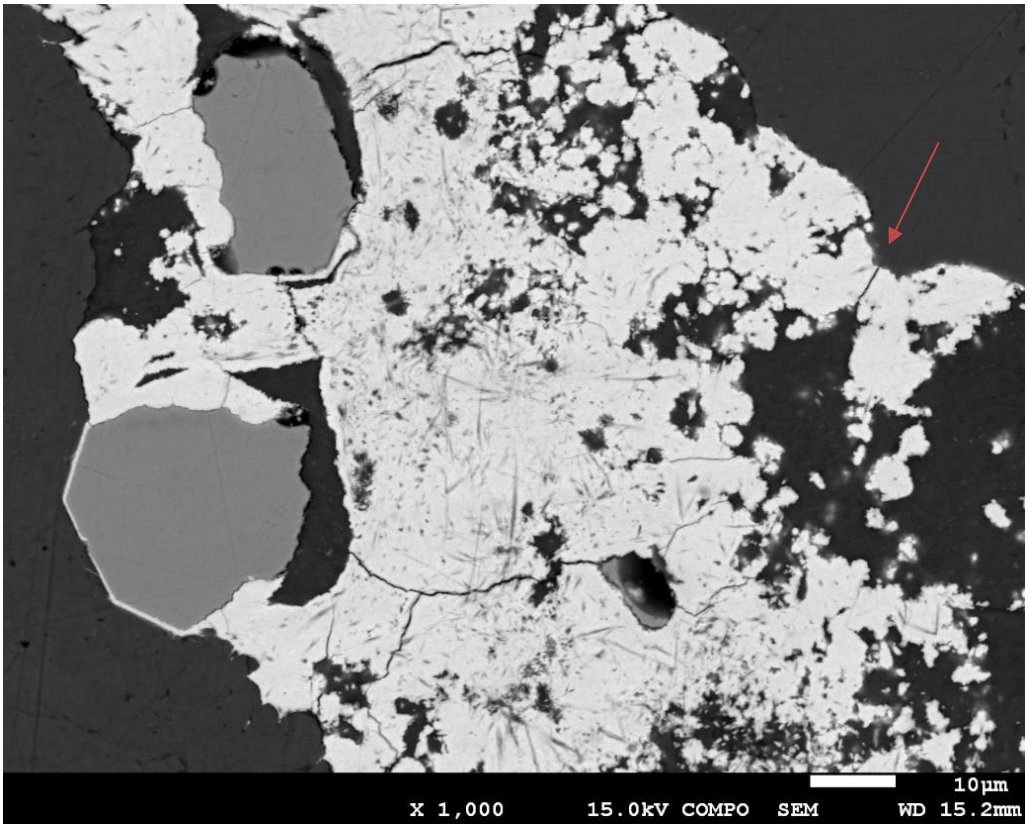

Figure 4.27. SEM photomicrograph showing massive botryoidal or colloform coffinite (white colour) with undistinguished needle-like mineral within calc-silicate rock. Red arrow depicts an inferred overprinted linear structure.

4.2.2 Textural characteristics of U ore

Granoblastic textures represent the principal mode of occurrences of host mineral assemblages of metasedimentary rocks and iron skarn rock in the ore samples, (Fig. 4.28 to FFig. 4.35). The granoblastic texture in these samples is manifested by medium to coarse grained equigranular arrangement, whose grain contacts varies from polygonal to interbolate with straight-line grain boundaries to somewhat irregular boundaries of both oxide and silicate minerals. Alteration appears to be responsible for undulating and irregular grain boundaries of otherwise straight-line grain boundaries of host mineral assemblages.

Replacement textures represent evidence for hydrothermal reaction and resultant introduction of new minerals. Relatively coarse grained (200 - 400µm) uraninite is hydrothermally broken down to coffinite and it is associated sulphide such as pyrite (FeS), galena (PbS), and chalcopyrite (CuFeS); and REE (Xenotime - YPO4) minerals along its grain boundaries and fracture planes, Fig. 4.31. Products of hydrothermal reaction in form of partial dissolution (Fig.4.32) and element re-mobilization have been deposited in fractures and are observed as veins, Fig. 4.36.

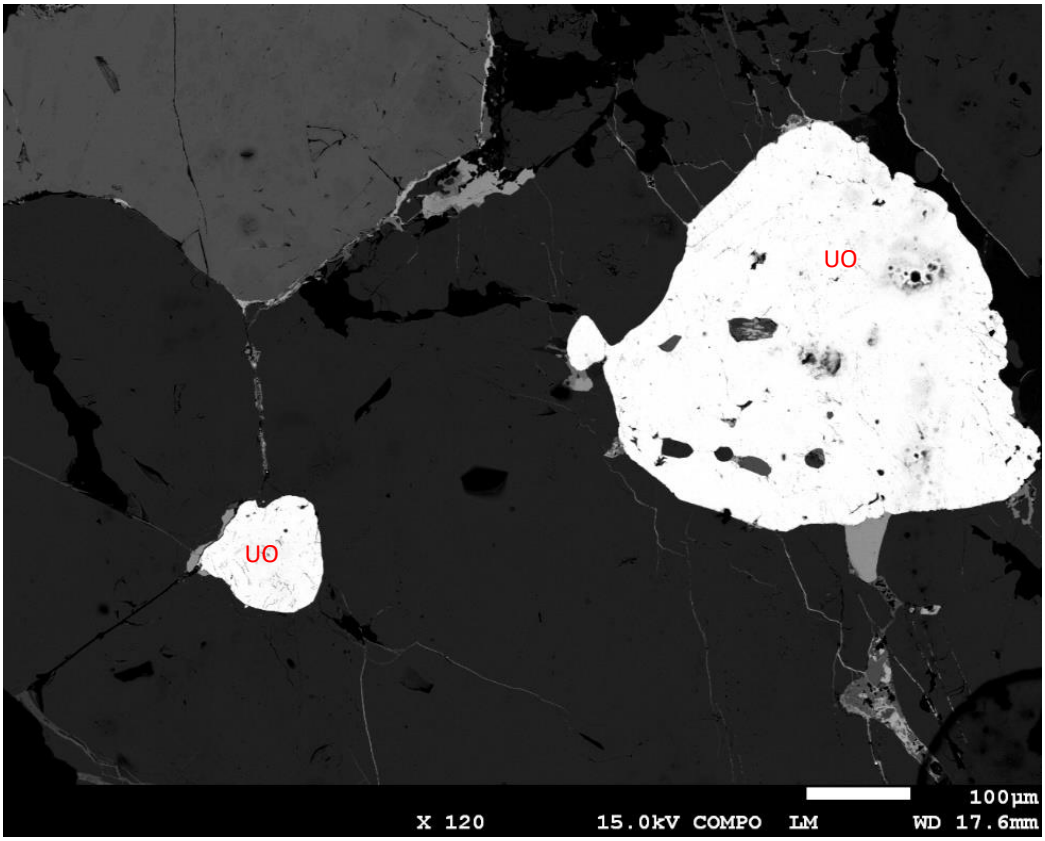

Figure 4.28. SEM photomicrograph of coarse-grained (200 - 400µm in size) uraninite, and micro-fractures as well as grain boundaries filled with hydrothermal mineralisation in iron skarn rock.

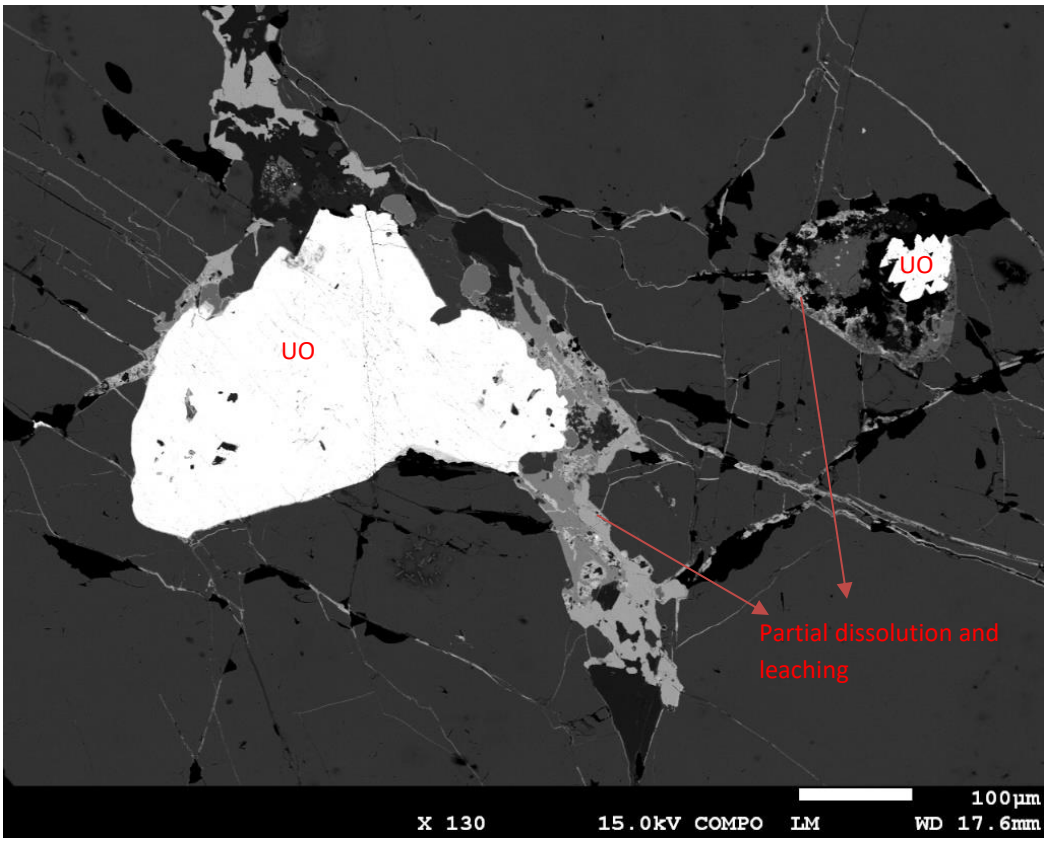

Figure 4.29. SEM photomicrograph showing partial dissolution and leaching of uraninite (UO) into fractures and as partial aureole around its grain (pale grey and grey).

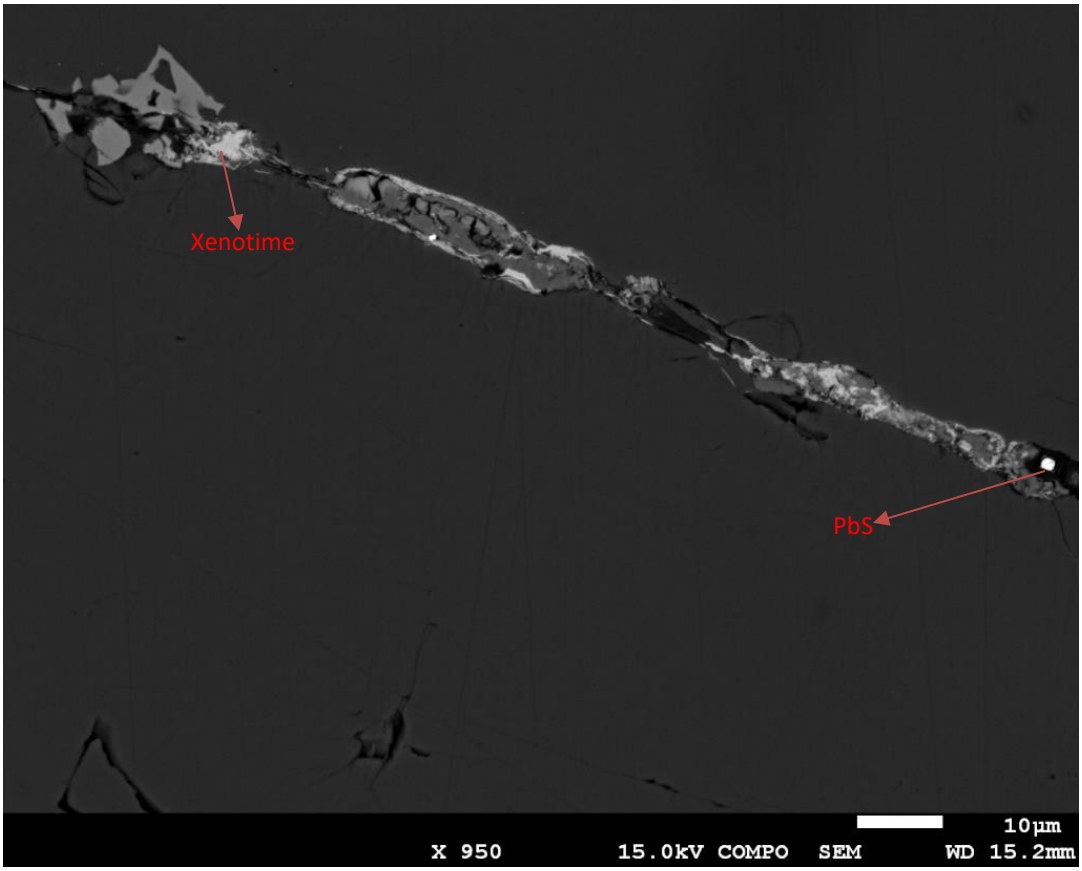

Figure 4.30. SEM Photomicrograph of a hydrothermal vein associated with hydrothermal uranium, REE (pale grey) and sulphide mineralisation. Bright white cubic galena (PbS) on the middle right margin of the plate.

Metamictization has been observed as alpha-decay halos around grains of uranium and suggest release of daughter products such lead that was ultimately mobilized by circulating hydrothermal fluids, Fig. 4.31 and Fig. 4.32. In-situ partial dissolution of fractured uraninite has been observed in close association with metamictized uraninite and coffinite infills (Fig. 4.32) indicating remobilization of uranyl ions and other elements such Lead and Yttrium.

Colloform texture of coffinite (USi), aragonite and opal has been observed associated with zircon in calc-silicate rock, Fig. 4.31.

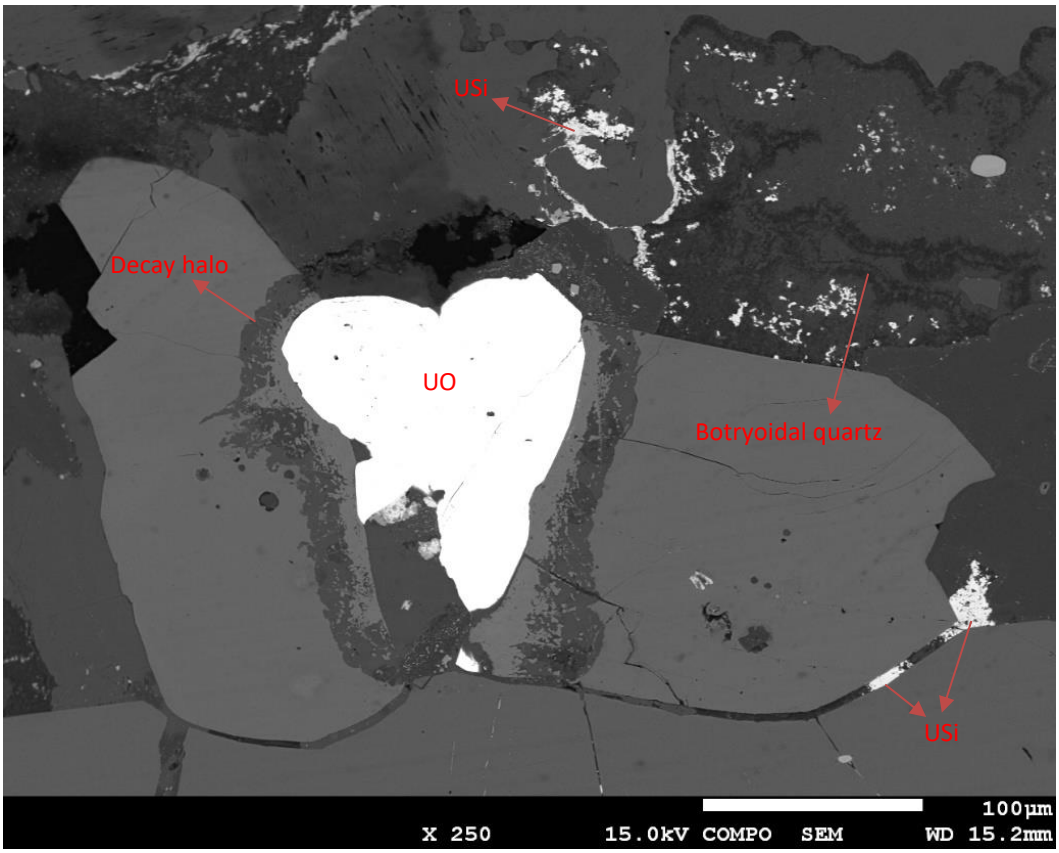

Figure 4.31. Metamictization of uraninite (UO) indicated by alpha-decay halo around its grain boundary. Botryoidal quartz and coffinite (USi) in the top middle right and fracture infilling of coffinite in the bottom right of the photomicrograph.

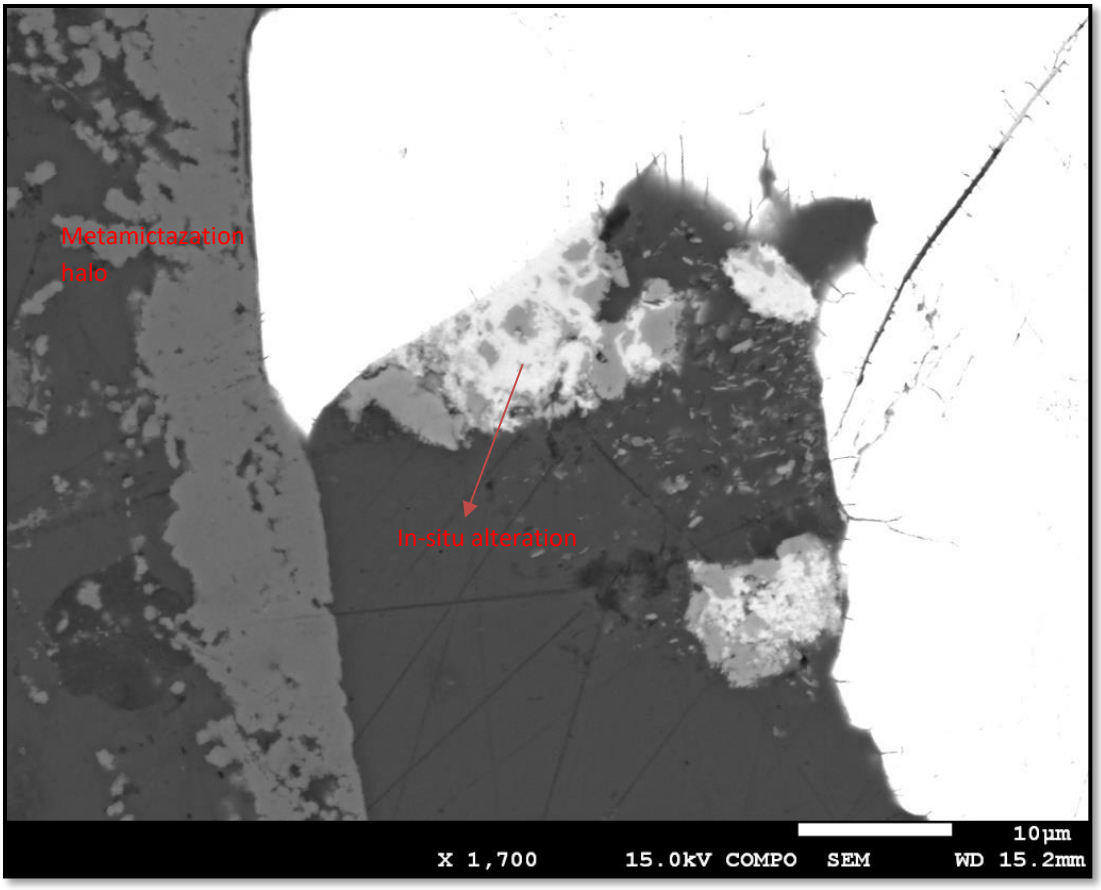

Figure 4.32. SEM photomicrograph of in-situ alteration (centre, pale grey and grey) of uraninite (white) and metamictization halo on the left of the photomicrograph.

Mineral growth zonation or corona texture has occasionally been observed on some uraninite grains, Fig. 4.33 and Fig. 4.34. At least two composition zones have been observed on a uraninite grain and may represent a sequence of hydrothermal mineral reactions that could be related to evolution of a hydrothermal fluid or surface nucleation of successive minerals related to multiple fluids. The mechanism of formation of these zones could be interesting to study mineral phase systems to test along boundary mineral growth or volume diffusion mineral growth. Idioblastic apatite has occasionally been observed enclosed in uraninite grains, Fig. 4.33.

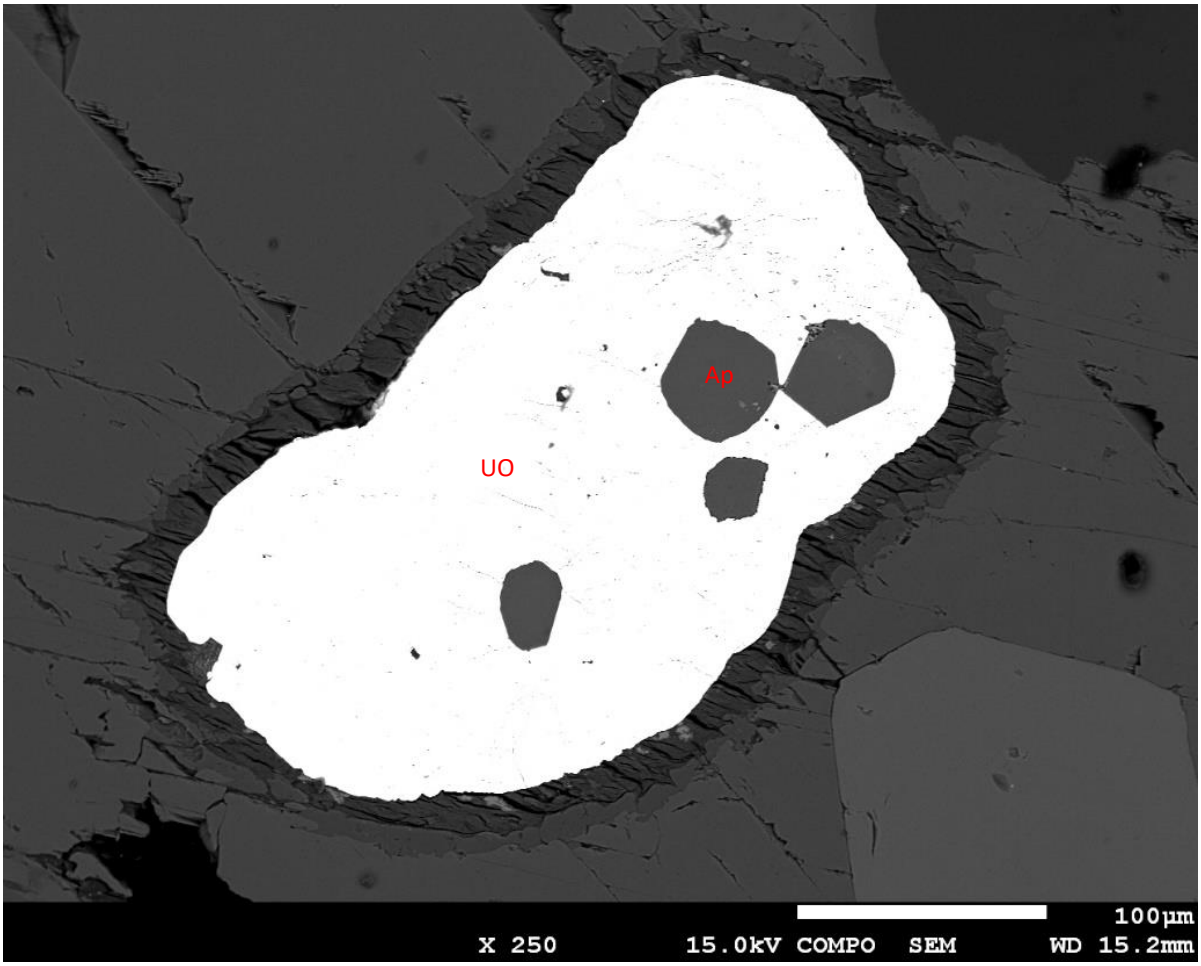

Figure 4.33. SEM photomicrograph depicting two compositional zones (corona texture) around uraninite grain and anhendral to subeuhedral apatite enclosed in uraninite.

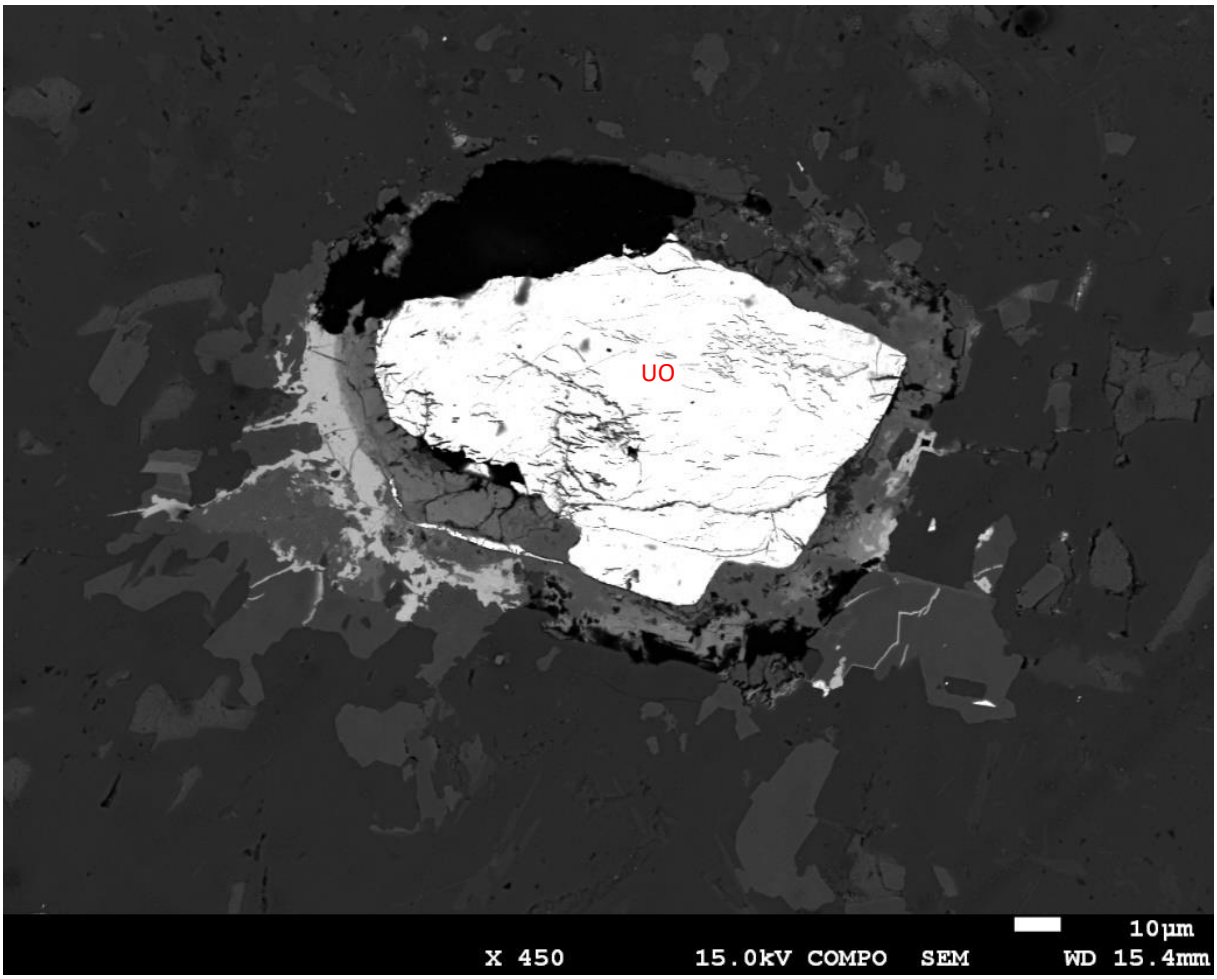

Figure 4.34. SEM photomicrograph showing pervasively fractured uraninite grain with composition zonation and replacement texture around its grain margins within a silicate groundmass.

In general the observed textures suggest temporal association of coffinite, REE and sulphide mineralisation in fractures and along grain margins of uraninite and host rock mineral assemblages, Fig. 4.35.

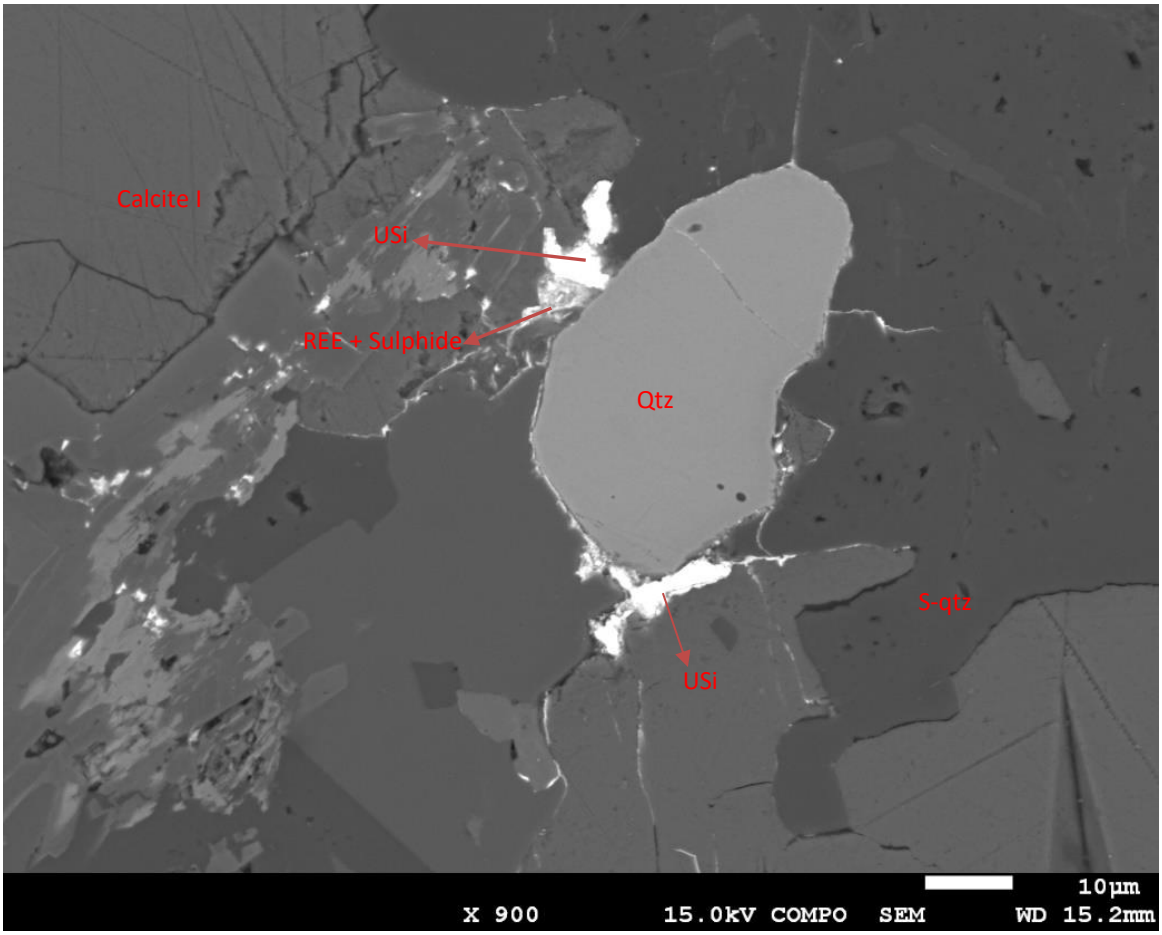

Figure 4.35. SEM photomicrograph of Sulphide, REE and coffinite (USi) mineralisation at the left top and bottom of a quartz grain (subrounded, pale-grey, Qtz), around grain boundaries, and in fractures. Calcite I – calcite of calc-silicate rock; S-Qtz – silicification quartz.

4.3 Geochemistry

Whole rock major and trace element analyses of metasedimentary, granitic, and skarn rock samples from three boreholes, INCRD 155, INCRD 277, and INCRD 332 are presented in Table 4.2 to Table 4.9. The analysed samples comprise calc-silicate gneisses, biotite gneisses, iron skarn rocks and undifferentiated granites. The heterogeneity in rock types and composition related to hydrothermal alteration as described in section 4.2, and therefore unusual composition as a

consequence of replacement textures and partial dissolution as well as leaching could have resulted to a wide range variability of elemental concentrations in each borehole and sample such as very low silica content in some samples. The geochemical data is therefore presented in relation to both main rock type association and vertical variations in each of the three boreholes.

Table 4.2. Major element oxides content (wt.%) of samples from boreholes INCRD 332, INCRD 155 and INCRD 277.

Sample no.	Lithology	Al_2O_3	CaO	Fe_2O_3	K_2O	Na_2O	SiO_2	TiO_2	MgO	MnO	P_2O_5
		Wt. %	Wt. %	Wt. %	Wt. %	Wt. %	Wt. %	Wt. %	Wt. %	Wt. %	Wt. %
INCRD332_1	Leucocratic granite	14.74	0.68	0.81	8.31	2.20	73.00	0.01	0.14	0.01	0.11
INCRD332_2	Leucocratic granite, scapolite, cavities	12.58	3.62	1.66	1.14	3.62	76.64	0.04	0.66	0.03	0.02
INCRD332_3	Calc-silicate, migmatitic biotite gneiss	14.69	6.51	6.03	1.69	3.80	61.45	0.85	4.71	0.10	0.17
INCRD332_4	Leucocraticgranite, weathered, oxidised	13.76	0.83	0.81	5.91	2.85	75.69	0.03	0.05	0.01	0.05
INCRD332_5	Leucocratic granite, Biotite gneiss	13.46	4.44	3.69	0.78	4.30	71.16	0.25	1.66	0.07	0.17
INCRD332_6	Calc-silicate gneiss, magnetite skarn, anhydrite	2.67	7.97	62.86	0.14	0.44	22.45	0.29	2.79	0.35	0.05
INCRD332_7	Calc-silicate gneiss, magnetite, pyroxene, anhydrite	6.94	17.22	17.73	0.25	1.43	50.66	0.12	5.19	0.39	0.07
INCRD332_8	Calc-silicate gneiss, magnetite skarn, anhydrite/gypsum	3.45	11.69	46.86	0.17	0.76	32.23	0.22	4.18	0.38	0.06
INCRD332_9	leuco granite + calc-silicate	14.02	11.08	10.43	1.00	3.14	52.29	0.80	6.92	0.17	0.15
INCRD332_10	Leucocratic granite	19.21	10.13	2.57	0.57	5.13	60.41	0.13	1.25	0.08	0.53
INCRD155_1	Granite	14.16	0.77	0.96	7.16	2.76	73.91	0.03	0.13	0.01	0.12
INCRD155_2	Massive magnetite, mm calcite veins, magnetite skarn, calc-silicate rock	1.68	1.94	83.70	0.24	0.20	9.02	0.48	2.03	0.17	0.55
INCRD155_3	Calc-silicate, cavities, calcite	2.91	2.84	74.32	0.26	0.42	16.31	0.35	2.33	0.18	0.08

INCRD155_4	Calc-silicate, magnetite skarn,	2.50	16.29	45.41	0.13	0.14	29.44	0.19	5.02	0.33	0.55
INCRD155_5	Biotite gneiss, migmatitic, veins calcite + quartz	14.67	8.92	5.74	1.76	3.26	56.04	0.85	8.50	0.08	0.19
INCRD155_6	Biotite gneiss, migmatitic, cavities with calcite	12.86	6.76	9.74	2.85	2.41	54.19	0.95	9.92	0.15	0.17
INCRD155_7	Granite, pegmatitic	17.25	1.49	1.22	9.22	3.47	66.19	0.08	0.41	0.02	0.65
INCRD155_8	Magnetite skarn	0.90	1.26	92.45	0.12	0.08	2.97	0.49	0.71	0.19	0.84
INCRD155_9	Magnetite skarn	3.14	4.46	72.79	0.34	0.56	13.62	0.37	2.20	0.19	2.33
INCRD155_10	Granite	14.25	9.10	5.71	0.89	3.52	58.16	0.78	7.30	0.10	0.18
INCRD155_11	Granite	13.69	3.02	11.94	2.75	3.19	58.86	0.67	5.47	0.09	0.32
INCRD155_12	Biotite gneiss, massive	15.55	1.70	3.81	8.23	3.27	65.15	0.27	1.28	0.04	0.70
INCRD155_13	Massive magnetite, some cavities	16.15	2.49	3.19	8.94	2.99	62.97	0.37	1.96	0.04	0.91
INCRD155_14	Granite	16.87	4.03	6.21	2.56	5.16	59.77	0.66	4.10	0.08	0.56
INCRD155_15	Massive magnetite, iron skarn, calc-silicate rock, calcite veins	1.90	0.34	86.58	0.80	0.10	7.56	0.32	1.95	0.25	0.19
INCRD155_16	Calc-silicate, magnetite, cavities, calcite	0.96	0.56	95.96	0.10	0.03	0.96	0.35	0.46	0.23	0.41
INCRD155_17	Granite, disseminated magnetite	13.42	3.31	4.32	0.75	4.22	72.93	0.23	0.64	0.04	0.14
INCRD277_1	Granite	12.90	1.77	0.82	6.24	3.07	75.04	-0.02	0.10	0.01	0.07
INCRD277_2	Granite	12.96	1.48	2.17	4.84	3.96	74.08	0.10	0.26	0.02	0.14

INCRD277_3	Granite	12.88	1.17	1.43	4.83	3.62	75.69	0.07	0.22	0.01	0.08
INCRD277_4	Granite	15.36	6.31	1.02	3.89	4.85	68.08	0.07	0.25	0.01	0.15
INCRD277_5	Biotite gneiss	15.44	2.79	6.57	3.67	4.11	60.79	1.07	5.33	0.07	0.16
INCRD277_6	Leucocratic granite	13.94	2.52	1.38	2.05	5.13	74.87	0.04	0.05	0.01	0.01
INCRD277_7	U mineralised Leucocratic granite	15.31	8.05	1.09	1.07	5.40	68.46	0.07	0.38	0.01	0.14
INCRD277_8	Biotite gneiss, migmatitic	14.74	3.68	7.20	3.83	3.83	59.88	1.02	5.54	0.09	0.19
INCRD277_9	Biotite gneiss, magnetite skarn	7.07	5.70	50.24	0.38	2.44	31.95	0.40	0.86	0.22	0.74
INCRD277_10	Pinkish Granite, phlogopite + calcite alteration	11.07	3.04	14.19	8.47	0.13	42.56	1.49	16.78	0.20	2.06
INCRD277_11	Leucocratic granite	14.07	1.50	1.05	4.69	4.32	73.94	0.07	0.27	0.01	0.07

4.3.1 Geochemistry of borehole INCRD 155

The concentration values of Fe_2O_3 and SiO_2 are the most anomalous of the major oxide elements of samples from borehole INCRD 155, and display a clear inverse concentration relationship between these two major oxides, Fig. 4.36. The concentration values of SiO_2 range from 58.16 to 73.91 wt % in granite samples, 57.17 to 60.75 wt % in biotite gneiss samples, and 9.97 to 27.81 wt % in iron skarn-calc-silicate gneiss samples. The elevated concentrations of Fe_2O_3 are most abundant in iron skarn rock samples ranging from 84.5 to 96.36 wt %, and iron skarn rich calc-silicate gneiss samples varying from 42.89 to 92.50 wt % concentration. The concentrations of Al_2O_3 range from 12.87 to 18.01 wt % in granite samples, 13.76 to 16.95 wt % in biotite gneiss samples. The remainder of major elements do not represent any significant anomalies and range from below detection of 0.01 ppm to 10 ppm wt %.

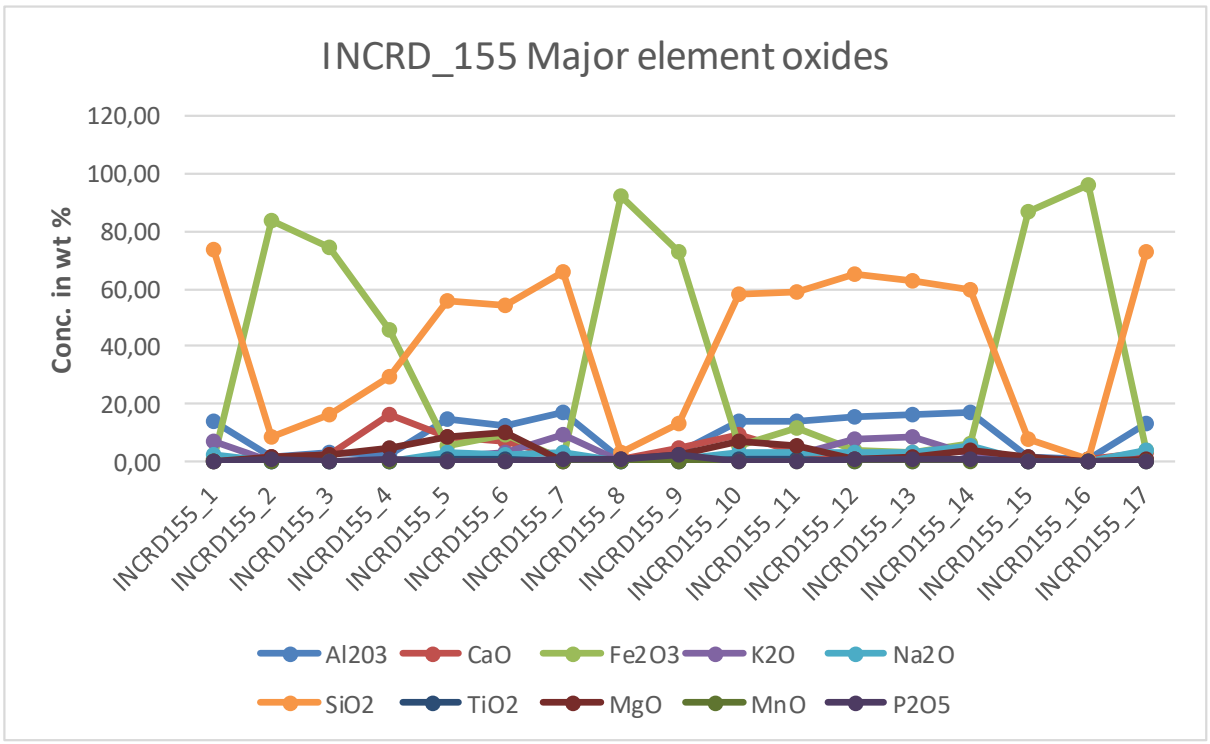

Figure 4.36. Major oxide element abundances of samples from borehole INCRD 155.

Selected lithophile trace elements concentration of Nb, Rb, Ta, Th, U, and Ba are shown in Table 4.3. Uranium has the highest and a wide range concentration of 4 to 13400 ppm in samples of coarse-grained pegmatitic granite and iron skarn respectively. Anomalous U concentrations of 116 ppm, 147 ppm and 1070 ppm are observed in calc-silicate gneisses of samples INCRD 155-3, -4 and -11 respectively and are associated with elevated Fe_2O_3 concentrations of 83.9 wt %, 42.9 wt % and 12.5 wt % respectively. Generally, biotite gnesiss samples do not show uranium enrichment.

Table 4.3. Lithophile trace element concentrations of samples from borehole INCRD 155.

Sample No.	**Lithology**	**Nb ppm**	**Rb ppm**	**Ta ppm**	**Th ppm**	**Ba ppm**	**U ppm**
INCRD155_1	Granite	<0.01	416	0.5	3	353	6.5
INCRD155_2	Massive magnetite, mm calcite veins, magnetite skarn, calc-silicate rock	<0.01	5	1.5	169	9	11000
INCRD155_3	Calc-silicate, cavities, calcite	<0.01	7	4	2	17	116
INCRD155_4	Calc-silicate, magnetite skarn	<0.01	<0.01	0.5	9	4	1070
INCRD155_5	Biotite gneiss, migmatitic, veins calcite + quartz	10	326	1.5	10.5	505	10
INCRD155_6	Biotite gneiss, migmatitic, cavities with calcite	70	517	4	4.5	91	20
INCRD155_7	Granite, pegmatitic	<0.01	531	1	2.5	433	4
INCRD155_8	Magnetite skarn	<0.01	1	1	79.5	<0.01	5180
INCRD155_9	Magnetite skarn	20	20	1.5	326	14	13400
INCRD155_10	Granite	15	67	1	10.5	194	20

INCRD155_11	Granite	80	426	6.5	11.5	106	147
INCRD155_12	Biotite gneiss, massive	15	434	1.5	3	413	20
INCRD155_13	Massive magnetite, some cavities	20	552	2.5	2.5	410	14.5
INCRD155_14	Granite	40	338	3	6.5	98	49.5
INCRD155_15	Massive magnetite, iron skarn, calc-silicate rock, calcite veins	25	95	3	3.5	19	399
INCRD155_16	Calc-silicate, magnetite, cavities, calcite	5	1	1.5	16	<0.01	2400
INCRD155_17	Granite, disseminated magnetite	25	72	5	63.5	105	16

Selected siderophile trace elements Ni, Co and Cr of samples from borehole INCRD 155 are generally of very low and wide distribution of concentration ranging from below detection limit to 110 ppm (sample INCRD 155-10). Concentration of selected siderophile trace elements Ni, Co, and Cr range from 10 ppm to 100 ppm, 1 ppm to 58 ppm, and 2 ppm to 110 ppm respectively in all samples.

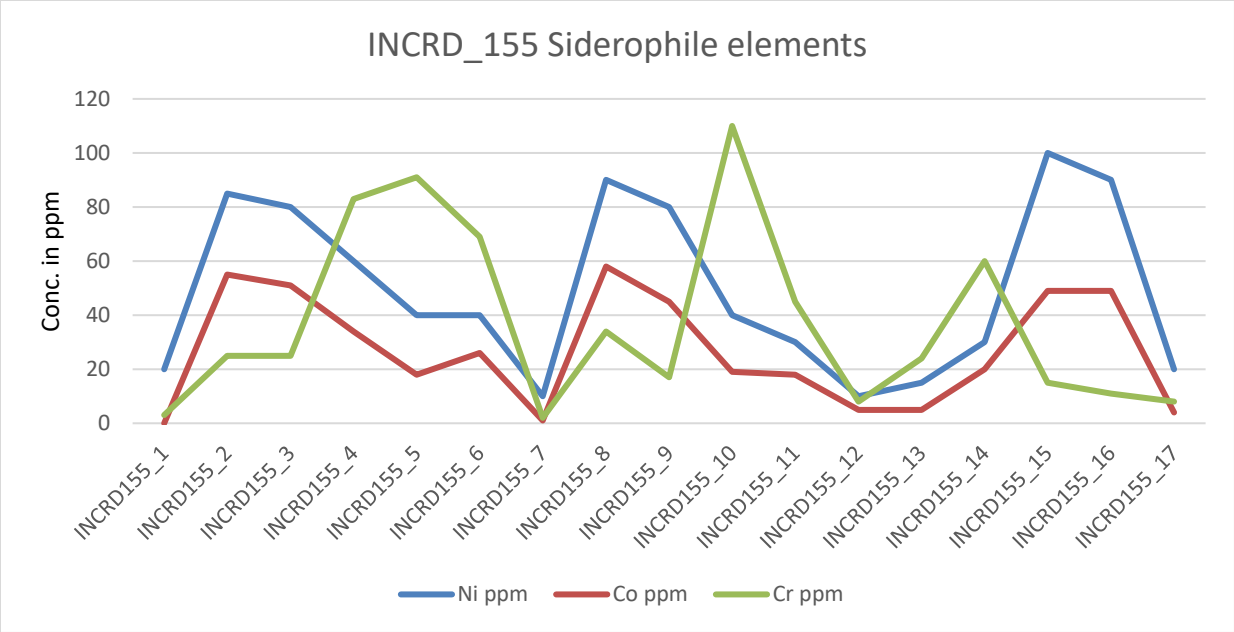

Figure 4.37. Siderophile trace element distribution of samples from borehole INCRD 155.

There is no obvious correlation between siderophile trace element concentrations and U enrichment in samples from borehole INCRD 155, Table 4.4. However, a relatively positive correlation between Ni concentrations and U enriched samples INCRD 155-2, INCRD 155-3, INCRD 155-4, INCRD 155-8, INCRD 155-9, INCRD 155-15 and INCRD 155-16, except of sample INCRD 155-11 that is also U enriched but have much lower Ni concentration of 30 ppm.

Table 4.4. Siderophile trace element and uranium concentrations of samples from borehole INCRD 155.

Sample no.	**Lithology**	**Ni ppm**	**Co ppm**	**Cr ppm**	**U ppm**
INCRD155_1	Granite	20	<0.01	3	**6.5**

INCRD155_2	Massive magnetite, mm calcite veins, magnetite skarn, calc-silicate rock	85	55	25	11000
INCRD155_3	Calc-silicate, cavities, calcite	80	51	25	116
INCRD155_4	Calc-silicate, magnetite skarn,	60	34	83	1070
INCRD155_5	Biotite gneiss, migmatitic, veins calcite + quartz	40	18	91	10
INCRD155_6	Biotite gneiss, migmatitic, cavities with calcite	40	26	69	20
INCRD155_7	Granite, pegmatitic	10	1	2	4
INCRD155_8	Magnetite skarn	90	58	34	5180
INCRD155_9	Magnetite skarn	80	45	17	13400
INCRD155_10	Granite	40	19	110	20
INCRD155_11	Granite	30	18	45	147
INCRD155_12	Biotite gneiss, massive	10	5	8	20
INCRD155_13	Massive magnetite, some cavities	15	5	24	14.5
INCRD155_14	Granite	30	20	60	49.5
INCRD155_15	Massive magnetite, iron skarn, calc-silicate rock, calcite veins	100	49	15	399
INCRD155_16	Calc-silicate, magnetite, cavities, calcite	90	49	11	2400
INCRD155_17	Granite, disseminated magnetite	20	4	8	16

The selected chalcophile elements, S, Pb, and Zn have shown significant concentrations in some samples, Table 4.2. Generally, sulphur concentrations vary from 50 ppm to 450 ppm across all samples except sample INCRD 155-14 which has anomalous concentration of 4350 ppm. The concentration of Pb varies from 4 ppm to 1140 ppm in sample INCRD 155- 6 and INCRD 155-9.

The elevated Pb values of 867 ppm, 397 ppm, 1140 ppm, and 174 ppm corresponds with U enriched samples INCRD 155-2, INCRD 155-8, INCRD 155-9 and INCRD 155-16. The concentrations of Zn in borehole INCRD 155 vary from 15 ppm to 195 ppm except in sample INCRD 155-1 that is below detectable level. All elevated concentrations of Zn directly corresponds to U enriched samples INCRD 155-2, INCRD 155-8, INCRD 155-9, INCRD 155-11, INCRD 155-15 and INCRD 155-16. In general, a positive correlation between U and chalcophile elements is observed. Elevated concentration of chalcophile elements corresponds to enriched uranium concentrations, Table 4.5.

Table 4.5. Chalcophile trace elements and U concentrations of samples from borehole INCRD 155

Sample No.	**Lithology**	**S (ppm)**	**Pb (ppm)**	**Zn (ppm)**	**U (ppm)**
INCRD155_1	Granite	150	21	<0.01	6.5
INCRD155_2	Massive magnetite, mm calcite veins, magnetite skarn, calc-silicate rock	150	867	100	11000
INCRD155_3	Calc-silicate, cavities, calcite	<0.01	16	90	116
INCRD155_4	Calc-silicate, magnetite skarn,	100	89	75	1070
INCRD155_5	Biotite gneiss, migmatitic, veins calcite + quartz	<0.01	6	15	10
INCRD155_6	Biotite gneiss, migmatitic, cavities with calcite	50	4	100	20

INCRD155_7	Granite, pegmatitic	<0.01	35	15	4
INCRD155_8	Magnetite skarn	450	397	145	5180
INCRD155_9	Magnetite skarn	150	1140	125	13400
INCRD155_10	Granite	50	11	30	20
INCRD155_11	Granite	100	16	110	147
INCRD155_12	Biotite gneiss, massive	50	31	30	20
INCRD155_13	Massive magnetite, some cavities	50	28	45	14.5
INCRD155_14	Granite	4350	12	60	49.5
INCRD155_15	Massive magnetite, iron skarn, calc-silicate rock, calcite veins	400	27	195	399
INCRD155_16	Calc-silicate, magnetite, cavities, calcite	<0.01	174	145	2400
INCRD155_17	Granite, disseminated magnetite	<0.01	12	20	16

Rare Earth Elements (REE) patterns of samples from borehole INCRD 155 indicate diverse signature among samples, Fig. 4.38. Some REE patterns are incomplete because of low concentration levels that are below analytical detection limits in some samples. The REE patterns of samples INCRD 155-2, -8, and -9 (Group 1) have a similar relatively flat to positive signature with a negative Eu anomaly, and display elevated heavy and light REE abundances compared to

the all other samples. These samples are U enriched and comprise predominantly of iron skarn rock. Two samples INCRD 155-4 and -16 (Group 2) have similar shallow positive signature with a negative Eu anomaly and are associated with elevated U and Fe concentrations. The samples INCRD 155-13 and -17 (Group 3) display a moderate negative pattern with a negative Eu anomaly and they are both granites and are associated with depleted concentrations of U and Fe. However, INCRD 155-13 appears to be enriched in light REE concentration and depleted in heavy REE compared to INCRD 155-17. The majority of samples INCRD 155-5, -6, -7, -10, -11, -12, -and -14 display a shallow negative pattern with a negative Eu anomaly. INCRD 155-1, -3, and -15 displays a relatively flat REE depleted pattern.

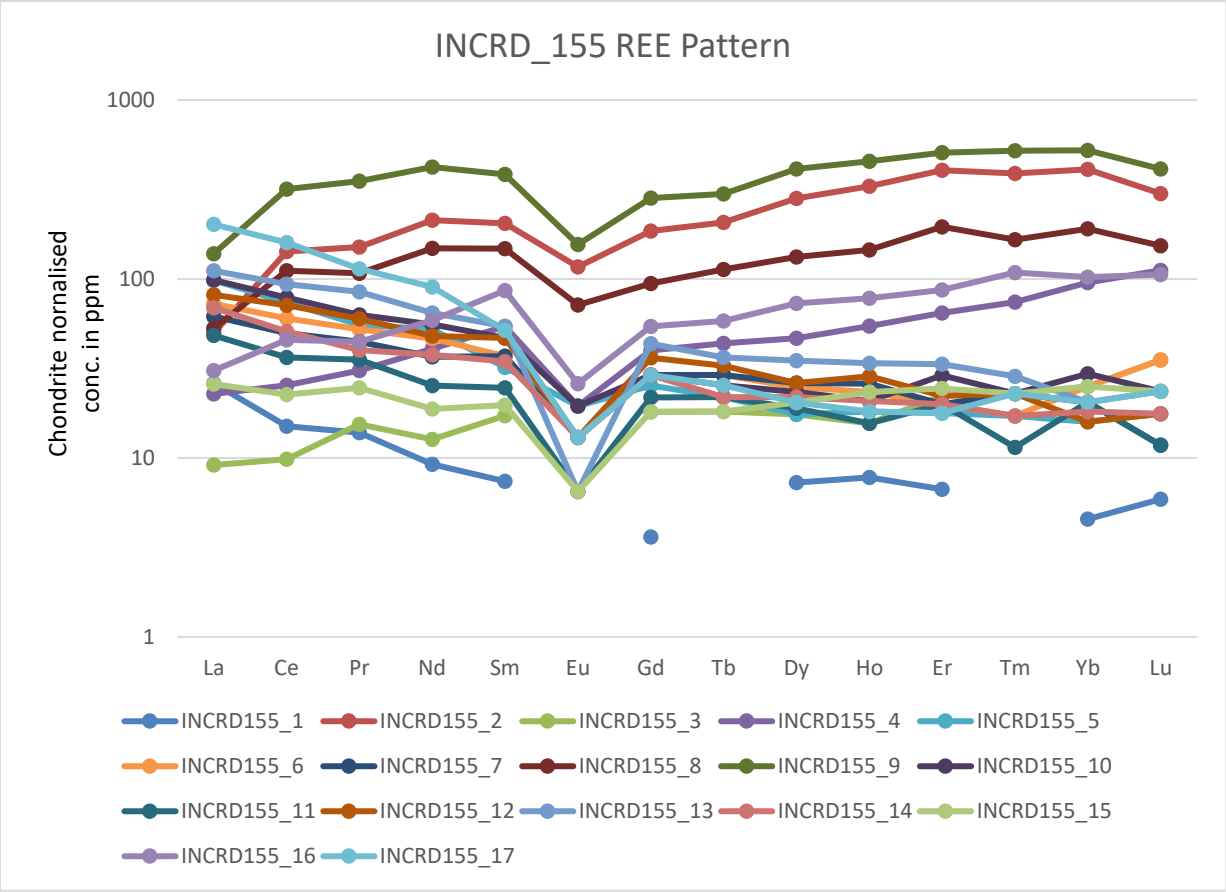

Figure 4.38. REE patterns of samples from borehole INCRD 155.

4.3.2 Geochemistry of borehole INCRD 277

The relative abundances of major oxide elements of samples from borehole INCRD 277 are shown in Figure 4.4. In all samples (granites), the concentration values of SiO_2 are the highest, except in biotite sample INCRD 277-9. Al_2O_3 has the second highest concentration values; and the remainder major oxide elements are relatively of low concentrations ranging from below detection (TiO_2 in sample INCRD 277-1) to relatively moderate concentrations, generally below 5 wt %, Fig. 4.4. However, sample INCRD 277-9 and -10 appear to signify distinct concentration values and both represent the lowest SiO_2 concentration values of 29.09 and 39.15 wt % respectively. Sample INCRD 277-9 shows elevated Fe_2O_3 and relatively depleted Al_2O_3 and SiO_2 as well as relatively moderate elevated CaO concentration of 5.19 wt %. Sample INCRD 277-10 (altered granite) shows elevated concentrations of MgO (15.44 wt %), Fe_2O_3 (13.05 wt %) and K_2O (7.79 wt %) as well as the highest concentration of P_2O_5 (1.90 wt %). Sample INCRD 277-9 and -10 correlates with U enrichment of 553 and 4420 ppm respectively.

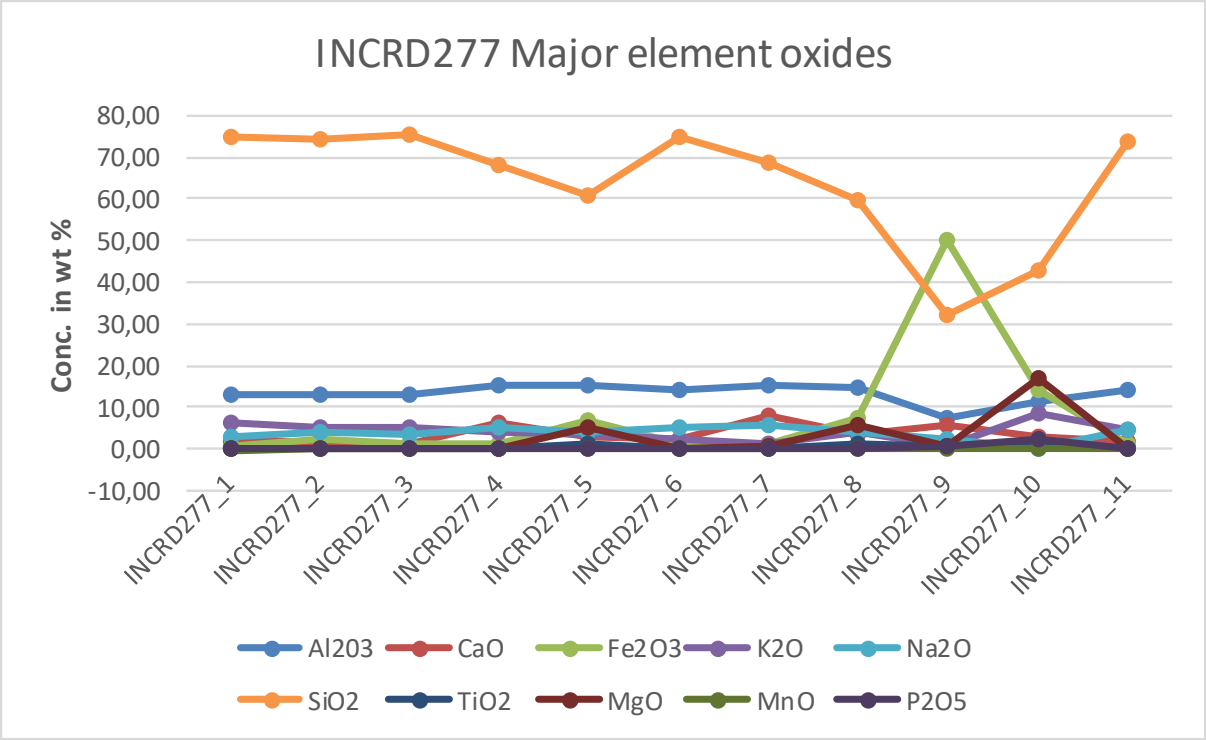

Figure 4.39. Relationship of major oxides in borehole INCRD 277.

The concentrations of selected lithophile trace elements Nb, Rb, Ta, Th, U and Ba of samples from borehole INCRD 277 are shown in Table 4.5. The most abundant selected lithophile trace elements in borehole INCRD 277 are Rb (13 to 1360 ppm), U (3 to 4420 ppm) and Ba (23 to 1310 ppm) and occur in all samples. Of the least abundant lithophile trace elements Nb, Ta, and Th in all the samples, except sample INCRD 277-10 which appears to be relatively anomalous and represent their highest values, Nb (95 pmm), Ta (7.5 ppm) and Th (70 ppm) in borehole INCRD 277, Th has the peak elevated concentration ranging from 1 to 9.5 ppm. Sample INCRD 277-10 signify a distinct relative elevated concentration of all selected lithophile trace elements, Table 4.5.

Table 4.6. Concentration of selected lithophile trace elements of samples from borehole INCRD 277.

Sample No.	Lithology	Nb ppm	Rb ppm	Ta ppm	Th ppm	Ba ppm	U ppm
INCRD277_1	Granite	<0.01	289	<0.01	1	452	11.5
INCRD277_2	Granite	<0.01	206	1	1.5	371	7.5
INCRD277_3	Granite	<0.01	224	<0.01	4	477	13
INCRD277_4	Granite	<0.01	155	<0.01	2.5	584	9.5
INCRD277_5	Biotite gneiss	15	467	2	9.5	1030	6
INCRD277_6	Leucocratic granite	10	82	1.5	6	421	16.5
INCRD277_7	U mineralised Leucocratic granite	<0.01	43	1	27	280	1340
INCRD277_8	Biotite gneiss, migmatitic	15	534	1.5	6.5	1310	3
INCRD277_9	Magnetite skarn, k-feldspar alteration)	<0.01	13	<0.01	8.5	23	553
INCRD277_10	Pinkish Granite altered, biotite + calcite alteration, phlogopite	95	1360	7.5	70	270	4420
INCRD277_11	Leucocratic granite	<0.01	192	<0.01	4.5	495	<0.01

The distribution of selected siderophile trace elements of samples from borehole INCRD 277 are shown in figure 4.5. The elevated concentrations of siderophile trace elements is observed as four distinct peaks representing samples INCRD 277-5, -8, -9 and -10 in figure 4.5. The remainder samples represent very low siderophile concentration levels ranging from below detection to 20 ppm. In the four distinct peaks, Cr has the highest concentration followed by Ni and Co respectively.

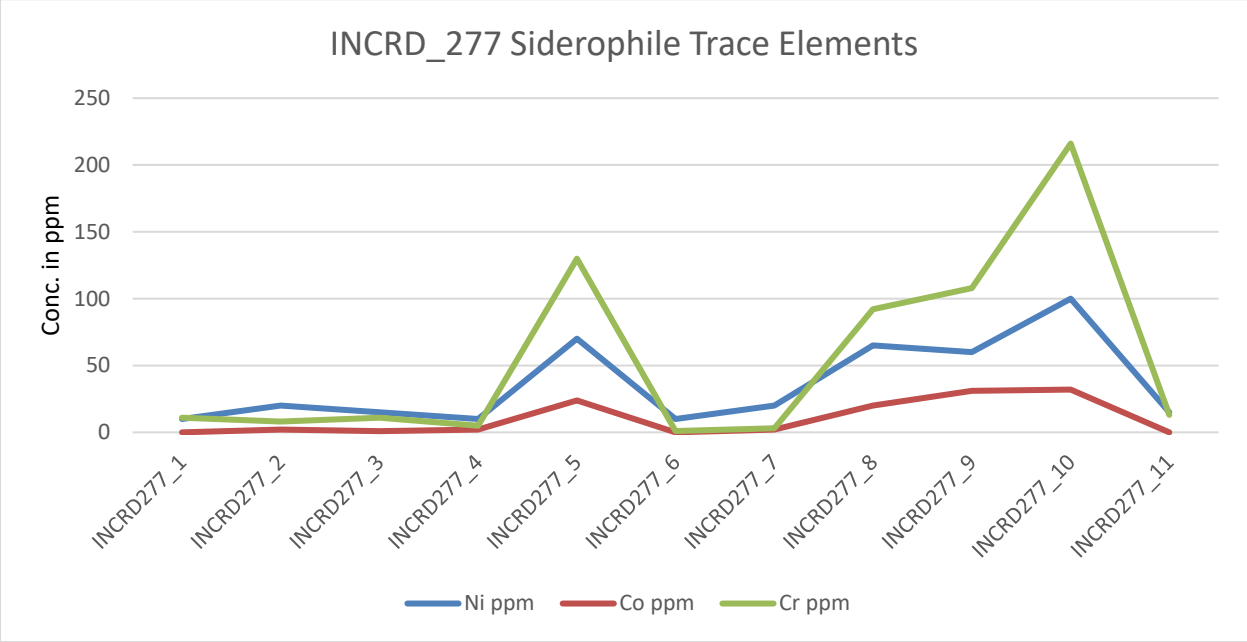

Figure 4.40. Distribution of selected siderophile trace elements of samples from borehole INCRD 277.

The concentrations of selected chalcophile trace elements of samples from borehole INCRD 227 are shown in Table 4.6. Sulphur is the most abundant chalcophile trace element in borehole 277 and is contained in all samples. The low range of sulphur concentrations (200, 600 and 700 ppm) is represented by granite sample INCRD 277-3, -6 and -11. The relatively broad high concentrations range from 1400 to 25200 ppm both limits occurring in granite sample INCRD

227-2 and -7 respectively. The relative elevated concentrations of Pb of 101 ppm and 292 ppm are observed in granite samples INCRD 277-7, and -10 respectively. The relatively anomalous concentrations of Zn, 105 and 205 ppm are observed in a biotite gneiss sample of INCRD 277-9 and granite sample of INCRD 277-10 respectively.

Table 4.7. Concentrations of chalcophile trace elements and U of samples from borehole INCRD 227.

Sample No.	**Lithology**	**S ppm**	**Pb ppm**	**Zn ppm**	**U ppm**
INCRD277_1	Granite	6200	16	<0.01	11.5
INCRD277_2	Granite	1400	13	<0.01	7.5
INCRD277_3	Granite	200	14	15	13
INCRD277_4	Granite	22900	14	<0.01	9.5
INCRD277_5	Biotite gneiss	1800	4	40	6
INCRD277_6	Leucocratic granite	600	11	55	16.5
INCRD277_7	U mineralised Leucocratic granite	25200	101	<0.01	1340
INCRD277_8	Biotite gneiss, migmatitic	4400	7	55	3
INCRD277_9	Biotite gneiss, k-feldspar alteration)	15000	40	105	553

INCRD277_10	Pinkish Granite, biotite + calcite alteration	2550	292	205	4420
INCRD277_11	Leucocratic granite	700	12	<0.01	<0.01

The REE patterns of samples from borehole INCRD 277 are plotted in figure 4.6 and display four distinct signatures. The relatively flat pattern is characterised by relatively moderate elevated light and heavy REE concentrations with a negative Eu anomaly and is represented by sample INCRD 277-10. A shallow negative pattern characterised by relatively low concentrations of REE is represented by samples INCRD 277-7 and –9. The samples INCRD 277-4, -5, and -8 displays a moderate negative REE pattern with a negative Eu anomaly. The very low incomplete REE pattern is represented by samples INCRD 277-2, -3, -6, and -11 and therefore are insignificant for REE

analysis.

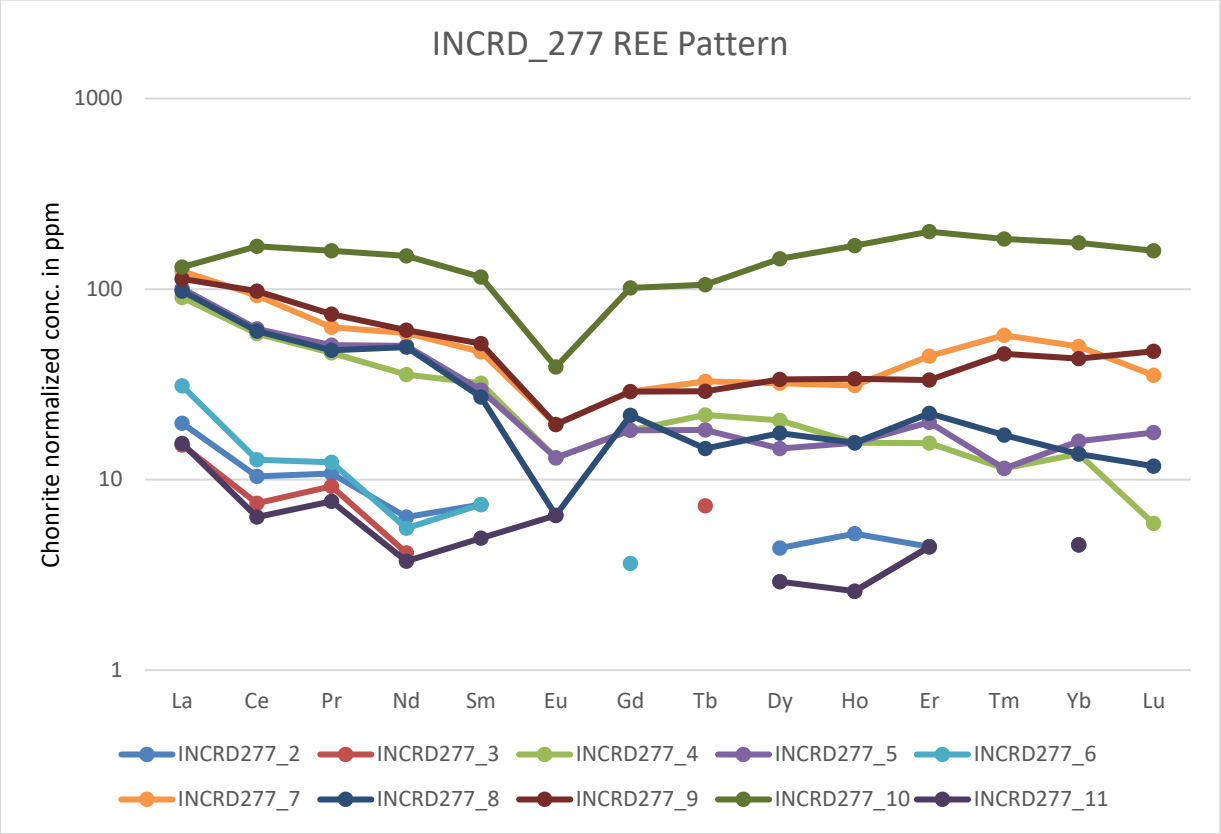

Figure 4.41. REE patterns of samples from borehole INCRD 277.

4.3.3 Geochemistry of borehole INCRD 332

The major element oxide distributions of samples from borehole INCRD 332 are plotted in Figure 4.7. In the exception of sample INCRD 332-6 and -8 where Fe_2O_3 is the most abundant, SiO_2 concentrations ranging from 59.04 to 91.34 wt % are by far the highest of the major oxide elements in all samples. The concentrations of Al_2O_3 indicate a relatively constant range from 14.81 to 20.41 wt % in samples INCRD 332-1, -2, -3, -4, -5, -9 and -10. CaO concentrations are relative elevated in samples INCRD 332-6, -7, -8, -9 and -10. Sample INCRD 332-1 represent the only relatively elevated concentration of the K_2O of 9.99 wt %.

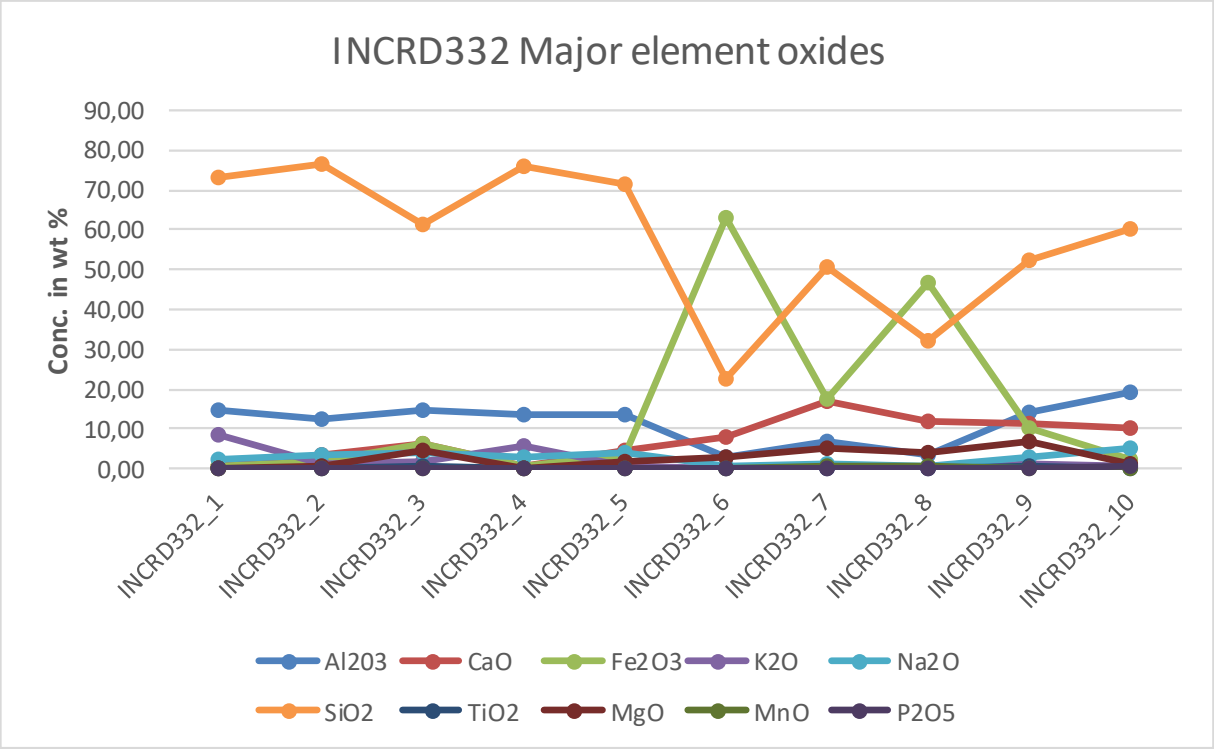

Figure 4.42 Major element oxide distributions of samples from borehole INCRD 332.

The concentration values of selected lithophile trace elements, Nb, Rb, Ta, Th, U and Ba of samples from borehole INCRD 332 are shown in Table 4.7. The lithophile trace element concentrations of all the samples are generally relatively low. However, relatively anomalous concentration levels for Rb, U and Ba. Samples INCRD 332-1, -3, and -4 represent elevated Rb concentrations of 415, 150, and 250 ppm in that order; and the anomalous U concentrations of 364, 76, 67.5 and 66.5 are observed in samples INCRD 332-2, -6, and -8 respectively; whereas elevated Ba concentrations of 1040, 102, 126 and 294 ppm are contained in samples INCRD 332-1, -2, -3, and -4 respectively.

Table 4.8. Concentrations of selected lithophile trace elements of samples from borehole INCRD 332.

Sample No.	Lithology	Nb ppm	Rb ppm	Ta ppm	Th ppm	Ba ppm	U ppm
INCRD332_1	Leucocratic granite	<0.01	415	1	1	1040	8
INCRD332_2	Leucocratic granite, scapolite, cavities	<0.01	37	1	11.5	102	364
INCRD332_3	Calc-silicate, migmatitic biotite gneiss	50	150	4.5	6.5	126	76
INCRD332_4	Leucocraticgranite, weathered, oxidised	<0.01	250	<0.01	0.5	294	1
INCRD332_5	Leucocratic granite, Biotite gneiss	10	13	2	3	48	4.5
INCRD332_6	Calc-silicate gneiss, magnetite, anhydrite	5	2	1.5	3.5	5	67.5
INCRD332_7	Calc-silicate gneiss, magnetite, pyroxene, anhydrite	<0.01	7	0.5	26.5	19	71
INCRD332_8	Mottled calc-silicate gneiss, magnetite, anhydrite/gypsum	<0.01	2	1	1	7	66.5
INCRD332_9	leuco granite + calc-silicate	40	20	3.5	7.5	75	8.5

INCRD332_10	Leucocratic granite, hydrothermally altered, fault	20	14	2.5	3.5	18	18.5

Concentration of selected chalcophile trace element S, Pb, and Zn are shown in Table 4.9. The levels of sulphur concentrations are elevated in samples INCRD 332-3, -6, -7, -8 and -10. Concentrations of Pb and Zn are generally very low in all the samples except for sample INCRD 332-6, -7, and -8 where slightly elevated concentrations of 125, 55 and 95 ppm are observed respectively.

Table 4.9. Concentrations of selected chalcophile trace elements and U of samples from borehole INCRD 332.

Sample No.	**Lithology**	**S ppm**	**Pb ppm**	**Zn ppm**	**U ppm**
INCRD332_1	Leucocratic granite	<0.01	16	25	8
INCRD332_2	Leucocratic granite, scapolite, cavities	50	32	5	364
INCRD332_3	Calc-silicate, migmatitic biotite gneiss	11900	11	40	76
INCRD332_4	Leucocraticgranite, weathered, oxidised	<0.01	14	<0.01	1
INCRD332_5	Leucocratic granite, Biotite gneiss	450	7	10	4.5
INCRD332_6	Calc-silicate gneiss, magnetite, anhydrite	2250	6	125	67.5

INCRD332_7	Calc-silicate gneiss, magnetite, pyroxene, anhydrite	15600	12	55	71
INCRD332_8	Mottled calc-silicate gneiss, magnetite, anhydrite/gypsum	4200	7	95	66.5
INCRD332_9	leuco granite + calc-silicate	300	11	35	8.5
INCRD332_10	Leucocratic granite, altered, fault	17500	6	10	18.5

The distribution of selected siderophile trace elements Ni, Co and Cr of samples from borehole INCRD 332 are shown in figure 4.7. The concentrations are generally low although relatively elevated Cr concentrations of 121 and 105 ppm are observed in samples INCRD 332-3 and -9 respectively.

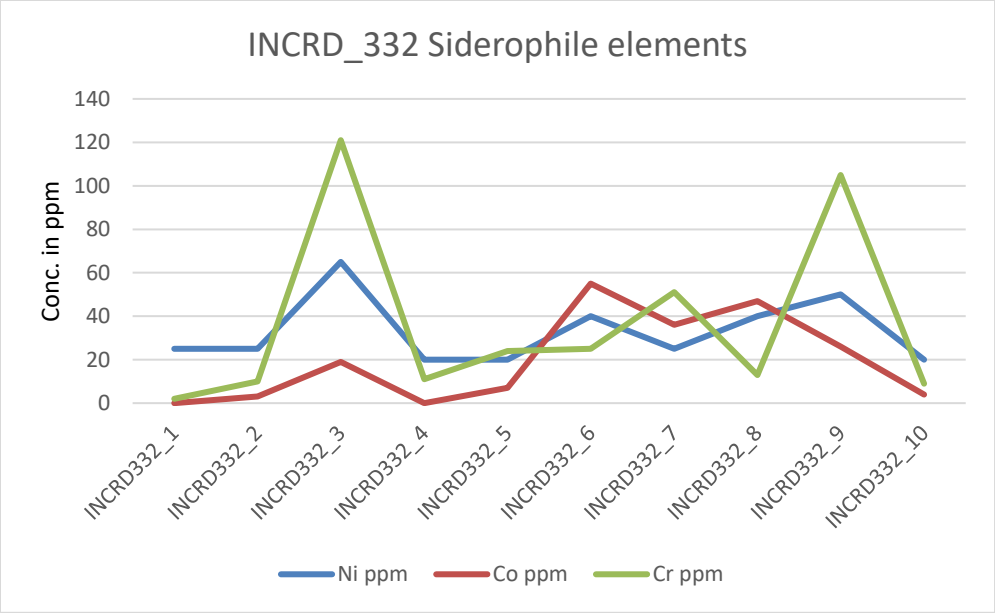

Figure 4.43. Distribution of selected siderophile trace elements of samples from borehole INCRD 332**.**

The REE patterns of samples from borehole INCRD 332 are plotted in figure 4.8. Most of the samples display a relatively flat heavy REE distribution and a variable light REE pattern. Based on the distribution of light REE and Eu signature, four REE distribution signatures have been distinguished, Fig. 4.8. A steep negative pattern with a gentle negative Eu is represented by samples INCRD 332-7 and -6 with highest and second highest concentrations of light REEs. The second pattern is represented by an overall moderate negative REE pattern with a gentle negative Eu and is indicated by samples INCRD 332-3 and -9. The third pattern of a relatively flat signature and a sharp negative Eu anomaly is represented by samples INCRD 332-5, -8, and -10. The fourth pattern has a relatively flat slope with a pronounced positive Eu anomaly and is manifested by sample INCRD 332-2.

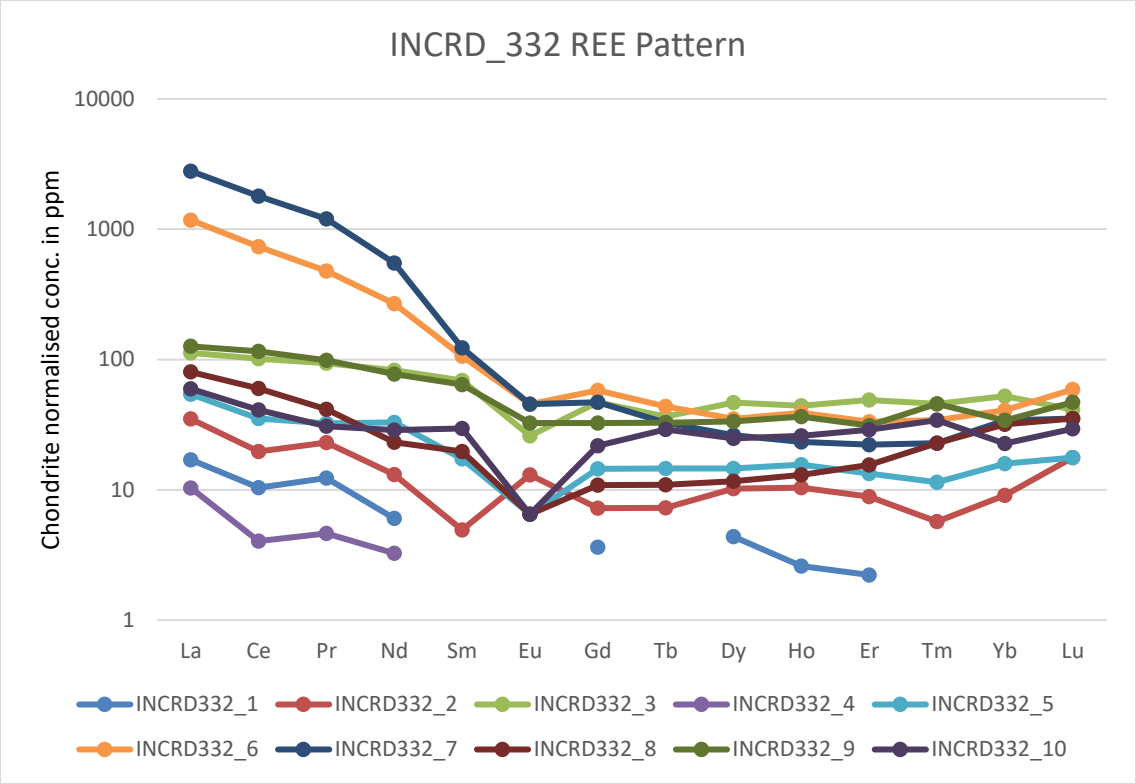

Figure 4.44. REE patterns of samples from borehole INCRD 332.

Chapter 5

5. Discussion

This chapter presents the main mineralogical and geochemical processes, which resulted in the formation of the Inca uranium deposit.

5.1 Primary genesis of uranium mineralisation

The prograde metamorphism of the Damara orogeny that resulted in amphibolite facies grade, is manifested by granoblastic recrystallization texture of the calc-silicate mineral assemblages encountered in this study, and has been ascribed to anatexis related genesis of primary uranium mineralisation, in particular, as the source of the uraniferous granites (Smith, 1965; Jacob et al., 1986). The amphibolite facies grade metamorphism is evident in the calc-silicate rock by massive to semi-massive interlocking mineral growth of pyroxene, calcite, and quartz as well as plagioclase feldspar to a lesser extent, and provide an indication of primary uranium generation as depicted by cob-web uraninite occurring in association with meatsedimentary quartz grain, Fig. 4.2 to Fig. 4.4. The occurrence of disseminated, interstitial and interlocked subeuhendral uraninite grains with euhedral-subeuhedral magnetite grains suggest a synmetarmophic and/or magmatic origin of primary uranium mineralisation, Fig. 4.21. The occasionally observed somewhat idioblastic crystal growth of apatite in disseminated uraninite grains in calc-silicate rock and iron skarn rock might also suggest synmetarmophic genesis, Fig 4.41. Furthermore, the occurrence of disseminated uraninite in leucogranites is a clear indication of magmatic origin of the primary uranium mineralisation.

5.2 Secondary hydrothermal uranium mineralisation

Retrograde metamorphism in the study area is associated with diverse mineral assemblages that reflect interaction of metamorphic and/or magmatic fluids with host prograde metamorphism mineral assemblages (section 4.1). Idiomorphic growth of hornblende (amphibole) in the cleavage planes of pyroxene suggest retrograde replacement texture because of hydration reactions, Fig 4.5. Metamictization and partial dissolution as well as leaching of uraninite grains through microfractures must have played a role in partial release of some elements like lead (Pb) from its internal structural sites, Fig. 4.40. Partial dissolution of plagioclase to produce sericite is a direct consequence of hydrothermal reaction, Fig. 4.17. Therefore, a prevalent hydrothermal system must have overprinted magmatic event associated with uranium mineralisation as postulated by Kinnaird and Nex (2007).

The pervasive silicification occurs as fracture and vug infills including as botryoidal or corona features of opal, arongonite and coffinite, Fig 4.31 and Fig. 4.33 - Fig. 4.35. The silicification processes is associated with precipitation of coffinite and sulphide mineralisation. The partial dissolution of some uraninite grains along grain boundaries and fracture suggest hydrothermal reaction and leaching as a mechanism for mobilizing uranium ions (U^{6+}) in form of uranyl ions, $(UO_2)^{2+}$ into solution where it exist as anion complexes (Plášil, 2014) and then precipitate as uranium silicate, coffinite. Therefore, coffinite, $USiO_4$, in 4^+ valance, is an alteration mineral of uraninite and forms from silica-rich ($>10^{-4}$ Mol/L, (Guo et al., 2015)), low temperature hydrothermal fluids containing dissolved uranium species under reducing conditions (Guo et al., 2015). Langmuir (1978) postulated the aqueous equilibrium of uraninite and coffinite at the concentration levels of 10-3 Mol/L, as follows:

$$USiO_4\,(s) + 2H_2O\,(l) \rightleftarrows UO_2\,(s) + Si\,(OH)_4\,(aq) \qquad (1)$$

Although the above is the most plausible mechanism to form coffinite and uraninite, coffinite may also form from processes that involve a sequence of reactions such as the dissolution of UO_2 under locally oxidizing environments, and then transport of the dissolved U^{6+} ions into more reducing environments containing dissolved silica, and finally the precipitation of coffinite, (Guo et al., 2015).

The hydrothermal reaction product coffinite is associated with REE (Y_2O_3 in particular) and sulphide mineralisation (galena), Fig 4.30 and Fig. 4.35. Although not directly observed, dissolution (inferred from common association with uraninite) of the observed idioblastic apatite might be the possible mechanism for the hydrothermal production of yttrium phosphate mineral, Xenotime.

The occurrence of gypsum and anhydrite in both the calc-silicate and granite rocks suggest interaction of host mineral assemblages with hydrothermal fluids of meteoric origin (Table 4.1). This observation therefore suggest and assumes mineral precipitation under conditions similar to current hydrological system and that these minerals formed at low temperatures and pressure (e.g., Ballouard et al., 2017; Bruneton and Cuney, 2016). The evidence of prevalent vugs and fracture infilling as well as colloform or botryoidal textures (Fig. 4.27 and Fig. 4.31) correlates well with these inferences.

5.3 Magnetite skarn

Anomalous concentrations of iron oxide in some samples correspond to hydrothermal replacement reaction of prograde metamorphic mineral phases, predominantly in calc-silicate gneiss and to a lesser extend biotite gneiss, Fig. 4.5, Fig. 4.6, and Fig. 4.10. This phenomenon suggest iron-rich magmatic-hydrothermal fluid interacting with mineral assemblages of the host calc-silicate gneiss.

However, apart from replacement textures such as magnetite enclosing texture and xenoblastic magnetite growth along cleavage planes (Fig. 4.11), no in-situ reaction products have been observed, except for hydrothermal quartz, which varies in amounts from almost completely absent in massive magnetite skarn to minor occurrences on the fringes of magnetite grains in semi-massive magnetite skarn.

Magnetite as a product of a chemical reaction process can be explained using two mechanisms. The first method is based on the Schikorr reaction, whereby the formation is assumed to be under anaerobic conditions from ferrous hydroxide ($Fe(OH)_2$), which is not stable and can be easily oxidised by water to produce magnetite (Fe_3O_4), hydrogen (H_2) and water (H_2O), (Schikorr, 1933).

The second mechanism of magnetite (Fe_3O_4) production based on the Massart reaction where formation of solid magnetite (Fe_3O_4) from $FeCl_2$ and $FeCl_3$ under sodium hydroxide (NaOH) conditions, (Massart, 1981). These two methods are conventional redox related reactions and similar in processes to the typical reduction reaction of hematite (Fe_2O_3) with hydrogen (H_2) to produce magnetite (Fe_3O_4). Non-redox reactions can also explain chemical changes in the production of magnetite from hematite and vice versa. The serpentinization of fayalite to magnetite can demonstrate the production of magnetite from hydrothermal reactions as below (Iyer, 2007):

$$Fe_2SiO_4 + H_2O = Fe_3O_4 + SiO_2 + H_2 \quad (2)$$

Therefore, similar reaction processes are suggested for mineral assemblages of calc-silicate rocks such as pyroxenes although this may be complicated due to their complex mineralogy (Iyer, 2007).

Subsequent to magnetite skarn formation, the observed pervasive fractures must have played an important role in magmatic-hydrothermal mobilization and remobilization of uranium and other associated elements and served as sites for mineral precipitation upon favourable conditions such

as redox boundary. This is evidenced by coffinite principally confined to fracture zones and margins of magnetite grains in association with sulphides such as lead (PbS), pyrite (FeS) and REE mineralisation (e.g. Xenotime), (Fig. 4.30 and Fig. 4.35). Multiple hydrothermal events and/or prolonged remobilization resulted in two mineral phases in equilibrium as zones around uraninite (Fig. 4.33 and Fig. 4.34).

5.4 Mineral paragenesis

The mineral paragenesis of the Inca deposit is determined based on textural characteristics and relationships of minerals and mineral assemblages observed in all studied samples from the three boreholes, e.g., Chapter 4, sections 4.1 and 4.2. These observations suggests that the gangue and ore mineral paragenesis at the Inca deposit is directly and indirectly related to prograde and retrograde metamorphism and the rock-fluid interaction of their related hydrothermal fluids as well as magmatic-hydrothermal and meteoric hydrothermal fluids. Consequent to amphibolite facies metamorphic overprint of the sedimentary rock pile, the mineral paragenetic sequence begins from prograde related recrystallization through peak metamorphism fluid influx (e.g. mobilization of calcite (calcite I) from calc-silicate rocks into fracture openings as veins (calcite II)) to syn- and late magmatic hydrothermal fluid interactions (Fig. 4.17) and late meteoric hydrothermal circulations, Table 5.1.

Table 5.1. A summary of observed mineral paragenetic sequence in the studied samples from borehole INCRD 155, INCRD 277 and INCRD 332.

Minerals	Stage I - Prograde metamorphism/ recrystallization	Stage II - Metamorphic/magmatic hydrothermal	Stage III - Meteoric hydrothermal/fluid
Uraninite			
Coffinite			
Xenotime			
Magnetite			
Hematite			
Sulphides			
Sulphates			
Quartz I			
Quartz II			
Calcite I			
Calcite II			
Pyroxene			
Hornblende			
Plagioclase			
Biotite I			
Biotite II			
Scapolite			
Diopside			

5.5 Geochemical processes, anomalies and trends

Anomalous content of some major element oxides, REE (plus Y), siderophile and chalcophile trace elements in relation to uranium enrichment and the host lithologies present insightful discussion points on the character of uranium mineralisation at Inca. The observed geochemical anomalies and trends reflect changes in the chemical composition mainly related to multiple magmatic and associated hydrothermal episodes as described in chapter 4. These geochemical processes are responsible, in parts, for successive uranium enrichment in the metamorphic rock pile of the lower Swakop Group of the Damara Supergroup at Inca uranium deposit.

Major element oxide abundances are characterised by anomalous silica and iron oxides such as Fe_2O_3 (42.89 to 92.50 wt % in iron skarn rock samples of drill hole INCRD 155) and SiO_2 (9.97 to 27.81 wt % in iron skarn-calc-silicate gneiss samples of drill hole INCRD 155) and are suggested to be related to metamorphic and/or magmatic related hydrothermal alterations as manifested by leaching and replacement textures under sections 4.1 and 4.2.

The anomalously low concentrations of SiO_2 in some samples is a consequence of replacement of silicate mineral assemblages by magnetite. These anomalous concentrations are in most cases directly associated with uranium enrichment e.g., Fig. 5.1 and Fig. 5.2. This association could imply that uranium has been sourced and transported by hydrothermal fluids of metamorphic and/or magmatic origin because the anoumalies are a result of hydrothermal activities. However, the spatial association could also be attributed to the reducing conditions of the host hydrothermal product, the magnetite skarn which rather triggered precipitation of uranium from subsequent circulating fluids, (e.g., Ballouard et al., 2017). This assertion is further supported by the occurrence of uranium in interstitial sites within massive granoblastic magnetite and calc-silicate host rocks, Fig. 4.28.

Trace element abundances of some elements depict correlation with uranium mineralisation and is postulated to imply simultaneous successive distinct processes e.g. metamorphic hydrothermal processes, magmatic hydrothermal and meteoric hydrothermal influence. Chalcophile trace elements S, Pb, and Zn have shown positive correlation with uranium enrichment (Fig. 5.3-5.5) especially in iron skarn rock and this may suggest a common temporal relationship for their occurrence. Furthermore, sulphur seems to be abundant in calc-silicate samples and appears to correspond to occurrence of gypsum and anhydrite (Table 4.1), and is interpreted to originate from late stage authigenic processes related to meteoric fluids, (e.g., Ballouard et al., 2017).

Evidence of REE and uranium enrichment correlation particularly associated with iron skarn rocks suggests mobility of REE during hydrothermal uranium mineralisation event, Fig. 4.3. An example is the association of coffinite and xenotime (yttrium phosphorous apatite), Fig. 5.1 and 5.2.

The observed weak correlation of Pb and U in borehole INCRD 332 (Fig. 5.3) is postulated to represent a different processes, possibly superimposed process altogether, and therefore cannot form a basis for correlation.

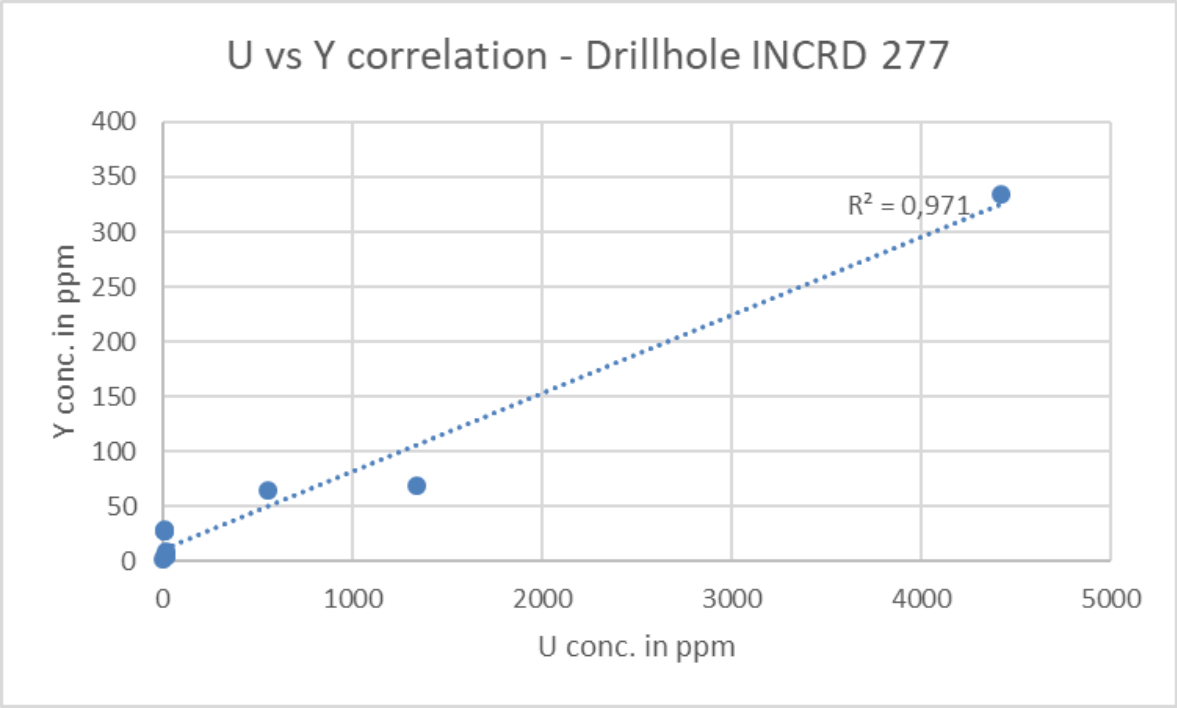

Figure 5.1. Correlation coefficient (R^2) of U verses Y (Yttrium) concentration in drill hole INCRD 277.

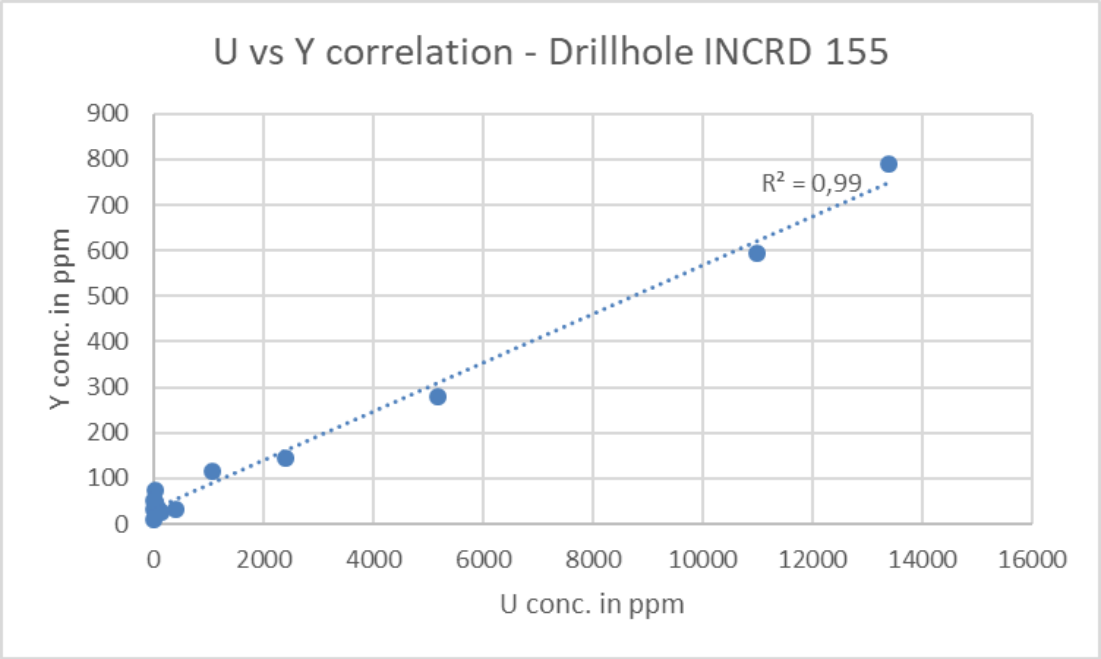

Figure 5.2. Correlation coefficient (R^2) of U and Y concentration in drill hole INCRD 155.

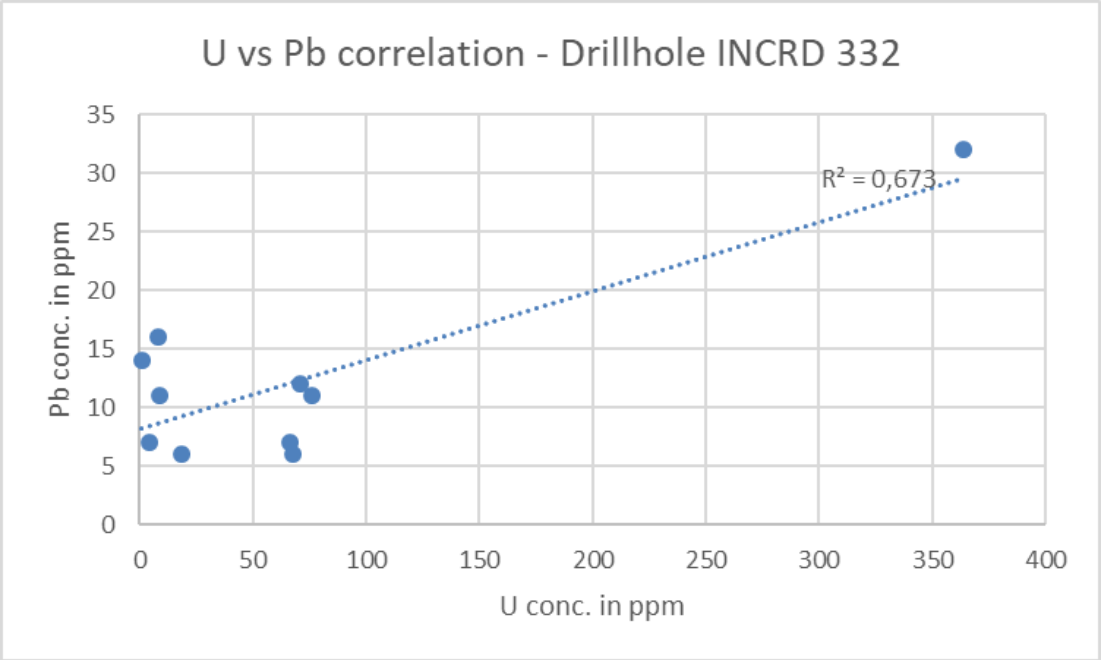

Figure 5.3. Correlation coefficient (R^2) of U verses Pb concentration in drillhole INCRD 332

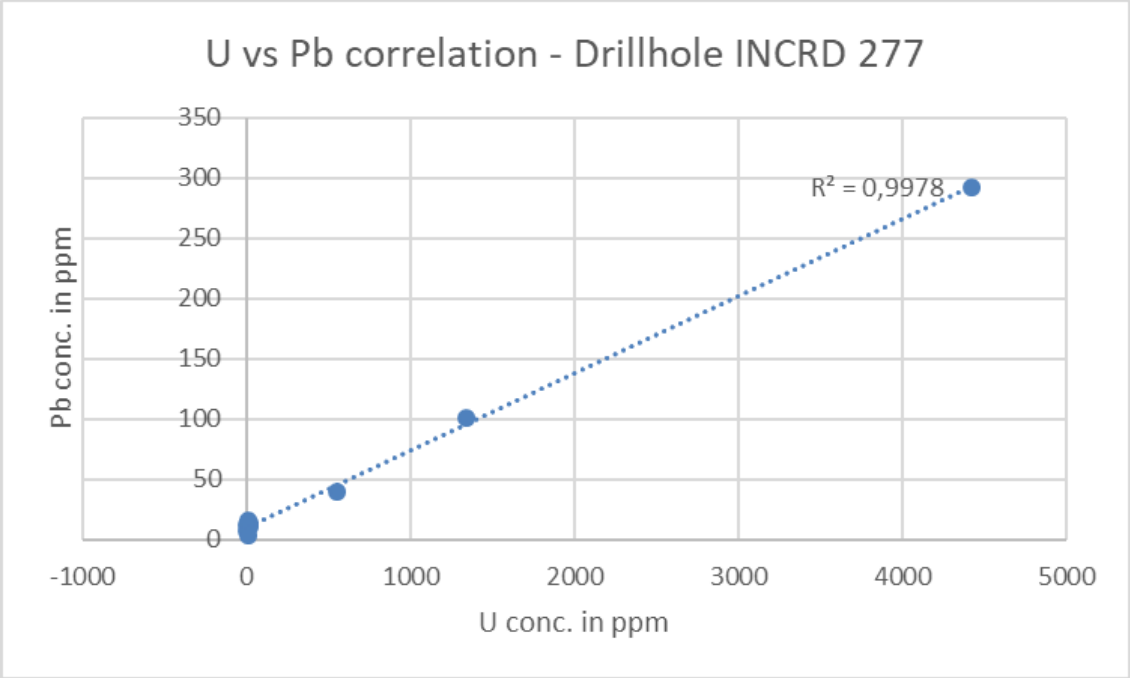

Figure 5.4. Correlation coefficient (R^2) of U verses Pb concentration in drill hole INCRD 277.

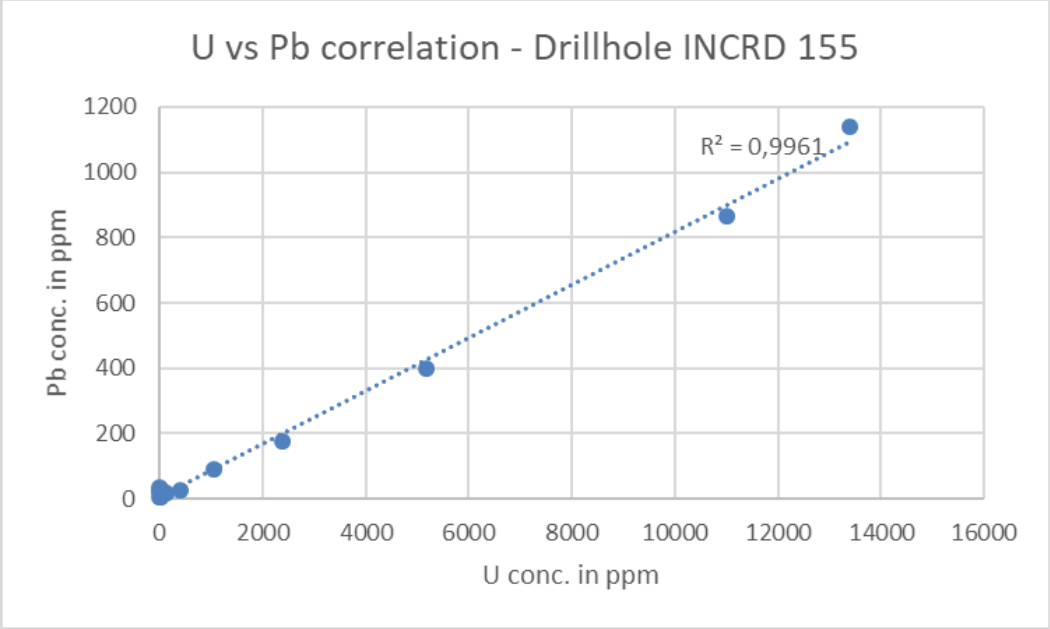

Figure 5.5. Correlation coefficient (R^2) of U verses Pb concentration in drill hole INCRD 155.

5.6 Mineralisation Model

Due to the scope of work, it has not been possible to precisely constrain the source of uranium mineralisation from this study. However, it has been established that the source of U mineralisation in this region, the Central Zone of the Damara belt, are the pre-Damara rocks and Damara sedimentary rocks with relatively anomalous uranium content that underwent metamorphism of upper amphibolite facies grade and partial melting to form uranium-enriched magma emplaced as leucogranites (Jacob et al., 1986; Nex et al., 2001a).

Evidence from thin section optical petrography and SEM studies suggest that uranium mineralisation in the Inca deposit is associated with magmatic and hydrothermal processes. A similar ore formation process model by Ballouard et al., (2017) is proposed by this study. The uranium mineralisation hosted in leucogranites and Damara metamorphic rocks occurs as disseminated uraninite, and coffinite in micro-fracture infills (veins). Magmatic fluids released from uranium-enriched leucogranites interacted with host metasedimentary rocks to form uranium enriched magnetite skarns. Multiple interaction because of successive infiltration of magmatic solutions led to further enrichment through remobilisation of uraninite to form coffinite.

Therefore, the origin of uranium mineralisation in the Inca U deposit begins with the intrusion of uraniferous leucogranites into metamorphosed Damaran metasedimentary rocks. The mineral assemblages such as pyroxenes and amphiboles (hornblende) of the metasedimentary rock, mainly calc-silicate, have been replaced by hydrothermal magnetite to form massive to semi-massive magnetite skarn rock (iron skarn) or hybrid rock of magnetite-enriched calc-silicate. The magnetite skarn rock is then invaded by fluids enriched in uranium leading to deposition of uraninite in interstitial sites and around grain boundaries, thereby interlocked with magnetite. The iron skarn rock must have created a redox condition that triggered deposition of uranium in interstitial or

fracture sites. The postulated fluid-rock interaction process is similar to what Cuney (2009) envisaged in the formation of metasomatic skarn uranium deposits.

The disseminated uraninite in mineralised leucogranites has been hydrothermally altered and mobilised into coffinite, and deposited as fracture infills and around grain boundaries as veinlets. This postulation is in concurrence with suggestion by Kinnaird and Nex (2007) that a hydrothermal system overprints the uraniferous magmatic event resulting in uranium enrichment. The vein-hosted mineralisation appears as magnetite veins (Fig. 4.17), possibly of magmatic hydrothermal origin, which cut across leucogranites mineral assemblages pre-dates silicification associated with epigenetic botryoidal coffinite.

All in all, the model for the origin of uranium mineralisation in the Inca U deposit begins with sourcing uranium through upper amphibolite facies related partial melting into granites, followed by multiple release of uranium enriched solutions from U enriched leucogranites, and infiltration into host rocks causing skarn formation and successive U enrichment. Finally, late meteoric fluid under hydrothermal conditions appears to be associated with late botryoidal coffinite mineralisation together with opal and aragonite as well as partial oxidation of magnetite to hematite that is also related to this event.

Chapter 6

6. Conclusions and Recommendations

6.1 Conclusion

This study has provided some knowledge and information on the occurrence and possible evolution of the Inca deposit uranium mineralisation. The Inca uranium deposit is suggested to be a product of metamorphic-magmatic-hydrothermal and meteoric mineral system. The upper amphibolite metamorphism that produced partial melting of pre-Damara basement rocks and epicontinental metasedimentary rocks of the Central Zone, Damara belt, is responsible for sourcing of uraniferous leucogranites. The uranium mineralisation is essentially of disseminated euhedral to subeuhedral primary uraninite; and magmatic-hydrothermal, disseminated to semi-massive and botryoidal coffinite. Both uraninite and coffinite are confined to leucogranites and calc-silicate rocks as well as magnetite skarn rocks. Coffinite has been mainly derived from partial dissolution of uraninite under hydrothermal conditions and is associated with sulphide and REE mineralisation as fracture infills and along grain boundaries of host mineral assemblages of leucogranites and calc-silicate rock as well as magnetite skarn rock.

Pervasive fractures facilitated remobilization of uranium ions and served as conduit for fluid transport as well as deposition sites. The iron skarn rock served as a redox boundary and triggered precipitation of uranium mineralisation, and associated REE and sulphide ore minerals.

Late meteoric fluid under hydrothermal conditions appears to be associated with late botryoidal coffinite mineralisation together with opal and aragonite. Partial oxidation of magnetite to hematite is related to this later event.

6.2 Recommendations

Despite enhanced information on the characterisation of formation processes of uranium minerals, further work in form of mineral geochemistry, U-Pb geochronology and stable isotope, is recommended to advance the understanding of the evolution and quantification of the ore formation processes involved. U-Pb Geochronology, sulphur isotope studies, and stable isotope studies are recommended to constrain the timing and relationship of diverse mineralisation observed at Inca deposit. A study of the origin of massive-semi massive magnetite would aid in the understanding of the origin of fluids and advance the search for magnetite related uranium mineralisation in the Central Zone of the Damara orogenic belt.

7. References

Ballouard, C., Poujol, M., Boulvais, P., Mercadier, J., Tartèse, R., Venneman, T., Deloule, E., Jolivet, M., Kéré, I., Cathelineau, M., and Cuney, M., 2017. Magmatic and hydrothermal behaviour of uranium in syntectonic leucogranites: The uranium mineralisation associated with the Hercynian Guérande granite (Armorican Massif, France). Ore Geology Reviews, 80, pp 309-331.

Bruneton, P. and Cuney, M., 2016. Geology of Uranium deposits. In: Hore-Lacy, I., Uranium for nuclear power, Woodhead publishing series in Energy, No. 93, Copyright © 2016 Elsevier Ltd.

Cuney, M., 2014. Felsic magmatism and uranium deposits. Bull. Soc. Geol. Fr. 185, 75–92. http://dx.doi.org/10.2113/gssgfbull.185.2.75

Cuney, M., 2009. The extreme diversity of uranium deposits. *Miner. Deposita.*, 44, pp. 3–9.

Dubessy, J., Ramboz, C., Nguyen, Trung, C., et al., 1987. Physical and chemical control (fO_2, T, pH) of the opposite behaviour of U and Sn-W as exemplified by hydrothermal deposits in France and Great Britain, and solubility data. *Bull Mineral,* 110, pp. 262-644.

Fayek, M., Kyser, T. K. and Riciputi, L. R., 2002. U and Pb isotope analysis of uranium minerals by ion microprobe and the geochronology of the McArthur and the sue zone uranium deposits, Saskatchewan, Canada. *Can. Mineral,* 40, pp. 1553-1569.

Guo, X., Szenknect S., Mesbah A., Labs S., Clavier N., Poinssot C., Ushakov S.V., Curtius H., Bosbach D., Rodney R.C., Burns P., Navrotsky A., 2015. Thermodynamics of Formation of Coffinite, USiO4. *Proc. Natl. Acad. Sci. USA*. 112 (21), pp. 6551–6555.

Geological Survey of Namibia, 2018. Nuclear Fuel Map. Ministry of Mines and Energy, Windhoek, Namibia.

Geological Survey of Namibia, 2019. 1:250 000 Walvis bay Geological map sheet. Ministry of Mines and Energy, Windhoek, Namibia.

Hazen, R. M., Ewing, R. C., and Sverjensky, D. A., 2009. Evolution of uranium and thorium minerals. American Mineralogist, Vol. 94, p. 1293-1311.

Hecht, L. and Cuney, M., 2000. Hydrothermal alteration of monazite in the basement of Athabasca basin: implication for the genesis of unconformity related deposits, Miner Deposita 35, pp. 791-795.

Iyer, K., 2007. Mechanisms of serpentinization and some geochemical effects. *Unpub. PhD thesis, Univ. of Oslo, Norway,* 674, ISSN 1501-7710.

Jacob, R. E, Corner, B. and Brynard, H. J., 1986. The regional geological and structural setting of the uraniferous granitic provinces of southern Africa. In: Anhaeussser, C.R. and Maske, S. (ed.), Mineral deposits of southern Africa: *Geological Society of South Africa,* 2, pp. 2335.

Kinnaird, J. A. and Nex, P. A. M., 2007. A review of geological controls on uranium mineralisation in sheeted leucogranites within the Damara Orogen, Namibia: Transactions of the Society of Mining and Metallurgy, *Applied Earth Science*, sec. B, 166, pp. 68-85.

Kríbek, B., Knésl, I., Pasava, J., et al., 2005. Hydrothermal alteration of the graphitized organic matter at the Kansanshi Cu (Au-, U-) deposit, Zambia. In: Mao J, Bierlein FP (eds), Mineral deposit Research: meeting the global challenge. Proc 8th SGA Meeting Beijing, China, pp. 277-280.

Langmuir, D., 1978. Uranium solution-mineral equilibria at low-temperatures with applications to sedimentary ore-deposits. *Geochim Cosmochim Acta*., 42(6):547–569.

Marlow, A. G. M., 1981. Remobilization and primary genesis in the Damaran orogenic belt. PhD Dissertation, Leeds University, pp. 227.

Massart, R., 1981. Preparation of aqueous magnetic liquids in alkaline and acidic media. *IEEE Trans. Magn*. 17, pp. 1247-1248

Nex, P.A.M., Kinnaird, J.A. and Oliver, G.J.H., 2001a. Petrology, geochemistry and mineralisation of post-collisional magmatism around Goanikontes, southern Central Zone, Damara Orogen, Namibia. *Journal of African Earth Sciences*, 33, pp. 481–502.

Plášil, J., 2014. Oxidation–hydration weathering of uraninite: the current state-of-knowledge Journal of Geosciences, 59, 99–114.

Pontifex and Associates (Pty) Ltd., 2008. Mineralogical report No. 9326. Unpubl. Report, Reptile Uranium Namibia Pty Ltd, Swakopmund, Namibia.

Reyx, J., 2009. Mineralogie Study 9512, Report to Reptile Uranium Namibia (Pty) Ltd, Swakopmund, Namibia.

Richard, A., Rozsypal, C., Mercadier, J., Banks, D. A., Cuney, M., Boiron, M-C. and Cathelineau, M., 2012. Giant uranium deposits formed from exceptionally uranium-rich acidic brines.Nature Geoscience, Vol. 5, DOI: 10.1038/NGEO1338.

Rollinson, H., 1993. Using geochemical data: evaluation, presentation, interpretation. *John Wiley & Sons, Inc., New York.*

Robb, L., 2005. Introduction to ore forming processes. *Blackwell Science, Oxford, UK*, pp. 75.

Sawyer, E.W., 1981. Damara structural and metamorphic geology of an area southeast of Walvis Bay, SWA/Namibia. *Mem. Geol. Surv. S.W. Afri./Namibia*, 7, pp. 94.

Schikorr, G., 1933. The iron (II) hydroxide and a ferromagnetic iron (III) hydroxide. Zeitschrift fur Anorganische und Allgegemeine Chemie. 212 (1): pp 33-39.

Smith, D.A.M., 1965. The geology of the area around the Khan and Swakop rivers in South West Africa. Memoirs of the Geological Survey of South Africa (South West Africa Series), 33, pp. 200-301.

Spivey, M., Penkethman, A., and Culpan, N., 2010. Geology and mineralisation of the Recently Discovered Rössing South Uranium Deposit, Namibia. Society of Economic Geologists, Inc. Special Publication, 15, pp. 720-746.

Turpin, L., Leroy, J. and Sheppard, S.M.F., 1990. Isotopic systematics (O, H, C, Sr, Nd) of superimposed barren and U-bearing hydrothermal systems in Hercynian granite, Massif Central, France. *Chem. Geol.* 88, pp. 85-96.